Universidade do Minho
Escola de Engenharia

Sandra Beatriz Tomé Gonçalves

µLED Optrode for Acute Optogenetic
Applications

Sandra Beatriz Tomé Gonçalves   µLED Optrode for Acute Optogenetic Applications

UMinho | 2019

janeiro de 2019

Universidade do Minho
Escola de Engenharia

Sandra Beatriz Tomé Gonçalves

µLED Optrode for Acute Optogenetic
Applications

Tese de Doutoramento
Programa Doutoral em Líderes para as Indústrias Tecnológicas

Trabalho efetuado sob a orientação do
Professor Doutor José Higino Gomes Correia

janeiro de 2019

DECLARAÇÃO

**Nome:** Sandra Beatriz Tomé Gonçalves

**Endereço eletrónico:** id5750@alunos.uminho.pt; **Telefone:** 915636173

**Número do Cartão de Cidadão:** 13571854

**Título da tese:** $\mu$LED Optrode for Acute Optogenetic Applications

**Orientador:** Professor Doutor José Higino Gomes Correia

**Ano de conclusão:** 2019

**Designação do Ramo de Conhecimento do Doutoramento:** Programa Doutoral em Líderes para as Indústrias Tecnológicas

É AUTORIZADA A REPRODUÇÃO INTEGRAL DESTA TESE/TRABALHO APENAS PARA EFEITOS DE INVESTIGAÇÃO, MEDIANTE DECLARAÇÃO ESCRITA DO INTERESSADO, QUE A TAL SE COMPROMETE.

Universidade do Minho,

Assinatura: _____

STATEMENT OF INTEGRITY

I hereby declare having conducted my thesis with integrity. I confirm that I have not used plagiarism or any form of falsification of results in the process of the thesis elaboration.

I further declare that I have fully acknowledged the code of ethical conduct of the University of Minho.

University of Minho,

**Full Name:** Sandra Beatriz Tomé Gonçalves

Signature: _____

# Acknowledgments

This PhD journey was an extraordinary experience. It was a roller coaster ride in terms of emotions and work, in which I have grown and learned a lot. In the ups and downs I had the support of incredible people that I want to express my gratitude.

First and foremost, I would like to acknowledge my supervisor, Higino Correia, for the all the support and advice during this project. Also, my supervisor at MIT, Ed Boyden, for teaching me to always look at the big picture.

Because this work was a team effort, I really need to thank people from Microtechnologies Lab, namely João Ribeiro, Helena Fernandes, Ângela Loureiro and Sara Pimenta for all their contribution to make this project a reality. I also appreciate all the work discussions and directions with Alexandre Silva. Last but not least I want to thank Marino Maciel for the companionship and help every time I needed. For all of you, you are good friends.

To all that warmly welcome me at MIT and specially in the Boyden lab, a sincere thank you. I was very honored to join this research group. Jörg Scholvin, Francisco Flores and Justin Kinney thank you for teaching me so much about probes, about animal experiments and data acquisition and analysis. For all the work done at Champalimaud Foundation, I want to express my gratitude to Rodrigo Oliveira for all you teach me and for your patience.

Moreover, I cannot forget the amazing people I met at MIT, the Portuguese lunch group. You provide me the most amazing year with all kind of experiences. Being so far away from home was so much easier in your company. I have grown as scientist as well as a person.

This section could not be completed without expressing my thanks to my family that always believe in me and help however they could.

Thank you all!

# Abstract

The human brain remains among the most poorly understood organ despite all studies and efforts dedicated to it. Gathering knowledge on the brain mechanisms as a whole and individual networks has been a challenge in neuroscience. Advances in microtechnologies enabled the development of micrometer-sized devices or microsystems to interface and access a wide range of brain areas. The study of neural networks aims to understand neurophysiological processes and restore lost neural functionalities, in a way that catalyzes new diagnostic tools and treatments for brain disorders and diseases, such as Parkinson, Alzheimer, depression, etc.

Optogenetics is a recent technique that has revolutionized scientists' ability to control neurons by promoting excitation or inhibition from targeted cells sensitive to light. Optogenetic tools (known as optrodes) have shown cell-type neuromodulation with unique spatial resolution by delivering light on a cellular-scale with millisecond temporal precision.

In the interest of developing a new tool for deeper understanding of the human brain and its mechanisms, this PhD thesis presents the development of an optrode microsystem capable of optical stimulation and simultaneous electrical recording. The photostimulation in the proposed device will be provided by a commercial light emitting diode (LED) chip. With this approach, the light source is directed to the target engineered neuron cells, in order to minimize losses of the emitted irradiance, a major issue of conventional fiber-based approaches. The manufacturing process of the LED-based optrode device comprehends only standard and low-cost microfabrication technologies, such as blade dicing, photolithography and physical vapor deposition.

Fabrication results demonstrated mechanically robust optrodes consisting of 8 mm long and 600 $\mu$m wide single-shafts with a sharp tip. The optrode dimensions were optimized in order to minimize tissue damage and shaft length was maximized to reach deep brain structures. Validation tests show that probes have good recording and optical features, with average impedance magnitude of 371 k$\Omega$, at 1 kHz, and optical power of 1.2 mW.mm$^{-2}$ (at 467 nm), respectively. The LED chip integrated in the optrode showed a peak wavelength at 467 nm and thus enables optogenetic experiments to be performed in engineered cells sensitive to blue light, e.g. neurons expressing channelrhodopsin-2 opsins.

Overall, results show a device capable of meeting the requirements of a neural interface for recording and stimulating of brain activity, which suggests a promising tool for neuroscience.

# Resumo

O cérebro humano permanece um dos órgãos menos compreendidos, apesar de todos os estudos e esforços dedicados a tal. Angariar conhecimento acerca dos mecanismos cerebrais como um todo assim como circuitos neuronais individuais tem sido um desafio na área das neurociências. Os avanços nas microtecnologias permitiram o desenvolvimento de dispositivos na escala dos micrómetros ou microssistemas que fazem interface e acedem a uma vasta gama de áreas cerebrais. O estudo dos circuitos neuronais tem como objetivo compreender os processos neurofisiológicos e restaurar funcionalidades cerebrais perdidas, de forma que esses estudos possam catalisar novas ferramentas de diagnóstico e tratamentos para doenças e distúrbios de foro mental, tal como o Parkinson, Alzheimer, depressão, entre outros.

Optogenética é uma técnica recente que revolucionou a capacidade dos cientistas de modular o funcionamento de neurónios promovendo a excitação ou inibição de células-alvo sensíveis à luz. Ferramentas que promovem optogenética (conhecidas por optrodes) têm demonstrado neuromodulação de grupos de células com resolução espacial única através da iluminação à escala celular e com uma precisão temporal de milissegundos.

Na perspetiva de desenvolver uma ferramenta inovadora para um maior conhecimento de cérebro humano e os seus mecanismos, esta tese de doutoramento propõe o desenvolvimento de um microssistema optrode capaz simultaneamente de estimulação ótica e gravação elétrica de circuitos neuronais. No dispositivo proposto, a fotoestimulação será conseguida através de díodos emissores de luz (LEDs). Com esta abordagem, a fonte de luz é direcionada para as células neuronais modificadas de forma a minimizar as perdas de radiância ótica emitida, sendo esta uma das principais preocupações nas abordagens convencionais com fibra ótica. O processo de manufatura do optrode baseado em LEDs compreende apenas tecnologias de microfabricação padrão e de baixo custo, como a corte com lâmina, fotolitografia e deposição física de vapor.

Os resultados do fabrico demonstraram optrodes mecanicamente robustos que consistem em sondas únicas, cada uma com 8 mm de comprimento, 600 $\mu$m de largura e ponta afiada. As dimensões do optrode foram otimizadas de forma a minimizar o dano no tecido e o seu comprimento foi maximizado para aceder a estruturas neuronais profundas. Os testes de validação demonstraram que os dispositivos têm boas caraterísticas funcionais de gravação e óticas, com uma magnitude da impedância de 371 k$\Omega$, a 1 kHz, e ainda potência ótica de 1.2 mW.mm$^{-2}$ (a 467 nm), respetivamente.

Os LEDs integrados nos optrodes apresentam um pico de emissão aos 467 nm e, portanto, possibilita realizar estudos optogenéticos com células sensíveis à luz azul, por exemplo, neurónios que expressem opsinas channelrhodopsin-2.

Em suma, os resultados demonstram um dispositivo que vai de encontro aos requisitos de uma interface neuronal com capacidade de gravação e estimulação da atividade neuronal. Isto sugere que o dispositivo poderá vir a ser uma ferramenta promissora na área de estudo das neurociências.

# Contents

# List of Figures

# List of Tables

# List of Acronyms

| Acronym | Definition |
| --- | --- |
| CNS | Central nervous system |
| PNS | Peripheral nervous system |
| DBS | Deep brain stimulation |
| OCD | Obsessive compulsive disorder |
| MEA | Microelectrodes array |
| UEA | Utah electrode array |
| ChR-2 | Channelrhodopsin-2 |
| BR | Bacteriorhodopsin |
| HR | Halorhodopsin |
| NpHR | Natronomonas pharaonis halorhodopsin |
| ILD | Injection laser diode |
| AAMI | American association of medical instrumentation |
| EEG | Electroencephalography |
| ECG | Electrocardiography |
| fMRI | Functional magnetic resonance imaging |
| LED | Light emitting diode |
| FIB | Focused ion beam |
| SEM | Scanning electron microscope |
| CVD | Chemical vapor deposition |
| UOA | Utah optrode array |
| USOA | Utah slant optrode array |
| MQW | Multiple quantum well |
| RF | Radio-frequency |
| DRIE | Deep reactive ion etching |
| CMOS | Complementary metal-oxide semiconductor |
| PCB | Printed circuit board |
| MEMS | Micro-electro-mechanical systems |
| DLW | Direct laser writing |

| | |
|---|---|
| PR | Photoresist |
| UV | Ultra-violet |
| PVD | Physical vapor deposition |
| DC | Direct current |
| AC | Alternating current |
| e-beam | Electron-beam |
| SNR | Signal-to-noise ratio |
| EIS | Electrochemical impedance spectroscopy |
| MTTF | Mean time to failure |
| PBS | Phosphate buffer solution |
| DI | Deionized |
| ECP | Electrically conducting polymer |
| LFP | Local field potential |
| S1HL | Primary somatosensory cortex, hindlimb region |
| M2 | Secondary motor cortex |
| ACC | Anterior cingulate cortex |
| 3D | Three-dimensional |

# List of Chemical Symbols

| Symbol | Definition |
| --- | --- |
| Si | Silicon |
| SiON | Silicon Oxynitride |
| SiN | Silicon Nitride |
| $SiO_2$ | Silicon Dioxide |
| GaN | Gallium Nitride |
| TiN | Titanium Nitride |
| $IrO_2$ | Iridium Oxide |
| Au | Gold |
| PEDOT | Poly(ethylene dioxythiophene) |
| PDMS | Polydimethylsiloxane |
| $Al_2O_3$ | Alumina |
| Ti | Titanium |
| Al | Aluminum |
| Pt | Platinum |
| Ar | Argon |
| $N_2$ | Nitrogen |
| $H_2O_2$ | Hydrogen peroxide |
| $NH_4OH$ | Ammonium hydroxide |
| EDOT | 3,4-Ethylenedioxythiophene |
| PSS | Poly(sodium 4-styrenesulfonate) |

# Chapter 1

# Introduction

The brain is one the most complex living structure known, capable of shaping our thoughts, hopes, dreams, imagination and abstract thinking. How the brain processes computation, retain memory or feel emotions, is still not well understood, but a lot of progress was done towards the understanding of brain functions. Ultimately, this knowledge will make us understand better how the different brain illnesses emerge and how they affect us. With a wide spectrum of brain diseases and disorders that represents emotional, financial and social burdens to the patients, their families and their network, it becomes crucial the development of new or improved technologies. Indeed, during the last decade, many efforts have been made to supply new tools that study more deeply the information processing and networks in the brain.

This chapter briefly introduces the basic concepts of the nervous system, brain functions and the role of neuron cells in transmitting and processing the information. Moreover, the engineering challenges and requirements for the development of implantable technological solutions are explained. This kind of microsystem is the one being proposed in this thesis, which aims to interface with engineered neural tissue for optogenetics. Finally, the motivation to develop a novel implantable microdevice useful for optogenetic studies is presented and the objectives for this thesis are summarized.

## 1.1  Nervous system and information transmission

Humans, as nearly all multicellular organisms, rely on the nervous system to control and coordinate body functions as well as respond to internal and external stimuli (e.g. breathing, body temperature, organ function, muscle activity, sensory inputs, etc.). The nervous system is divided into the central nervous system (CNS) and peripheral nervous system (PNS): the first comprises the brain and the spinal cord, and the latter consists of nerves responsible for connecting the central system to rest of the body [1]. This complex communication system uses specialized cells to carry messages from one cell to another ensuring that information transmission among all body parts occurs quickly and efficiently.

The brain is the central organ of the CNS. It is divided into two hemispheres broadly similar in shape, but some functions are associated with one of the sides: e.g. language is associated with in the left hemisphere and visual-spatial ability in the right. Each hemisphere is conventionally categorized into four lobes – the frontal, temporal, parietal, and occipital lobes, each associated with specific functions [2]. The cerebral cortex is the outer layer of the brain that covers all these neural structures and processes memory, attention, conscience, language and sensory perception. Due to its complex multi-laminated structure composing of so many functions, the cerebral cortex is one of the most study brain structures to better understand basal and pathological brain circuitry [3]. Most areas of the brain are basically the same in all mammals, which means animal models such as mice and rats can be study to unfold details of connection and function of neural activity. This is not the case for the cerebral cortex where distinctive circuits and organization complexity vary from species. The huge development of the cerebral cortex in humans distinguish them from other mammals due to its complex multi-laminated organization, being directly related to the emergence of the superior intellectual capacities [3].

At a cellular level, the information carried by the nervous system is accomplished by neurons. These cells transmit electrical signals called impulses or action potentials. Glial cells are another type of cells existing in the nervous system. However, they act mostly as a support element that bring structure and consistency to the brain, not being able to generate electricity and thus to transmit information [1].

Neurons can be classified into three types according to the direction in which an impulse
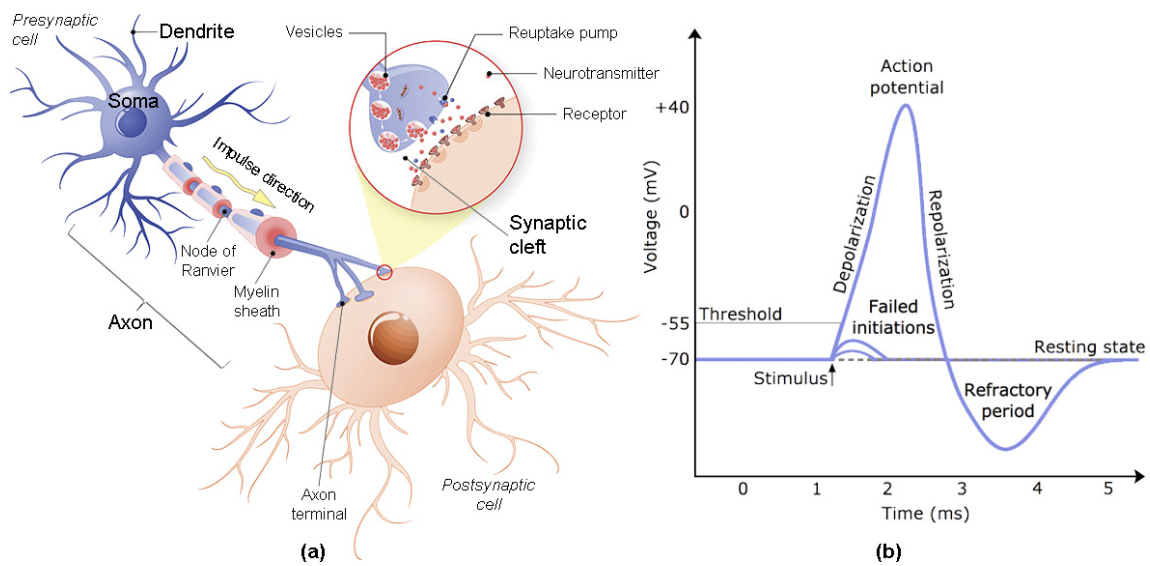
**Figure 1.1:** (a) Illustration of an impulse being propagated down an axon through its terminals to the dendrite of the next cell. The main parts of a typical neuron are highlighted. Adapted from [4]. (b) Graph of an action potential [5]. Plotting voltage (in mV) measured across the cell membrane against time (in ms). When the input signals are strong enough to pass the threshold, occurs depolarization in the cell, followed by its repolarization, which goes past the resting potential into hyperpolarization, and finally the membrane returns to rest.

travel: (1) Sensory neurons carry impulses from the sense organs to the spinal cord and brain; (2) Motor neurons carry impulses from the brain and the spinal cord to muscles and glands, and (3) Interneurons connect sensory and motor neurons and carry impulses between them [2]. Despite varying in shape and size, neurons have several features in common. Figure 1.1(a) illustrates the main parts that constitute a neuron, and how it works to transmit electrical impulses to another neuron using neurotransmitter vesicles in the synapse area. The largest part of a typical neuron is the cell body (soma). Dendrites are short, branched extensions that spread out from the soma. They carry impulses from the environment or from other neurons toward the soma until the other end of the cell. The long fiber that carries impulses away from the soma is called the axon. In some neurons, the axon is surrounded by an electrical insulating membrane, the myelin sheath, that aims to increases the speed at which an impulse can travel along the axon. The axon ends in a series of small swellings called axon terminals, located some distance from the soma [1]. In most animals, axons and dendrites are clustered into bundles of fibers called nerves [2].

The transmission of messages is based on an electrochemical pulse: along the presynaptic neuron information is transmitted in the form of electrical pulses from dendrites to axon terminals.

At these terminals, vesicles filled with neurotransmitters (chemical messengers) release them into the synaptic cleft. Synapses are the contact points where one neuron communicates with another. Then, receptors in the dendrites of the postsynaptic cell receive neurotransmitters, collect all the input signals from other neurons and send them to the soma. The soma generates an output signal following a non-linear law and sends the electrical impulses to the axons. In this way, input signals are processed and transmitted. The signal output may result on an action potential (also called spike) depending if the strength of the input signals is able to produce a small difference voltage in the cell membrane, and thus pass the threshold required to depolarize and repolarize its membrane. After, the membrane goes into a refractory period where input signals have nearly no effect on the membrane potential. Finally, after a few milliseconds, the neuron achieves again the initial resting state and is ready to spike again. Indeed, a neuron may be able to fire spikes hundreds of times every second [6]. The changes in the potential of a cell membrane is shown in Figure 1.1(b).

## 1.2    Neural interfacing methods

Devices capable of interfacing with neural circuits, either by recording or modulating their activity, are a reality for a few decades now. Neuroscientists take advantage of these interfaces to map brain networks and gather knowledge of their working mechanisms and interrelations. The ultimate goal of these devices, also known as neural probes, is to restore sensory and motor functions, and to treat neurological disorders.

### 1.2.1    Electrical interfaces

Conventionally, neural probes consist of electrical conductors that are in contact with the aqueous ionic solutions of brain tissue. Early probes consisted of insulated wires capable of acquiring bioelectric signals, by transducing ionic currents into electric currents [7]. The modality of recording neural activity was quickly followed by electrical stimulation capable neuromodulation of brain networks [8].

Techniques that include probing and perturbing neural activity are used as therapeutics into clinical practice for nervous system diseases. Deep brain stimulation (DBS) has shown beneficial
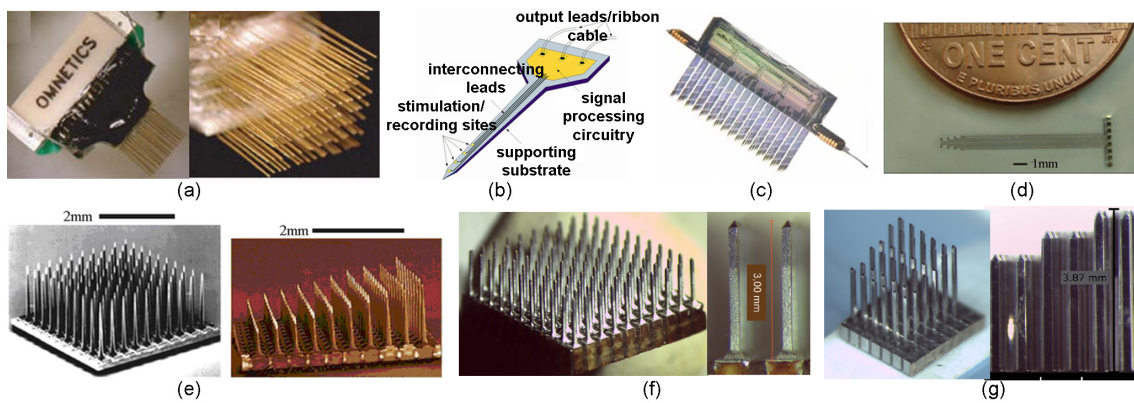
**Figure 1.2:** Implantable electrical neuroprobes. (a) Microwire array. (b) Typical single micromachined Michigan probe. (c) Michigan 64-channel array. (d) Flexible parylene-based 8-channel probe. (e) UEA flat (left) and slanted (right) profile. Adapted from [24] (f) Out-of-plane high density Al MEA. (g) 6 × 6 matrix of Si electrodes with 4 mm, 3.5 mm and 3 mm length, and 600 $\mu$m pitch.

effects in a variety of neurological conditions, such as depression [9, 10], obsessive compulsive disorder (OCD) [11, 12], chronic pain [13, 14], Parkinson's disease [15], epilepsy [16], essential tremor, dystonia and Tourette syndrome [17]. Cochlear [18, 19] and retinal [20] implants are also widely used in the therapy of deafness and blindness, respectively. Indeed, cochlear neuroprostheses are a successful therapeutic method with more than 300,000 devices already implanted worldwide [21]. Neuroprosthetics are also applied to peripheral neural system disabilities, by trying to achieve control of artificial limbs in individuals with tetraplegia [22, 23].

Neural probes can be classified according to their fabrication methods and design. Generally implantable probes relying on an electrical interaction with neural tissue can be classified in three types [24, 25]: Microwires, Micromachined, and Flexible Arrays (Figure 1.2). These designs rely on different technologies, designs and transduction materials to manufacture probes, and each type presents advantages and drawbacks for each application.

One of the first neural interface for chronic recording was made from insulated microwires (Figure 1.2a), which remains in use today due to its ability to provide durable and single-neuron recordings for more than a year [26]. This type of probe is easily clustered in bundles for multi-site recording (tetrodes), and it is particularly advantageous to access deep brain structures.

Advances in microtechnology, such as photolithographic and etching techniques, enabled the development of silicon (Si) micromachined electrodes. The Michigan probe [27] and the Utah

Electrode Array (UEA) [28] are two well-known Si-based configurations of such approach. The Michigan configuration includes single-shaft (Figure 1.2b), multi-shaft and 3D layouts (Figure 1.2c) with multiple recording sites per shaft. On the other hand, the UEA configuration (Figure 1.2e) comprises a 3D array of 100 needle-shaped microelectrodes, and each tip of the shafts interacts with the neural tissue by either recording or stimulating it. Currently, UEA electrodes have a maximum length of 1.5 mm, which restricts their application to surface structures of the cerebral cortex. Efforts are been made to obtain 3D microelectrodes array (MEA) with longer shafts based on Si wafers using micromachining technology. Compact 3D arrays mostly include microassembly methods, which combine 2D probes into integrative platforms [29–31]. Having the UEA as a starting point, our group has previously presented approaches to fabricate 3D MEA with high aspect-ratio shafts (up to 4 mm long), employing aluminum [32, 33] and Si wafers [34] as the bulk material for the probe manufacturing process (Figure 1.2f and 1.2g). Other approaches reported to fabricate 3D arrays, including microwire electrical discharge machining [35] and self-assembled processes [36, 37].

Finally, flexible arrays (Figure 1.2d) arose to overcome the mechanical mismatch between stiff probes and soft neural tissue. Flexible materials such as polyimide and parylene-C are used to substitute Si on microfabricated probes and stainless steel, or tungsten on microwires [38, 39].

In terms of industry, some major companies, specialized in the commercialization of electronic components, have now available commercial neuroprobes. Most of these companies are North-American, such as Medtronic, Tucker-Davis Technologies, Intan Technologies, Microprobes, and Plexon Inc. Other industrial approach to emergent specialized companies in neuroprobes mostly result from universities spin-offs: NeuroNexus Technologies is a 13-years old spin-off from the University of Michigan (USA); Blackrock Microsystems and Blackrock Neuromed are spin-offs from University of Utah (USA); and, Atlas Neuroengineering is a 5-years old spin-off from the University of Freiburg (Germany). Riple and Epitel are also examples of specialized companies commercializing neuroprobes.

Despite having represented a major breakthrough in the field of neuroscience, electrical interfaces still hold clinical restrictions such as the inability to target specific cell types within neural networks, and may cause potentially serious sensory motor, and neuropsychological side effects [15]. Taking as an example, patients with Parkinson's disease undergoing electrical stimulation – where no specific cell-type is targeted, instead the implanted electrodes target cells within their reach

– may suffer some side effects, such as depression, mood alteration, or sensory and motor control problems. Suppressing side effects requires turning off the electrical stimulation pulses [40]. Besides missing neuron selectivity, electrical stimulation shows inefficient inhibition, as stimulation is typically excitatory.

## 1.2.2 Optical interfaces

The engineering tools interacting optically with the brain using optogenetics are called optrodes. Typically, they are simultaneously capable of delivering light to neurons and electrically recording them. Currently, there are various optrode designs reported to the scientific community, which will be presented in the Chapter 2. These approaches are essentially categorized depending on source of light: customized optical fibers, waveguide systems or $\mu$LEDs. In an industrial context, the range of designs is narrower. Neuronexus and Cambridge Neurotech commercialize optogenetics-compatible neural probes that integrate exclusively optical fibers as light source.

Optical neuromodulation showed its potential by selectively controlling dysfunctional circuits and, consequently, has been proposed to assist several diseases: dysfunctional parkinsonian motor control [41, 42]; blindness [43–48]; deafness [21, 49, 50]; spinal cord injuries [51]; and, neuropsychiatric disorders such as compulsive behavior [52], social dysfunction [53], anxiety [54] and depression [55, 56]. Recently, Roy et al. showed that optogenetic activation of hippocampal cells in transgenic mouse models might lead to an effective strategy for treating memory loss in the early stages of Alzheimer disease [57]. Nevertheless, it is in the field of vision impairments that optogenetic studies are closer to clinical trials: Retrosense Therapeutics is a North-American company that is in Phase I/II of a clinical trial, which aims to study dose-escalation of safety and tolerability of a optogenetic promoter (RST-001) in patients with Retinitis Pigmentosa; GenSight (France) had also scheduled to start in 2016 a clinical trial for visual impairments.

So far, optical stimulation is not mature enough to be applied in clinical practice. There are still some key issues requiring additional research and development in photostimulation: (i) gene delivery methods must prove to be safely and stably transferred into the patient's neurons; and (ii) it is still necessary to optimize the optical devices with an effective optical control, which means delivering sufficient light intensity to the proper local neural circuit [58]; (iii) reliable and scalable

technologies that promote device miniaturization; and (iv) development of active interfaces with a life-lasting, fully integrated and ultra-low-power wireless system, capable of supporting bidirectional data flow [59].

## 1.3   Optogenetics

The human brain functions in symbiosis with complex cell networks composed of estimated 85 billion neurons, 100 trillion synapses, and 100 types of chemical neurotransmitters [60]. A long-standing aspiration in the scientific community is to understand and map the large-scale connectivity of the brain. Optogenetics emerged as a novel technique to help serve this purpose.

The term optogenetic reflects the combination of two scientific areas: photonics and genetic techniques. In this field of research, neural cells are genetically modified in order to make them susceptible to light stimulation, providing excitatory or inhibitory control of the neural circuitry with a millisecond precision [61]. The millisecond-scale precision is essential for neuroscience to keep pace with the dynamics of action potentials and synaptic currents [62].

The engineered reagents are single-component light-sensing systems, conservatively referred as opsins, which have a photoreceptive characteristic coupled with a biological function [61]. Figure 1.3 shows the optogenetic technique mechanism, which initializes with transcription and expression processes. Viral systems currently represent the most popular approach of in vivo expression processes [62]. These viral vectors are responsible for the introduction of opsins into the subject's brain. Consequently, the targeted neuron cells express the introduced opsin and, when exposed to light, the photoreceptive proteins will promote a biological effect on those specific cells. In the case of the light-sensitive ion channel opsin, channelrhodopsin-2 (ChR2), exposing the neurons to blue light promotes cell depolarization in those that express the opsin. This means that spatial resolution is improved by not triggering a response from all neurons exposed to light with simultaneous high temporal precision (Figure 1.4). The selective trigger can go beyond the ability to turn on neurons in vivo in a fast-reversible manner. It also enables turning neurons off (cells inhibition), which increases the clinical applications for optogenetic tools.

Nowadays, opsins present four major categories: fast excitation, fast inhibition, bistable modulation, and control of intracellular biochemical signaling in neurons and other cell types. A major
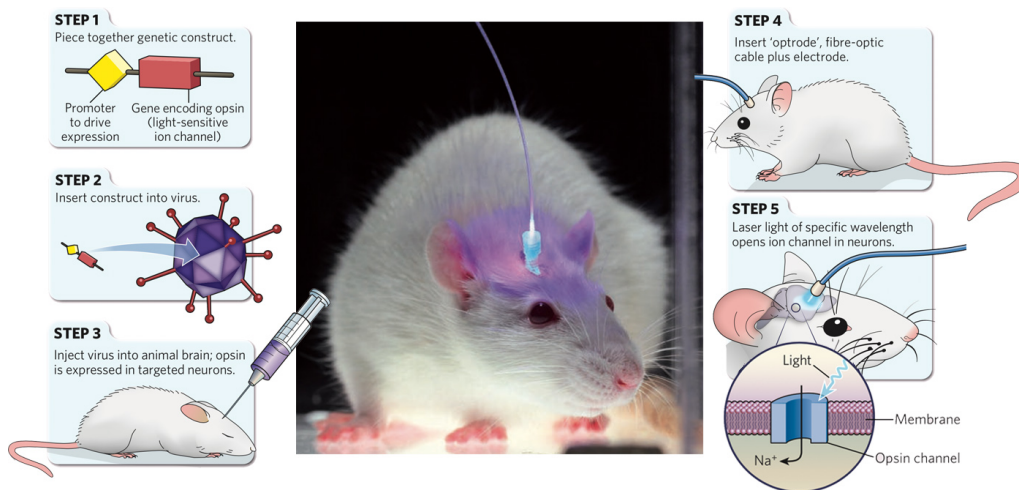
**Figure 1.3:** Optogenetics: genetically modifying targeted cell types for optical depolarization or hyperpolarization of the cell membrane. Adapted from [63].

class of light-sensitive proteins consists of transmembrane rhodopsins, which can be found in several micro-organisms like algae, bacteria and fungi, as well as serving a diverse range of functions [64]. A few examples of the microbial opsin gene family are the light-gated proton pumps bacteriorhodopsin (BR); Halorhodopsin (HR), a light-activated chloride pump; and the light-activated ion-flux proteins, the channelrhodopsin (ChR). In neurons, net photocurrent due to ChR activation is dominated by cation flow down the electrochemical gradient, resulting in depolarization of the neuron. This effect makes ChR the most used optogenetic tool in the context of action potential acquisition and modulation [65]. Both ChR2 and NpHR (Natronomonas pharaonis Halorhodopsin) are being widely employed in optogenetic studies since they could be functionally expressed without the addition of exogenous cofactors [58].

All combined, opsins enable experimental manipulations tuned toward the desired physiologic effect and kinetic properties of the light-dependent modulation. Over the last decade, the development of light-sensitive proteins bioengineered to control neural activity increased considerably and is continuously being improved [66]. Originally, these proteins mainly relied on activation by blue light, like ChR2 with an action-spectrum peak around 460 nm [65]. Nowadays, the range of light-sensitive proteins is wider with an absorption spectrum that covers much of the visible spectrum (400 nm to 630 nm) [67]. Neural modulation efficiency will vary with the specific protein employed, since they show different photocurrent characteristics. The level of protein expression, targeted cell type,
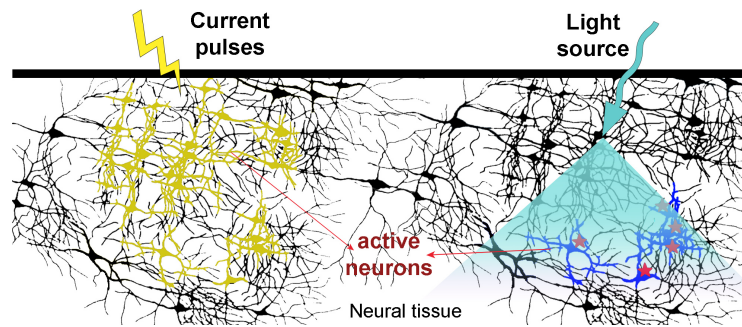
**Figure 1.4:** Comparison between conventional extracellular electrical and optical stimulation of neural circuits. Photostimulation approaches enable targeting selective cell-type (highlighted with a red star) while electrical probes trigger biological responses in the entire vicinity of stimulation focus.

required wavelength, optical power, and spatial extent of the light signal are also relevant variables in photostimulation effectiveness [62, 67].

In 2005, the first published study described how a microbial opsin, a natural light-sensitive ion-transporting membrane protein, could be expressed in neurons to make their electrical activity influenced by light [68]. Over the last decade, optogenetics has seen a rapid rise in the number of publications, therefore becoming a widespread research subject in neuroscience [69].

## 1.4 Requirements to develop an optrode

High-performance optical interfaces face various engineering and manufacturing challenges in order to provide relevant clinical knowledge for neuroscience research. Table 1.1 summarizes the major types of requirements these devices must comply with. Most optogenetic interfaces are combined with traditional electrical recording so that optical stimulation can be simultaneously performed with electrophysiology studies. The development of electro-optical microsystems is even more complex, since the electrical performance of the optical probe has to be ensured. Indeed, most electrical devices have shown to perform well in acute studies, but they tend to fail chronically since electrode performance and properties vary over time. It is often not clear whether these variations are due to changes in the tissue encapsulating the electrode, degradation of electrode materials, or whether there is a change in the excitability or functional response of the neural tissue [70].

Considering the biological tissue response to implanted neural interfaces, there are performan-

ce requirements to be envisaged by both electrical and optical probes. They need to minimize tissue damage and displacement, ensuring reliable acute and chronic recordings as well as efficient single neurons or cell circuit stimulation. The greatest challenge in obtaining consistent or stable stimulation and recordings over time seems to be the biological response that the brain cells show against implanted interfaces [71]. This phenomenon is a major concern, making the biocompatibility of the implantable device one of the key features in the probe design. Yet, so far, no optogenetic tool protects the intact architecture of the brain. Ideally, cells would respond to light delivered at a distance, avoiding implantable solutions. In this perspective, Chuong et al. [72] proposed a novel bioengineered opsin, Jaws, activated by red light (632 nm), which allows transcranial optical inhibition of neurons and reaches deep tissue up to 3 mm, mitigating less invasive solutions in optogenetics [72]. Nevertheless, by illuminating the entire volume of the brain, lateral accuracy of stimulation is impaired.

Engineering design challenges include geometrical, mechanical, electrochemical, thermal, and optical requirements for the development of functional neural probes. An optimal deep probe design for acute and chronic recording and stimulation studies requires small cross-section dimensions that generates the least amount of tissue damage during insertion [24]. Current compact human DBS devices are less than 1.5 mm wide [73]. Penetrating probes must also be structurally robust in order to not buckle or break during implantation into tissue. This should be a major issue in optrodes mounted on Si probes, due to the brittle nature of Si material. Nevertheless, recent high-aspect ratio optrodes based on Si wafers have been reported with mechanical stability during implantation [74, 75]. Other solutions include flexible deep and surface probes [76–79]. Although flexible structures decrease softness mismatch between the implant and the brain, they need hard insertion shuttles to guide them toward the target area [77, 78]. Electrical recording sites must provide low impedance magnitude ($< 1$ M$\Omega$) at 1 kHz (spike recording regime) and stable impedance profile over implantation time [80].

The ability to deliver light into neural tissue with reliability and accuracy rises new demands regarding probe fabrication. The major challenge for the current optogenetic-based interfaces continues to be the effective light intensity delivered to engineered cells [81]. The emitted irradiance threshold to stimulate in vitro culture cells expressing ChR2 is reported to be more than 1 mW.mm$^{-2}$ [62, 68]. Coupling and propagation losses are crucial issues for light intensity efficiency in optrodes.

**Table 1.1:** Summary of development requirements for an optrode microsystem.

| Type of Requirement | Description |
|---|---|
| Functional | • Provide stable and reliable clinical data in acute and chronic studies <br> • Electrical recording and optical stimulation of brain cells activity <br> • Minimize brain tissue damage and reaction against the implant <br> • Reliable transmission and acquisition of clinical data |
| Operational | Recording and stimulation mechanisms shall be activated for a selected task or protocol: <br> • Recording sites shall transduce ionic currents into electrical currents <br> • Optical channels shall produce proper optical power to irradiate target cells and trigger a biological effect |
| Performance | • Minimize dimensions (width and thickness): $<$ mm <br> • Maximize length: $>$ mm (longer probes enable probing deeper neural structures) <br> • Minimize system weight: 4-6 g <br> • Be structurally robust, which do not buckle or break during insertion into tissue <br> • Include inert/biocompatible materials (minimize immune response to implanted devices) <br> • Low impedance material: $<$ M$\Omega$ at 1 kHz [80] <br> • Efficient light power delivery interface (optical stimulation): $> 1$ mW.mm$^{-2}$ [68] <br> • Match wavelength with targeted opsin (e.g. ChR2-expressing neurons depolarize when exposed to 470 nm) <br> • Minimize light intensity losses (coupling, propagation and scattering) <br> • Minimize power consumption (wireless devices) <br> • Minimize overheating processes: Temperature varies $< 2$ °C [84] |
| External interfaces | • Brain tissue interaction: Ionic and phonic currents <br> • Hardware: microdrives, data transmission (cables, telemetry, data loggers) and acquisition, computer |

Coupling light losses are major concerns for optical fiber and waveguide-based devices, which require external sources of light to be coupled to one end of the light channel. Due to their large dimensions, manual coupling of laser diodes to smaller scale structures, amplifies misalignment errors and consequently lowers light efficiency at stimulation site. A recent study employed a compact injection laser diode (ILD) combined with alignment marks for ILD placement that showed improvements in the total light efficiency of the device [82]. Refraction and scattering are also phenomena affecting the efficiency of light delivered to tissue. In implantable devices, this issue is reduced due to the proximity to target cells, while non-invasive solutions still have to struggle with it due to the tissues that act as a block to light. Both refraction and scattering will be pronounced by the encountering of several aqueous intracellular or extracellular layers, and by absorption of light by hemoglobin and water, respectively. The attenuation of light intensity across the brain media further

increases the stimulation focus toward a small group of neurons. A potential option for non-invasive solutions might include higher wavelengths that are relatively amenable to deep tissue penetration.

Light intensity directly affects the volume of activated tissue, and therefore the efficacy of neuromodulation. Accordingly, optrode systems are being optimized to deliver higher optical power, so that the volume of neurons populations available for optical stimulation is maximized, and a more efficient optogenetic interface is accomplished. Activation of a large area of the brain would be optimized by employing multi-site optrodes rather than using a single optical site source to cover the same volume. The multi-site approach provides more homogeneous distribution of light and prevents gradients of light to happen, which causes a different extent of activation in the target volume [67]. This phenomenon is a major concern in neural inhibition studies where uniform light distribution is required to successfully silence neurons. Besides, multi-site optrodes aim to increase power density around target areas in the brain, and subsequently maximize spatial resolution of optical stimulation. This design approach can be accomplished by precisely arranging the embedded light sources in order to minimize inter-optical site spacing, avoiding spatial aliasing and still covering the entire area of interest [83].

Assessing thermal properties of optical sites under various conditions is also crucial, since inadequate light power density or exposure time can cause cell damage from overheating. Rises in temperature of approximately 2 $^\circ$C have been used as threshold to prevent brain damage [84], corresponding nowadays to the regulatory limit recommended by the American Association of Medical Instrumentation (AAMI). By directly exposing light sources to tissue, $\mu$LED-based optrodes could be easily affected by overheating, as light emitter converts energy into heat. However, Kim et al. claims that if small dimensions $\mu$LEDs ($50 \times 50~\mu$m$^2$) are employed, a highly effective thermal management is achieved, and the brain tissue itself operates as an efficient heat sink [77]. In fact, previous studies using LED-optrodes measured local rises of temperature in vivo below 1 $^\circ$C [85, 86].

Another issue shared by electrical and optical interfaces consists in stimulation artifacts (short-duration and high-amplitude spikes), which can be observed in external recording methods, e.g., electroencephalography (EEG) [87] and electrocardiography (ECG) [88]. Artifacts can therefore contaminate biosignals and preclude useful data from being acquired. Functional Magnetic Resonance Imaging (fMRI) that is also a powerful imaging technology used to study brain responses to different stimuli, can be affected by neural interfaces, limiting its compatibility with probes and

may also represent an unsafe procedure to patients [89]. Standard device implants, which include various electronic and metallic parts, such as data acquisition signals, wires, screws, connectors, etc., can cause severe degradation of magnetic resonance images due to differences in magnetic susceptibility, which in turn leads to static field inhomogeneity and susceptibility to artifacts [90]. Attraction, deflection and displacement of implants, malfunction of electronically activated devices, and heating or burn of devices and tissue are also possible risks associated with MRI and neural implants. Nevertheless, strategies to promote compatibility with other technologies, such electromyographic setups [91], imaging techniques [90, 92, 93] and photochemical methods [94] are being developed.

Optical interface design requirements should also include an efficient electronic communication system, so that reliable signal transfer and data acquisition is accomplished, and animal mobility is improved. Communication systems, relying on flexible lightweight cables and rotary joints, are being replaced by untethered platforms, since they enable freely moving animals in chronic experiments and support studies with a larger number of animals.

## 1.5 Motivation and objectives

Implantable neural probes have proved the huge social impact in the overall life quality of the patients, with successfully implanted cochlear prosthetics, Parkinson's symptoms relief with DBS technique, and more recently, promising results in human trials regarding artificial limb control by tetraplegia patients [23]. Hence, these devices are becoming mature therapeutic solution in clinical practice. The potential breakthroughs of neural devices have led to a major research funding of neuroscience project around the world, e.g. the Brain Research Advancing Innovative Neurotechnologies (BRAIN) Initiative, in USA, and the Human Brain project, in Europe.

In the interest of developing a new tool for deeper understanding of the human brain and finding new treatments for brain disorders and diseases, this project research objective is to develop a novel optrode microsystem, integrating commercially available LED chips into a deep-penetrating Si probe. By employing optogenetics, this device is expected to demonstrate improved spatial resolution (cell-type selectivity) and millisecond temporal precision. This device is also expected to electrically record and simultaneous stimulate neural tissue using light pulses coming from a

LED light source. As it will be explored in Chapter 2, LED optrodes have some key advantages over traditional approaches: (i) they can be monolithically manufacture on the substrate or can be transfer into probe body; (ii) do not require external light source; (iii) minimize losses of the emitted irradiance; (iv) individual addressable $\mu$LEDs enable different wavelengths, optical power, and modulation bandwidth to trigger different photosensitive cells; and finally, (v) enable wireless solutions.

The development of the proposed microsystem relies on two major categories:

- Establish a robust manufacturing technology, based on standard and low-cost semiconductor technologies, for fabricating an implantable optrode with optical and electrical capability stable in vivo. Blade dicing, photolithography and thin-film depositions are some of the microtechnologies included for manufacturing of such challenging device.

- Perform in vitro and in vivo methodologies to validate the proposed device as a useful tool in optogenetic studies. Mechanical, electrochemical, optical characterization techniques, as well as electrophysiology studies, are the quantitative tests carried out to accomplish the process validation.

## 1.6 Thesis Outline

The thesis outline proceeds as follows. Chapter 2 describes the state-of-the-art implantable optrode solutions for mapping extracellular activity in the brain of animal models. Also, the optrode design proposed for this work is presented. In chapter 3 the manufacturing and characterization technologies used for the project are described. Experimental results of the optrode prototypes are presented in Chapter 4, which includes fabrication output and in vitro mechanical, electrochemical and optical characterization of the device. Chapter 5 explores in vivo testing on mice brains using two different probe solutions, comprising electrophysiology and optogenetic studies. The last chapter, Chapter 6, provides conclusions of this research and future directions for this work. In the Annex A is listed the international journal publications that have resulted from this thesis.

# References

[1] E. R. Kandel, J. H. Schwartz, and T. M. Jessell, Principles of Neural Science. New York, USA: McGraw-Hill, 2000.

[2] W. J. Hendelman, Atlas of functional neuroanatomy, Second ed. Boca Raton, FL, USA: CRC Press, 2006.

[3] J. DeFelipe, "The evolution of the brain, the human nature of the cortical circuits, and intellectual creativity," Frontiers in Neuroanatomy, **5**(20), doi: 10.3389/fnana.2011.00029, 29, 2010.

[4] iStock. Chemical synapses figure. link to web Accessed on July 2018]

[5] Wikipedia online. Action potential figure. `https://commons.wikimedia.org/wiki/File:Action_potential.svg` [Accessed on July 2018]

[6] W. Gerstner, and W. M. Kistler, Spiking Neuron Models. Cambridge University Press, 2002.

[7] M. Neuman, Biopotential Electrodes. 2nd Edition The Biomedical Engineering Handbook CRC Press, 1999.

[8] N. G. Hatsopoulos, and J. P. Donoghue, "The Science of Neural Interface Systems," Annu. Rev. Neurosci., **32**, doi: 10.1146/annurev.neuro.051508.135241, 249–266, 2009.

[9] T. E. Schlaepfer, M. X. Cohen, C. Frick, M. Kosel, D. Brodesser, N. Axmacher, A. Y. Joe, M. Kreft, D. Lenartz, and V. Sturm, "Deep brain stimulation to reward circuitry alleviates anhedonia in refractory major depression," Neuropsychopharmacology, **33**(2), doi: 10.1038/sj.npp.1301408, 368-377, 2008.

[10] V. Johansson, M. Garwicz, M. Kanje, J. Schouenborg, A. Tingström, and U. Görman, "Authenticity, depression, and deep brain stimulation," Frontiers in Integrative Neuroscience, **5**, doi: 10.3389/fnint.2011.00021, 21, 2011.

[11] S. L. Rauch, D. D. Dougherty, D. Malone, A. Rezai, G. Friehs, A. J. Fischman, N. M. Alpert, S. N. Haber, P. H. Stypulkowski, M. T. Rise, S. A. Rasmussen, and B. D. Greenberg, "A functional neuroimaging investigation of deep brain stimulation in patients with obsessive-compulsive disorder," J Neurosurg., **104**(4), doi: 10.3171/jns.2006.104.4.558, 558-565, 2006.

[12] H. Hung, S. Tsai, H. Tsai, and S. Chen, "N-of-1 trial following deep brain stimulation in a patient with obsessive-compulsive disorder," Tzu Chi Medical Journal, **24**(4), doi: 10.1016/j.tcmj.2012.04.003, 205-208, 2012.

[13] D. Rasche, M. Ruppolt, C. Stippich, A. Unterberg, and V. M. Tronnier, "Motor cortex stimulation for long-term relief of chronic neuropathic pain: A 10 year experience," Pain, **121**(1-2), doi: 10.1016/j.pain.2005.12.006, 43-52, 2006.

[14] A. Machado, M. Ogrin, J. M. Rosenow, and J. M. Henderson, "A 12-month prospective study of gasserian ganglion stimulation for trigeminal neuropathic pain," Stereotact Funct Neurosurg, **85**(5), doi: 10.1159/000103260, 216-224, 2007.

[15] S. J. Groiss, L. Wojtecki, M. Südmeyer, and A. Schnitzler, "Deep Brain Stimulation in Parkinson's Disease," Ther Adv Neurol Disord, **2**(6), doi: 10.1177/1756285609339382, 20-28, 2009.

[16] T. L. Skarpaas, and M. J. Morrell, "Intracranial Stimulation Therapy for Epilepsy," Neurotherapeutics, **6**(2), doi: 10.1016/j.nurt.2009.01.022, 238-243, 2009.

[17] J. S. Perlmutter, and J. W. Mink, "Deep Brain Stimulation," Annu. Rev. Neurosci., **29**, doi: 10.1146/annurev.neuro.29.051605.112824, 229-257, 2006.

[18] J. C. Middlebrooks, J. A. Bierer, and R. L. Snyder, "Cochlear implants: the view from the brain," Current Opinion in Neurobiology, **15**(4), doi: 10.1016/j.conb.2005.06.004, 488–493, 2005.

[19] B. Wilson, and M. Dorman, "Cochlear implants: A remarkable past and a brilliant future," Hearing Research, **242**(1-2), doi: 10.1016/j.heares.2008.06.005, 3-21, 2008.

[20] D. Yanai, J. Weiland, M. Mahadevappa, R. Greenberg, I. Fine, and M. Humayun, "Visual Performance Using a Retinal Prosthesis in Three Subjects With Retinitis Pigmentosa," American Journal of Ophtalmology, **143**(5), doi: 10.1016/j.ajo.2007.01.027, 820-827, 2007.

[21] M. Jeschke, and T. Moser, "Considering optogenetic stimulation for cochlear implants," Hearing Research, **322**, doi: 10.1016/j.heares.2015.01.005, 224-234, 2015.

[22] J. P. Donoghue, "Bridging the Brain to the World: A Perspective on Neural Interface Systems," Neuron, **60**(3), doi: 10.1016/j.neuron.2008.10.037, 511-521, 2008.

[23] J. L. Collinger, B. Wodlinger, J. E. Downey, W. Wang, E. C. Tyler-Kabara, D. J. Weber, A. J. C. McMorland, M. Velliste, L Michael, M. L. Boninger, and A. B. Schwartz, "High-performance neuroprosthetic control by an individual with tetraplegia," Lancet, **381**(9866), doi: 10.1016/S0140-6736(12)61816-9, 557-564, 2013.

[24] B. Ghane-Motlagh, and M. Sawan, "Design and Implementation Challenges of Microelectrode Arrays: A Review," Materials Sciences and Applications, **4**(8), doi: 10.4236/msa.2013.48059,

483-495, 2013.

[25] K. Cheung, "Implantable microscale neural interfaces," Biomed. Microdevices, **9**(6), doi: 0.1007/s10544-006-9045-z, 923-938, 2007.

[26] R. C. deCharms, D. T. Blake, and M. M. Merzenich, "A multielectrode implant device for the cerebral cortex," J Neurosci Methods, **93**(1), doi: 10.1016/S0165-0270(99)00087-4 27-35, 1999.

[27] K. D. Wise, D. J. Anderson, J. F. Hetke, D. R. Kipke, K. Najafi, "Wireless implantable microsystems: high-density electronic interfaces to the nervous system," Proc. IEEE, **92**(1), doi: 10.1109/JPROC.2003.820544, 76-97, 2004.

[28] P. K. Campbell, K. E. Jones, R. J. Huber, K. W. Horch, and R. A. Normann, "A silicon-based, three-dimensional neural interface: manufacturing processes for an intracortical electrode array," IEEE Trans Biomed Eng, **38**(8), doi10.1109/10.83588, 758-768, 1991.

[29] G. E. Perlin, and D. W. Kensall, "An Ultra Compact Integrated Front End for Wireless Neural Recording Microsystems," Journal of Microelectromechanical Systems, **19**(6), doi: 10.1109/JMEMS.2010.2082496, 1409-1421, 2010.

[30] A. A. A. Aarts, H. P. Neves, R. P. Puers, and C. V. Hoof, "An interconnect for out-of-plane assembled biomedical probe arrays," J. Micromech. Microeng., **18**, doi: 10.1088/0960-1317/18/6/064004, 064004, 2008.

[31] M. Y. Cheng, M. Je, K. L. Tan, E. L. Tan, R. Lim, L. Yao, P. Li, W. T. Park, E. J. R. Phua, C. L. Gan, and A. Yu, "A low-profile three-dimensional neural probe array using a silicon lead transfer structure," Journal of Micromechanics and Microengineering, **23**, doi: 10.1088/0960-1317/23/9/095013 095013, 2013.

[32] A. C. Peixoto, S. B. Goncalves, A. F. Silva, N. Dias, and J. H. Correia, "Neural electrode array based on aluminum: Fabrication and characterization," IEEE Sensors Journal, vol.13(9), doi: 10.1109/JSEN.2013.2270034, pp. 3319-3324, 2013.

[33] A. C. Peixoto, S. B. Goncalves, F. Pinho, A. F. Silva, N. S. Dias, and J. H. Correia, "Flexible three-dimensional microelectrode array for neural applications," Sensors and Actuators A: Physical, **217**, doi: 10.1016/j.sna.2014.06.020, pp. 21-28, 2014.

[34] S. B. Goncalves, A. C. Peixoto, A. F. Silva, and J. H. Correia, "Fabrication and mechanical characterization of long and different penetrating length neural microelectrode arrays," J.

Micromech. Microeng., **25**(5), doi: 10.1088/0960-1317/25/5/055014, 055014, 2015.

[35] D. Rakwal, S. Heamawatanachai, P. Tathireddy, F. Solzbacher and E. Bamberg, "Fabrication of compliant high aspect ratio silicon microelectrode arrays using micro-wire electrical discharge machining," Microsyst. Technol., **15**(5), doi: 10.1007/s00542-009-0792-7, 789–797, 2009.

[36] M. Wang, T. Maleki, and B. Ziaie, "A self-assembled 3D microelectrode array," J. Micromech. Microeng. **20**, doi: 10.1088/0960-1317/20/3/035013, 035013, 2010.

[37] S. Merriam, O. Srivannavit, M. Gulari, and K. Wise K, "A Three-Dimensional 64-Site Folded Electrode Array Using Planar Fabrication," Journal of Microelectromechanical Systems, **20**(3), doi: 10.1109/JMEMS.2011.2127450, 594-600, 2011.

[38] K. C, Cheung, P. Renaud, H. Tanila, and K. Djupsund, "Flexible Polyimide Microelectrode Array for in Vivo Recordings and Current Source Density Analysis," Biosensors & Bioelectronics, **22**(8), doi: 10.1016/j.bios.2006.08.035 1783-1790, 2007.

[39] C. Metallo, R. D. White, and B. A. Trimmer, "Flexible Parylene-Based Microelectrode Arrays for High Resolution EMG Recordings in Freely Moving Small Animals," J Neurosci Methods, **195**(2), doi: 10.1016/j.jneumeth.2010.12.005, 176-184, 2011.

[40] R. Pashaie, P. Anikeeva, J. Lee, R. Prakash, O. Yizhar, M. Prigge, D. Chander, T. J. Richner, and J. Williams, "Optogenetic Brain Interfaces," IEEE Reviews in Biomedical Engineering, **7**, doi: 0.1109/RBME.2013.2294796, 3-30, 2014.

[41] A. V. Kravitz, B. S. Freeze, P. R. L. Parker, K. Kay, M. T. Thwin, K. Deisseroth, and A. C. Kreitzer, "Regulation of parkinsonian motor behaviours by optogenetic control of basal ganglia circuitry," Nature, **466**, doi: 10.1038/nature09159, 622-626, 2010.

[42] E. M. Vazeyn, and G. Aston-Jones, "New tricks for old dogmas: Optogenetic and designer receptor insights for Parkinson's disease," Brain Research, **1511**, doi: 10.1016/j.brainres.2013.01.021, 153–163, 2013.

[43] P. Degenaar, N. Grossman, M. A. Memon, J. Burrone, M. Dawson, E. Drakakis, M. Neil, and K. Nikolic, "Optobionic vision—a new genetically enhanced light on retinal prosthesis," J Neural Eng, **6**(3), doi: 10.1088/1741-2560/6/3/035007, 035007, 2009.

[44] V. Busskamp, J. Duebel, D. Balya, M. Fradot, T. J. Viney, S. Siegert, A. C. Groner, E. Cabuy, V. Forster, M. Seeliger, M. Biel, P. Humphries, M. Paques, S. Mohand-Said, D. Trono, K. Deisseroth, J. A. Sahel, S. Picaud, and B. Roska, "Genetic Reactivation of Cone

Photoreceptors Restores Visual Responses in Retinitis Pigmentosa," Science, **329**(5990), doi: 10.1126/science.1190897, 413-417, 2010.

[45] M. M. Doroudchi, K. P. Greenberg, J. Liu, K. A. Silka, E. S. Boyden, J. A. Lockridge, A. C. Arman, R. Janani, S. E. Boye, S. L. Boye, G. M. Gordon, B. C. Matteo, A. P. Sampath, W. W. Hauswirth, and A. Horsager, "Virally delivered Channelrhodopsin-2 Safely and Effectively Restores Visual Function in Multiple Mouse Models of Blindness," The American Society of Gene & Cell Therapy, **19**(7), doi: 10.1038/mt.2011.69, 1220–1229, 2011.

[46] N. Caporale, K. D. Kolstad, T. Lee, I. Tochitsky, D. Dalkara, D. Trauner, R. Kramer, Y. Dan, E. Y. Isacoff, and J. G. Flannery, "LiGluR Restores Visual Responses in Rodent Models of Inherited Blindness," The American Society of Gene & Cell Therapy, **19**(7), doi: 10.1038/mt.2011.103, 1212–1219, 2011.

[47] B. S. Henriksen, R. E. Marc, and P. S. Bernstein, "Optogenetics for Retinal Disorders," J Ophthalmic Vis Res, **9**(3), doi: 10.4103/2008-322X.143379, 374-382, 2014.

[48] E. Macé, R. Caplette, O. Marre, A. Sengupta, A. Chaffiol, P. Barbe, M. Desrosiers, E. Bamberg, J. Sahel, S. Picaud, J. Duebel, and D. Dalkara, "Targeting Channelrhodopsin-2 to ON-bipolar Cells With Vitreally Administered AAV Restores ON and OFF Visual Responses in Blind Mice," Molecular Therapy, **23**(1), doi: 10.1038/mt.2014.154, 7-16, 2015.

[49] V. H. Hernandez, A. Gehrt, K. Reuter, Z. Jing, M. Jeschke, A. M. Schulz, G. Hoch, M. Bartels, G. Vogt, C. W. Garnham, H. Yawo, Y. Fukazawa, G. J. Augustine, E. Bamberg, S. Kügler, T. Salditt, L. de Hoz, N. Strenzke, and T. Moser, "Optogenetic stimulation of the auditory pathway," J Clin Invest, **124**(3), doi: 10.1172/JCI69050, 1114–1129, 2014.

[50] T. Moser, "Optogenetic stimulation of the auditory pathway for research and future prosthetics," Current Opinion in Neurobiology, **34**, doi: 10.1016/j.conb.2015.01.004, 29–36, 2015.

[51] W. J. Alilain, X. Li, K. P. Horn, R. Dhingra, T. E. Dick, S. Herlitze, and J. Silver, "Light-Induced Rescue of Breathing after Spinal Cord Injury," J Neurosci., **28**(46), doi: 10.1523/JNEUROSCI.3378-08.2008, 11862–11870, 2008.

[52] E. Burguière, P. Monteiro, G. Feng, and A. M. Graybiel, "Optogenetic Stimulation of Lateral Orbitofronto-Striatal Pathway Suppresses Compulsive Behaviors," Science, **340**(6137), doi: 10.1126/science.1232380, 6137, 2013.

[53] O. Yizhar, "Optogenetic Insights into Social Behavior Function," Biol Psychiatry, **71**(12), doi:

10.1016/j.biopsych.2011.12.029, 1075–1080, 2012.

[54] S. A. Allsop, C. M. V. Weele, R. Wichmann, and K. M. Tye, "Optogenetic insights on the relationship between anxiety-related behaviors and social deficits," Frontiers in Behavioral Neuroscience, **8**. doi: 10.3389/fnbeh.2014.00241, 241, 2014.

[55] P. R. Albert, "Light up your life: Optogenetics for depression?," J Psychiatry Neurosci, **39**(1). doi: 10.1503/jpn.130267, 3-5, 2014.

[56] M. K. Lobo, E. J. Nestler, and H. E. Covington III, "Potential Utility of Optogenetics in the Study of Depression," Biol Psychiatry, **71**(12), doi: 10.1016/j.biopsych.2011.12.026, 1068-1074, 2012.

[57] D. S. Roy, A. Arons, T. I. Mitchell, M. Pignatelli, T. J. Ryan, and S. Tonegawa, "Memory retrieval by activating engram cells in mouse models of early Alzheimer's disease," Nature, **531**, doi: 10.1038/nature17172, 508–512, 2016.

[58] F. Zhang, A. M. Aravanis, A. Adamantidis, L. De Lecea, and K. Deisseroth, "Circuit-breakers: optical technologies for probing neural signals and systems," Nat. Rev. Neurosci., **8**(8), doi: 10.1038/nrn2192, 577-581, 2007.

[59] M. M. Maharbiz, R. Muller, E. Alon, M. Jan, J. M. Rabaey, and J. M. Carmena, "Reliable Next-Generation Cortical Interfaces for Chronic Brain–Machine Interfaces and Neuroscience," Proceedings of the IEEE, **105**, doi: 10.1109/JPROC.2016.2574938, 73-82, 2017.

[60] F. A. C. Azevedo, L. R. B. Carvalho, L. T. Grinberg, J. M. Farfel, R. E. L. Ferretti, R. E. P. Leite, W. J. Filho, R. Lent, and S. Herculano-Houzel, "Equal numbers of neuronal and nonneuronal cells make the human brain an isometrically scaled-up primate brain," J. Comp. Neurol., **513**, doi: 10.1002/cne.21974, 532–541, 2009.

[61] B. Chow, and E. S. Boyden, "Optogenetics and Translational Medicine," Science Translational Medicine, **5**(177), doi: 10.1126/scitranslmed.3003101, 177ps5, 2013.

[62] O. Yizhar, L. Fenno, T. Davidson, M. Mogri, and K. Deisseroth, "Optogenetics in Neural Systems," Neuron, **71**(1), doi: 10.1016/j.neuron.2011.06.004, 9-34, 2011.

[63] L. Buchen, "Neuroscience: Illuminating the brain," Nature, **465**, doi: 10.1038/465026a, 26-28, 2010.

[64] F. Zhang, J. Vierock, O. Yizhar, L. E. Fenno, S. Tsunoda, A. Kianianmomeni, M. Prigge, A. Berndt, J. Cushman, J. Polle, J. Magnuson, P. Hegemann, and K. Deisseroth, "The Microbial

Opsin Family of Optogenetic Tools," Cell, **147**(7), doi: 10.1016/j.cell.2011.12.004, 1446-1457, 2011.

[65] J. Bernstein, and E. S. Boyden, "Optogenetic tools for analyzing the neural circuits of behavior," Trends in Cognitive Sciences, **15**(12), doi: 10.1016/j.tics.2011.10.003, 592-600, 2011.

[66] E. S. Boyden, "Optogenetics and the future of neuroscience," Nat. Neurosci., **18**(9), doi: 10.1038/nn.4094, 1200-1201, 2015.

[67] S. Dufour, Y. De Koninckc, "Optrodes for combined optogenetics and electrophysiology in live animals," Neurophotonics, **2**(3), doi: 10.1117/1.NPh.2.3.031205, 031205, 2015.

[68] E. S. Boyden, F. Zhang, E. Bamberg, G. Nagel, and K. Deisseroth, "Millisecond-timescale, genetically targeted optical control of neural activity," Nat. Neurosci., **8**(9), doi: 10.1038/nn1525, 1263–1268, 2005.

[69] G. Aston-Jones G, and K. Deisseroth, "Recent advances in optogenetics and pharmacogenetics," Brain Research, **1511**, doi: 10.1016/j.brainres.2013.01.026, 1–5, 2013.

[70] S. F. Cogan, "Neural Stimulation and Recording Electrodes," Annu. Rev. Biomed. Eng., **10**, doi: 10.1146/annurev.bioeng.10.061807.160518, 275-309, 2008.

[71] A. Ersen, S. Elkabes, D. S. Freedman, and M. Sahin, "Chronic tissue response to untethered microelectrode implants in the rat brain and spinal cord," J Neural Eng, **12**(1), doi: 10.1088/1741-2560/12/1/016019, 016019, 2015.

[72] A. S. Chuong, M. L. Miri, V. Busskamp, G. A. C. Matthews, L. C. Acker, A. T. Srensen, A. Young, N. C. Klapoetke, M. A. Henninger, S. B. Kodandaramaiah, M. Ogawa, S. B. Ramanlal, R. C. Bandler, B. D. Allen, C. R. Forest, B. Y. Chow, X. Han, Y. Lin, K. M. Tye, B. Roska, J. A. Cardin, and E. S. Boyden, "Noninvasive optical inhibition with a red-shifted microbial rhodopsin," Nat. Neurosci., **17**(8), doi: 10.1038/nn.3752, 1123–1129, 2014.

[73] J. G. Bernstein, X. Han, M. A. Henninger, E. Y. Ko, X. Qian, G. T. Franzesi, J. P. McConnell, P. Stern, R. Desimone, and E. S. Boyden, "Prosthetic systems for therapeutic optical activation and silencing of genetically-targeted neurons," Proc SPIE Int Soc Opt Eng, **6854**, doi: 10.1117/12.768798, 68540H, 2008.

[74] S. Ayub, C. Gossler, M. Schwaerzle, E. Klein, O. Paul, U. T. Schwarz, and P. Ruther, "High-Density Probe With Integrated Thin-Film Micro Light Emitting Diodes ($\mu$-LEDs) For Optogenetic

Applications," Proc MEMS, Shangai, China, 379-382, 2016.

[75]  R. Scharf, T. Tsunematsu, N. McAlinden, M. D. Dawson, S. Sakata, and K. Mathieson, "Depth-specific optogenetic control in vivo with a scalable, high-density $\mu$LED neural probe," Nature Scientific Reports, **8**, doi: 10.1038/srep28381, 28381, 2016.

[76]  S. Yamagiwa, M. Ishida, and T. Kawano, "Flexible Optrode Array: Parylene-Film Waveguide Arrays With Microelectrodes For Optogenetics," Transducers, Alaska, USA, doi: 10.1109/TRANSDUCERS.2015.7180915, 277-280, 2015.

[77]  T. I. Kim, J. G. McCall, Y. H. Jung, X. Huang, E. R. Siuda, Y. Li, J. Song, Y. M. Song, H. A. Pao, R. H. Kim, C. Lu, S. D. Lee, I. S. Song, G. Shin, R. Al-Hasani, S. Kim, M. P. Tan, Y. Huang, F. G. Omenetto, J. A. Rogers, and M. R. Bruchas, "Injectable, Cellular-Scale Optoelectronics with Applications for Wireless Optogenetics," Science, **340**(6129), doi: 10.1126/science.1232437, 6129, 211-216, 2013.

[78]  J. W. Jeong, J. G. McCall, G. Shin, Y. Zhang, R. Al-Hasani, M. Kim, S. Li, J. Y. Sim, K. I. Jang, Y. Shi, D. Y. Hong, Y. Liu, G. P. Schmitz, L. Xia, Z. He, P. Gamble, W. Z. Ray, Y. Huang, M. R. Bruchas, and J. A. Rogers, "Wireless Optofluidic Systems for Programmable In Vivo Pharmacology and Optogenetics," Cell, **162**(3), doi: 10.1016/j.cell.2015.06.058, 662-674, 2015.

[79]  D. Park, A. A. Schendel, S. Mikael, S. K. Brodnick, T. J. Richner, J. P. Ness, M. R. Hayat, F. Atry, S. T. Frye, R. Pashaie, S. Thongpang, Z. Ma, and J. C. Williams, "Graphene-based carbon-layered electrode array technology for neural imaging and optogenetic applications," Nature Communications, **5**, doi: 10.1038/ncomms6258, 5258, 2014.

[80]  J. C. Williams, J. A. Hippensteel, J. Dilgen, W. Shain, and D. R. Kipke, "Complex impedance spectroscopy for monitoring tissue responses to inserted neural implants," J Neural Eng., **4**(4), doi: 10.1088/1741-2560/4/4/007, 410-423, 2007.

[81]  J. Williams, and T. Denison, "From Optogenetic Technologies to Neuromodulation Therapies," Science Translational Medicine, **5**(177), doi: 10.1126/scitranslmed.3003100, 177ps6, 2013.

[82]  K. Kampasi, E. Stark, J. Seymour, K. Na, H. G. Winful, G. Buzsáki, K. D. Wise, and E. Yoon, "Fiberless multicolor neural optoelectrode for in vivo circuit analysis," Scientific Reports, **6**, doi: 10.1038/srep30961 30961, 2016.

[83]  M. W. Slutzky, L. R. Jordan, T. Krieg, M. Chen, D. J. Mogul, and L. E. Miller, "Optimal Spacing

of Surface Electrode Arrays for Brain Machine Interface Applications," J Neural Eng., **7**(22), doi: 10.1088/1741-2560/7/2/026004, 26004, 2010.

[84] C. Childs, "Human brain temperature: regulation, measurement and relationship with cerebral trauma: Part 1.," British Journal of Neurosurgery, **22**(4), doi: 10.1080/02688690802245541, 486-496, 2008.

[85] S. Kim, P. Tathireddy, R. A. Normann, and F. Solzbacher, "In vitro and in vivo study of temperature increases in the brain due to a neural implant," Proc. 3rd Int. IEEE EMBS Conference on Neural Engineering Kohala Coast, Hawaii, USA, doi: 10.1109/CNE.2007.369637, 163-166, 2007.

[86] N. McAlinden, D. Massoubre, E. Richardson, E. Gu, S. Sakata, M. D. Dawson, and K. Mathieson, "Thermal and optical characterization of micro-LED probes for in vivo optogenetic neural stimulation," Optics Letters, **38**(6), doi: 10.1364/OL.38.000992, 992-994, 2013.

[87] Y. Sun, F. Farzan, L. G. Dominguez, M. S. Barr, P. Giacobbe, A. M. Lozano, W. Wong, and Z. J. Daskalakis, "A novel method for removal of deep brain stimulation artifact from electroencephalography," J Neurosci Methods, **237**, doi: 10.1016/j.jneumeth.2014.09.002, 33-40, 2014.

[88] W. A. Martin, E. Camenzind, and P. R. Burkhard, "ECG artifact due to deep brain stimulation," The Lancet, **361**(9367), doi: 10.1016/S0140-6736(03)13136-4, 1431, 2003.

[89] J. B. Erhardt, E. Fuhrer, O. G. Gruschke, J. Leupold, M. C. Wapler, J. Hennig, T. Stieglitz, and J. G. Korvink, "Should patients with brain implants undergo MRI?" J Neural Eng, **15**(4), doi: 10.1088/1741-2552/aab4e4, 041002, 2018.

[90] B. A. Duffy, M. Choy, M. R. Chuapoco, M. Madsen, and J. H. Lee, "MRI compatible optrodes for simultaneous LFP and optogenetic fMRI investigation of seizure-like after discharges," NeuroImage, **123**, doi: 10.1016/j.neuroimage.2015.07.038, 173–184, 2015.

[91] O. G. S. Ayling, T. C. Harrison, J. D. Boyd, A. Goroshkov, and T. H. Murphy, "Automated light-based mapping of motor cortex by photoactivation of channelrhodopsin-2 transgenic mice," Nature Methods, **6**(3), doi: 10.1038/nmeth.1303 219-224, 2009.

[92] J. H. Lee, R. Durand, V. Gradinaru, F. Zhang, I. Goshen, D. Kim, L. E. Fenno, C. Ramakrishnan, and K. Deisseroth, "Global and local fMRI signals driven by neurons defined optogenetically by type and wiring," Nature, **465**, doi: 10.1038/nature09108, 788-792, 2010.

[93] M. Desai, I. Kahn, U. Knoblich, J. Bernstein, H. Atallah, A. Yang, N. Kopell, R. L. Buckner, A. M. Graybiel, C. I. Moore, and E. S. Boyden, "Mapping brain networks in awake mice using combined optical neural control and fMRI," J Neurophysiol, **105**(3), doi: 10.1152/jn.00828.2010, 1393–1405, 2011.

[94] M. T. Alt, E. Fiedler, L. Rudmann, J. S. Ordonez, P. Ruther, and T. Stieglitz, "Let There Be Light - Optoprobes for Neural Implants," Proceedings of the IEEE, **105**, doi: 10.1109/JPROC.2016.2577518, 101-138, 2017.

# Chapter 2

# Optrode Design

In this chapter will firstly be explored the current state-of-the-art for manufacturing an implantable optrode microsystem. With the knowledge acquired through this literature review, it is detailed the proposed microsystem of this thesis.

## 2.1 State-of-the-art optrodes

The requirement for light delivery in close proximity to the stimulus target can be achieved by one of three methods. Light can be generated at some distance and then guided to the local position using optical confinement with (1) optical fibers or (2) waveguides until the point of delivery. Alternatively, light can be produced locally on a penetrating or otherwise implantable device incorporating a micro-photonic element, e.g. a micro light emitting diode ($\mu$LED).

### 2.1.1 Optical fiber

Conventionally, the delivery of light into the brain to activate or silence opsin-expressing neurons relies on the insertion of an optical fiber into the brain tissue. Fibers exhibit at one end the photostimulation site, and at the opposite end it is attached or coupled to a light source. Commonly, xenon lamps [1, 2] or LED [3–5], but mostly laser diodes [6–13] are used as light power sources. The large use of lasers can be due to its high-light power output and narrowed wavelength selection.

Optical fiber-based devices have multiple designs, which are presented in Figure 2.1. One of
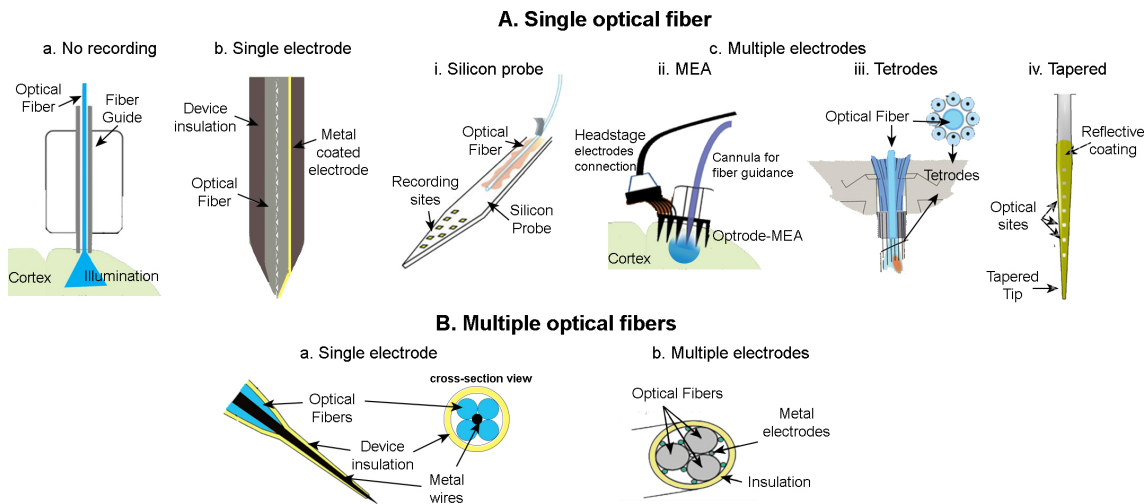
**Figure 2.1:** State-of-the-art optical fiber optrode designs. (A) Optrodes comprising single fibers for optical stimulation with: (a) no intrinsic recording (adapted from [1]); (b) single (adapted from [12]); and (c) multiple recording sites. Three single fiber optrodes showing multiple electrode combinations: optical fiber coupled to (i) Si probe (adapted from [6]); (ii) MEA (adapted from [8]); (iii) tetrode bundles (adapted from [16]); and, (iv) tapered fibers (adapted from [17]). (B) Combination of multiple optical fibers with (a) single (adapted from [9]) or (b) multiple electrodes (adapted from [18]).

the first approaches to promote photostimulation in an intact animal was performed by Aravanis et al. [1], which employed, as the channel to deliver light to neural tissue, a single optical fiber coupled to an external lamp as light source. In this design, the optical fiber is inserted with the help of a cannula for spatial guidance mounted on the animal's skull - Figure 2.1A(a). Later, Bernstein et al. [14] reported the use of a multimode fiber for simultaneous activation and inhibition, using blue and yellow light for genetically altered ChR2 and Halo/NpHR-expressing cells, respectively. More recently, Bernstein et al. [5] proposed optrodes based on arrays of optical fibers. The array design comprises more complex fabrication processes, including accurate fibers spatial distribution structures and alignment platforms for individual fiber coupling to light sources. An example of a 3D fiber array optrode was reported by Schwaerzle et al. [15], in which a stiff Si housing is used for the alignment of fibers that are coupled to a flexible substrate with integrated LEDs. Another multifiber array was also reported by Chen et al. [10], comprising a pluggable optrode structure, which takes advantage of a commercial mechanical transfer connector to facilitate fiber distribution and coupling. Although they allow the study of a larger volume of neurons, array solutions inevitably require higher complex designs and face more manufacturing challenges.

Informative data from an experimental setting are crucial, and therefore optrode designs

quickly evolved to be coupled with an appropriate quantitative readout system. Indeed, optical sites became concurrent with conventional electrical recording sites for simultaneous electrophysiology studies. Over the years, several optrode designs have been proposed, employing either single (Figure 2.1A(b)) or multiple recording sites (Figure 2.1A(c)).

The fabrication process of single recording sites conventionally includes thin-film deposition of a metallic layer over the fiber body [2, 10, 12] or a metallic wire attached to the fiber [11, 19–21], for electrophysiology recordings. These solutions that require illumination of metal electrodes might result in photoelectric artifacts [12]. In the perspective of mitigating this phenomenon, glass-based optrodes have been reported [11, 20, 22], which could prevent these undesired artifacts. Additionally, Katz et al. [23] proposed the designing of a patch pipette holder containing an additional port for the insertion of an optical fiber into the pipette (Optopatcher), allowing simultaneously intracellular recordings (patch-clamp) with direct projection of light from the recording pipette.

In contrast, fiber optrode designs with multiple electrode sites consist in hybrid solutions, relying on the integration of a single fiber unit into planar Si probes [4, 6, 13, 24], out-of-plane MEAs [2, 8], or simply tetrodes [16], as illustrated in Figure 2.1 A(c)i - A(c)iii. With high density of electrical recording sites, one is able to gather clinical data not only in the vicinity of photostimulation focus but also simultaneously in other target neural circuits. For example, in the optrode-MEA hybrid [8], the recording of extracellular neural activity occurs within an area of approximately 8 mm$^2$ around the stimulation focus. The manufacturing process of the aforementioned designs may show poor reproducibility, since manual coupling techniques are employed to attach the optical fiber to shafts or MEA. Conversely, in the optrode-tetrode approach [16], both electrode wires and optical fiber have a drive mechanism to ensure accurate guidance and alignment.

Another solution to produce multipoint optical sites consists in tapered fibers (Figure 2.1A(c)iv). In contrast to most fiber optrodes reported that are restricted to a single photostimulation site per fiber, Pisanello et al. [17] demonstrated the fabrication process of a tapered optical fiber device with multipoint optical stimulation sites. In this approach, a combination of Focused Ion Beam (FIB) and Scanning Electron Microscope (SEM) systems perform milling processes over coating layer of the fiber, resulting in the generation of multipoint optical sites used for mouse in vivo stimulation. FIB technology is here used as a tool for maskless micromachining, which enables a reproducible process with accurate geometric pits. This device does not include an intrinsic

readout solution. Instead, the tapered fiber is coupled to a commercially available planar MEA that performs extracellular recordings.

Fiber optrode designs also include multicore optical fibers [3] and clustering multiple single core optical fibers, with single [9] or multiple recording sites [18, 25]. These solutions can be seen in Figure 2.1B. The latter approach relies on the integration of optical fibers to metallic electrode wires, while the other approach is obtained by simply using multimode fiber coupling with a light power source. While enhancing light density in neurons, these designs present large dimensions (> 400 $\mu$m) by combining several fibers. Consequently, coupling light sources to each core of the optical fiber becomes a more complex process, decreasing its light power coupling efficiency. Moreover, fiber-based optrodes integrating multiple recording sites rely on manual assembly processes between optical fiber and recording metal wires, which are later inserted into guiding tubes [18, 25]. Due to scaling issues, microassembly is a highly demanding process mainly because of its complexity. As a result, this process has a low production yield and is time demanding. Manual assembly could be improved by employing a high precision pick-and-place robot with micrometer resolution to handle electrode wires. Another option for the inclusion of a readout system could be a thin-film metal coating over the optical fiber surface, as reported by Ozden et al. [12].

To summarize, optrode solutions based on optical fiber optrodes have both advantages and disadvantages. On one hand, fibers are able to reach deep neural structures by being long, flexible and lightweight structures. In addition, optical fibers are easily acquired and require few fabrication steps to produce a functional optrode. On the other hand, even though these tools ensure the separation of resistive heat-generating elements from target tissue, a study by Stujenske et al. [26] showed that high radiance light absorption from optic fiber emission can also cause localized tissue heating. Fiber optrodes might also have the need to reduce fiber dimensions (usually 200 $\mu$m) using mechanical stripping [5, 12, 21] or chemical etching processes [2, 6, 10], which aims to remove the jacket layer around the cladding or simply to obtain a tapered profile at the end of the fiber, smoothing tissue penetration during implantation time. Also, traditionally a fiber-based optical system requires a light source with an external physical connection that might hinder wireless solutions and compromise subjects' natural movements and dynamics for freely moving animal studies. In this context, Paralikar et al. [27] reported a fully hermetic, battery-powered fiber optrode with wireless communication capability.

## 2.1.2 Waveguide

As mentioned above, optical fibers present some constrains, such as the limitation of delivering light to a single target within the three-dimensional structure of the brain, unless employing array solutions. Thus, other approaches like using waveguide materials to deliver light to engineered cells have been proposed. Similar to optical fibers, these structures guide optical waves by total internal reflection. Waveguides are manufactured over the probe's body, normally by using two thin-film layers of distinctive refractive index materials, which results in a core-cladding system. This manufacturing process enhances flexibility in the optrode design, and simultaneously enables several optical stimulation sites along the probe.

Figure 2.2 shows different approaches to fabricate waveguide optrodes. Their design can be divided into two major groups: deposition of waveguide thin-films over conventional Si probes (Figure 2.2A) [7, 28–35]; and planar or out-of-plane optrodes that use waveguides as bulk material (Figure 2.2B) [36–39]. Most waveguide designs exhibit electrical recording but vary significantly in the number of shafts or in the number of photostimulation site per shaft.

Generally, the fabrication process of waveguides over Si probes includes standard microfabrication techniques, such as photolithography and chemical vapor deposition (CVD) techniques to pattern photoresist materials or chemically deposit the desired material (e.g., oxynitride, silicon oxynitride, silicon nitride, silicon dioxide, etc). SU-8, an epoxy-based negative photoresist, is the most commonly core-waveguide material used for these designs [28, 29, 32–34, 40].

Similar to the optical fiber interfaces, some waveguide designs only provide a single stimulation site per shaft [28, 30]. In order to increase the number of optical stimulation sites, multiple waveguide probes (Figure 2.2A(b)) [29, 31, 32] and planar multi-shaft waveguide arrays were proposed (Figure 2.2A(a)) for deep brain structures [7, 32, 33]. Another approach includes a manufacturing process with a sacrificial Si substrate to achieve a flexible planar parylene-film multi-waguide array for superficial neural applications [34]. Moreover, an alternative multimodality design demonstrated a polymer-based neural probe integrated with SU-8 waveguide, microelectrodes and a microfluidic channel [40].

Zorzos et al. [31] reported the fabrication process of a multiwaveguide probe capable of delivering independently light to multiple targets along the probe axis (Figure 2.2A(b)i), thus enabling
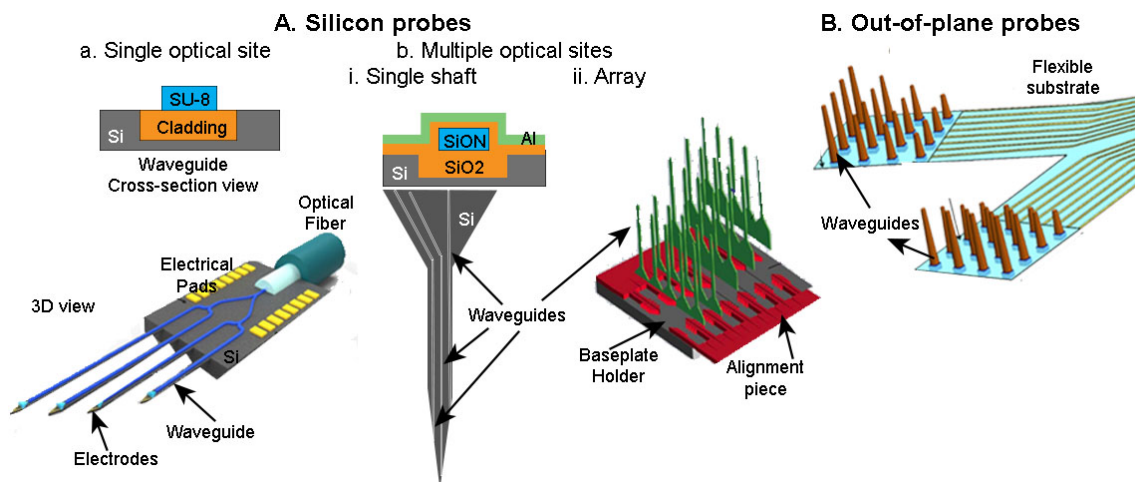
**Figure 2.2:** State-of-the-art waveguide optrode designs. (A) Waveguide layers coupled to conventional Si probes with multiple electrodes. (a) Single (adapted from [33]) and (b) multiple photostimulation sites in (i) a single shaft (adapted from [31]) and (ii) array (adapted from [7]). (B) Out-of-plane waveguides optrode (adapted from [39]).

targeting different brain layers. The final probe design with no recording capability comprised twelve parallel silicon oxynitride (SiON) rectangular waveguides (20 $\mu$m wide and 9 $\mu$m thick) with a pitch of 30 $\mu$m. Later, a three-dimensional approach of this solution (Figure 2.2A(b)ii) was also presented by fabricating waveguide combs (combination of several linear probes parallel to each other) aligned in a custom-engineered baseplate [7]. In this fabrication process, position accuracy of the combs and consequently the stimulation sites are directly dependent on the manual alignment, which could hinder result reproducibility. Yet, this seems like a highly scalable solution.

In the multipoint optical site perspective, Segev et al. [41] reported the development of a silicon nitride (SiN) waveguide-based array device, working in the visible range. This work is based on the technique of Wavelength Division (de)-Multiplexing (WDM), where the waveguide array has the ability to demultiplex the incoming light (one input) into its spectral components and guide the target wavelength through each waveguide channel (several output channels). The small footprint device (114 $\times$ 156 $\mu$m$^2$ for 9 output channels at 473 nm) was recently integrated into Si probes and validated in vivo [42]. Moreover, the waveguide array fabrication demonstrated here is fully compatible with CMOS-photonics fabrication processes.

Figure 2.2B shows out-of-plane optrode designs using waveguides as bulk material. By applying this concept, out-of-plane approaches present fabrication processes that vary between bulk material dicing or abrasion [36–38] to photolithography (Figure 2.2B) [39]. Taking advantage of the extensive

development of the UEA, it was demonstrated optical arrays suitable for optogenetics: the Utah Optrode Array (UOA) [43] and the Utah Slant Optrode Array (USOA) [36, 37]. Both approaches consit of arrays micromachined out of silicon dioxide ($SiO_2$) and silica glass wafers, respectively. Also based on the UEA fabrication methodology, Lee et al. [38] reported a $4 \times 4$ ZnO-based waveguide array used in rodent experiments. Despite having lower density of optical sites than the USOA approach, the ZnO-based device incorporates a simultaneous readout system. Kwon et al. [39] also demonstrated a slanted SU-8 optrode array with multiple photostimulation and recording sites able to reach neural circuits with different depths within a target area.

Compared with optical fiber optrodes, the probes that rely on waveguides present some key advantages. First, the waveguide-based optrode can provide multi-stimulation sites along its axis without significantly increasing the device dimensions [29, 31]. Second, the fabrication of multi-waveguides per shaft does not directly represent an increase in fabrication complexity. Finally, waveguide approaches allow more versatile design, since geometrical parameters such as thickness, width, and spacing between waveguides can be lithographically defined. Therefore, reproducible structures can be easily accomplished, enabling batch processes for waveguide optrode manufacturing. Similar to fiber optrodes, waveguide-based solutions also require external optical sources to promote photostimulation. Recent developments show integrated light sources allowing wireless device solutions [15, 35].

Waveguide optrodes show a major constraint: manual attachment of an optical fiber to the end of the waveguide. This process can be labor-intensive, time-consuming and inevitably result in alignment inaccuracy. Coupling between optical fiber and waveguide on the pathway from a laser source to the nerve cells contributes to light intensity losses in the tissue, which could compromise the activation of engineered cells. However, efforts were reported to overcome this limitation by fabricating a U-groove (set by optical fiber diameter) in the probe shafts to facilitate its alignment [28, 30, 33]. More recently, Kampasi et al. [35] reported a gradient-index (GRIN) lens system, which serves as the optical coupling medium between waveguide and light source and enhances the device optical efficiency (5.2–12%) while facilitating thermal dissipation at the back end of the device and providing adequate thermal insulation to the tissue. Nevertheless, the GRIN-waveguide optrode still presents stimulus-locked artifacts and is susceptible to angular misalignment errors between the GRIN and waveguide junction.

## 2.1.3 $\mu$LED

Optical fiber and waveguide optrodes have been stimulating engineered neural cells by means of lamps, lasers or LEDs, as external light sources. On the hand, one can directly stimulate brain tissue by the implementation of LEDs onto probes. $\mu$LEDs are drawing attention due to their low-power consumption and small sizes, which minimizes tissue damage and inflammation in chronic applications.

Current $\mu$LED optrode designs (Figure 2.3) can be categorized by planar devices for surface neural applications and by deep probes interfacing deeper brain structures. $\mu$-LEDs are either (1) monolithical manufactured onto the device structure by deposition of gallium nitride (GaN) layers on a substrate [44, 45], or (2) integrated in the probe by LED transfer techniques [46–49]. $\mu$LED fabrication process includes an anode (p-contact), a cathode (n-contact) and multiple quantum well (MQW) layers - see Figure 2.3A(b). GaN LEDs are the primary technology used in optrodes since the light required for optogenetics is primarily blue (ChR2 opsin is activated at 470 nm) and must also be high-irradiance. The emission spectrum of the LEDs depends on the indium concentration and can be tuned from violet to amber [50]. Individual addressable emitters on an array require a separated p-contact for each LED, but n-contact can be shared by all units [51].

One of the first designs consisted of a 16 $\times$ 16 array with individual addressable $\mu$LEDs, that enabled selective activation of the emitting units [52]. This feature allowed driving individual LEDs at different pulse width modulations, and thus enabled light intensity and brightness control. Also, individual addressable devices allow operation at the required output-power density with a lower voltage. This is crucial in applications where power consumption is a major factor, such as chronic implantable devices. Grossman et al. [53], by employing the same design, improved the emitters pitch to 50 $\mu$m, enhancing spatial resolution of the device - Figure 2.3A(b).

More recently, using a single photostimulation site, Park et al. [54] reported a flexible device (0.7 $\times$ 3.8 $\times$ 6 mm$^3$) for in vivo applications with lightweight construction (16 mg), capable of implantation into challenging anatomical shapes and subject's natural motions. Despite its straightforward planar geometric structure with silicone elastomer materials, the fabrication process of this device includes flexible electronic technology for a stretchable radio frequency (RF) harvesting unit, which receives and rectifies signals from a transmitter, as well as multiplies the voltages and
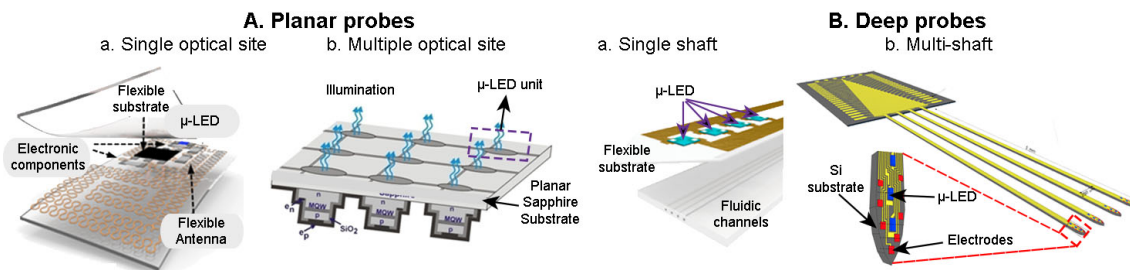
**Figure 2.3:** State-of-the-art $\mu$-LED optrode designs. (A) Planar probes for superficial applications with (a) single (adapted from [54]) and (b) multiple of photostimulation sites (adapted from [53]). (B) Deep probes with multipoint photostimulation comprising (a) single (adapted from [56]) and (b) multiple shafts (adapted from [44]).

routes the resulting direct-current output to the LED. Other approaches for cortex applications using planar flexible devices based on arrays of $\mu$LEDs were proposed, reaching maximum stimulation depths of 600 $\mu$m [46]. Moreover, a high-density $\mu$LED planar array (8100 pixels) was recently reported for retinal prosthesis applications, demonstrating thermal stability and low-power consumption, suitable for portable use [55].

Kim et al. [57] reported one of the first $\mu$LED optrode system that support deep brain tissue studies. The optrode includes a single probe with four GaN $\mu$LEDs in an epoxy substrate. This implantable multifunctional device (total thickness of 8.5 $\mu$m) combines optical stimulation with other sensors, such as electrical recording, temperature sensing and optical measurements. More importantly, this device includes a wireless communication system, enabling behavioral control over freely moving animals. Further development of this flexible design demonstrated a multimodal solution with the integration in the same probe of a multiple optical sites with microfluidic channels (Figure 2.3B(a)) [56]. As previously discussed, flexible devices need the support of hard platforms to assist the piercing process during tissue implantation. In this study, the mechanical integrity of the probe was ensured by treating brain's surface with collagenase, which required low insertion forces.

$\mu$LED Si optrodes comprehend both single or multi-shaft devices. A single-shaft optrode with multi-site photostimulation capability was reported by McAlinden et al. [58, 59]. Figure 2.3B(b) shows a four-shaft probe, each integrated with 4 $\mu$-LEDs and a total of 32 recording sites used into hippocampal layers of freely moving mice [44]. However, manufacturing these optrode designs require complex microfabrication techniques on the Si wafer: Deep Reactive Ion Etching (DRIE) and

wet etching processes to pattern substrate wafers; CVD, photolithography and lift-off techniques for selective deposition of multilayer materials [58]. Despite established MEMS technologies, the mentioned microfabrication techniques are complex with regard to parameters optimization.

The thin-film monolithical LED approach enables highly miniaturized light sources to be integrated in the probes. However, they also have drawbacks. First, GaN-based LED-wafers (sapphire or Si) techniques are expensive. Secondly, growing thin GaN layers on substrates offers limited substrate choices. Third, each LED will have the same emission wavelength, thus limiting the flexibility of probe design and application. On the other hand, the assembly process of the LED chip into a penetrating may represent a hard task and yield challenges. Cao et al. [47] proposed a polyimide single-shaft probe (12 mm long and 900 $\mu$m wide) integrating commercially available LED chip. The large dimensions of the shaft are the result of using a high-footprint $\mu$LED chip ($1 \times 0.6 \times 0.2$ mm$^3$), which in this case is the determining factor in the whole shaft design. An interesting approach to address high-footprint commercial LED chips is reported by Ayub et al. [60]. In that study, LED chips are mounted on a thin polyimide-based substrate, stiffened using a micromachined ladder-like Si structure. This approach avoids thicker probes by transfer LED chip to the surface of a stiff and thick substrate. In these cases, wider probes are necessary to accommodate wide LED chips and recording sites.

Considering these studies, advantages of using $\mu$LED optrodes to study neural circuits can be summarized. First, they eliminate external light sources, directly delivering light to the tissue, which minimizes light losses and simultaneously promote high power intensity stimulation. Secondly, to have individual addressable $\mu$LEDs enable different wavelengths, optical power, and modulation bandwidth to trigger different photosensitive cells. Finally, with this method one is able to multiplex the electronic outputs leading to a small cable. Indeed, $\mu$LED approaches show the potential to accomplish a truly untethered solution, crucial for chronic implants. Nonetheless, since $\mu$LEDs are the direct light source interface, a major concern consists in tissue damage due to overheating, and thus understanding thermal effects of the using $\mu$LEDs is important.

## 2.2   Proposed $\mu$LED optrode microsystem

The proposed design in this research consists on an $\mu$LED optrode, due to the key advantages shown in the previous section. Figure 2.4 shows a 3D optrode microsystem art-design comprising multi-electrical and optical sites. This solution is a potential approach to meet the engineering requirements previously identified. Multichannel electrical sites would enable recording and assessment of brain networks at a multilayer scale, and individual addressable $\mu$LED per shaft could provide multiple wavelengths at different optical sites. The objective of this research is to demonstrate a multifunctional probe, thus only a single-shaft probe is presented for further integration in a 3D probe array, as it can be seen in Figure 4.10. The single-shaft configuration could be assembled into a close-packed array by the stacking method reported by Chang et al [61].

Our manufacturing approach to produce this microsystem consists on low-cost semiconductor technologies, such as photolithography, thin-films deposition and blade dicing. The key advantages of these technologies are: their simplicity, commonly used in the semiconductor industry; and, fast processing time.

An optrode architecture includes optical, electrical, structural and hardware components: (i) a light source is required to activate photosensitive proteins in neurons; (ii) electrical recording sites are used for synchronized electrophysiology experiments; (iii) optical and electrical parts are assembled on a rigid or flexible platform for fixation purposes; and, finally, (iv) data acquisition, transmission and processing electronics can be external or monolithically coupled to the structural part of the device. All the main components of the proposed microsystem are detailed in the next sections.

### 2.2.1   Active Sites

Our probe includes two major active sites: (1) multiple electrical recording points, and (2) one optical stimulation site. The sites and interconnection lines and pads are accomplished by lithography and thin-film deposition techniques detailed in Chapter 3.

The recording points will directly interface with neural tissue, so they can perform the transduction of the ionic currents into electric currents. At the electrode-electrolyte interface, the electrode material requires: (1) biocompatible, (2) high resistance to corrosion, and (3) low constant impedance layers over the entire frequency range [62]. There have been reported several suitable metal-
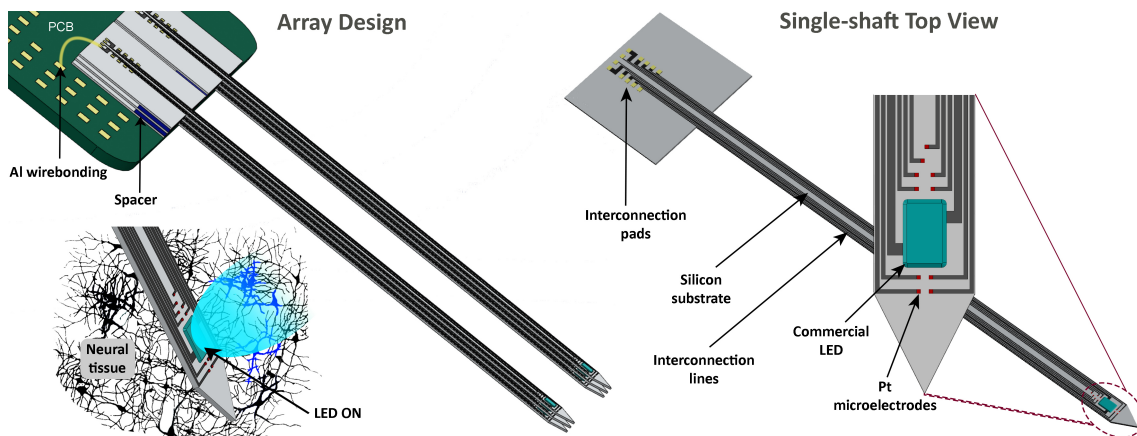
**Figure 2.4:** Design of the 3D optrode array concept (left), and detailed top view of a single-shaft probe with 10 patterned recording sites and a LED chip for electrical recording and optical stimulation, respectively.
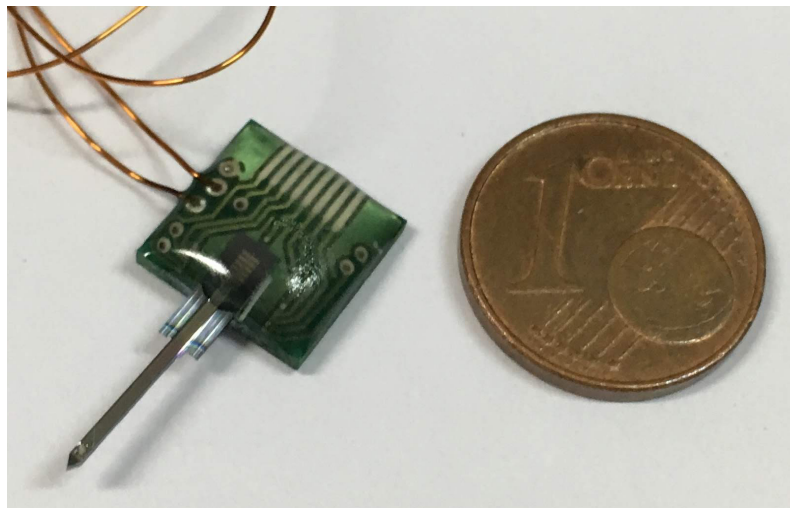


**Figure 2.5:** Final single-probe optrode microsystem next to a one-cent coin, used as a reference.

based materials, which include titanium nitride (TiN) [63], iridium oxide (IrO$_2$) [64–66], gold (Au) [67, 68], and platinum (Pt) [69, 70]. More recently, has grown the interest in using conducting polymers for neural recording and stimulation electrodes, like the poly(ethylene dioxythiophene) (PEDOT) [70–72]. In this work it was chosen Pt thin-films to interact with neural tissue, since it meets all the requirements to be used as a neural electrode and can be deposited using traditional thin-films techniques.

A commercial blue-light LED chip (ELC-470-37 [73], Roithner LaserTechnik GmbH) with dimensions of $280 \times 310 \times 85$ $\mu$m$^3$ is used as the light source, which delivers light to photosensitive engineered brain cells, so they can express the intended biological effect.

## 2.2.2 Substrate

As microtechnology developed, a wide variety of materials were explored for use as probes substrate, including Si, metals, glass, sapphire, and polymers [74]. Nevertheless, Si neural probes are still the most popular approach for developing new shaft designs in research community and also consists on the majority of solutions available in the industry.

Micromachined Si is the primary solution used in MEMS fabrication, due to the legacy of microelectronics and the resulting microfabrication equipment developed to fabricate microelectronics [75]. Moreover, it is compatible with Complementary Metal-Oxide Semiconductor (CMOS) processes and has key mechanical properties [76], such as: Low density: $2.33 \times 10^3$ Kg.m$^{-3}$; High degree of elasticity (Young's Modulus): 166 GPa, when subject to stress concentrations, as it is in this case, where stress is concentrated in the geometrical discontinuity caused by the reduction in cross-section area [77]; High degree of hardness: 11 GPa; High fracture resistance: 0.1–0.5 GPa; and, no residual stress.

In this work, the active sites are patterned over micromachined n-type [100] 525 $\mu$m/1 $\mu$m thick Si/silicon dioxide (SiO$_2$) wafers. The wafers are shaped into needle-profile shafts that serve a structural function. The shaping process is carried out by blade dicing technology, which will be explained in Chapter 3. The chosen Si doping and crystal orientation ensures the maximum shaft robustness after the cuts. The final Si device must be small enough to avoid damage in the neural tissue, but also strong enough to penetrate brain first membrane, the dura mater layer. Sharpening process of the tips is performed in order to smooth electrodes implantation procedure into brain tissue.

## 2.2.3 Encapsulation

The encapsulation layer serves a twofold purpose: (i) acts as an electrical insulator for the active sites, and (ii) ensures that a biocompatible or inert material is interfacing with the neural tissue. As previously discussed, an ineffective encapsulation layer over time can be the reason for the device failure in vivo [62]. As the device is inserted into the brain, neurons and glial cells are inevitably dislocated and damaged, creating an acute inflammatory response to the foreign body [78]. To minimize the inflammatory response, probes fabricated using non-biocompatible materials, such

as Si, need to be passivated with a biocompatible layer.

The biocompatible passivation materials reported comprehend polymers, metals and ceramics [79]. Parylene-C [80, 81] and polydimethylsiloxane (PDMS) [54, 82] are two widely polymers for encapsulation in Si neural probes. Biocompatible dielectric thin-films such as titanium oxide (TiO), silicon nitride (SiN) and alumina ($Al_2O_3$) [83–85] are alternative passivation materials over polymers. The main advantage of using thin-film materials is the prospect to fabricate thinner insulation layers using traditional deposition techniques. In this work, we use SiN thin-films, a widely choice as protective layer in Si probes [86].

### 2.2.4 Packaging

After manufacturing, the LED chip and recording sites pads of the optrode need to be connected to external hardware so the neural signals are extracted and processed. Firstly, the device is fixed to a Printed Circuit Board (PCB) using cyanoacrylate, and its contact pads are packaged by Al wire-bonding. Then, the PCB is coupled to an 18-pin connector (A79014-001 [87], Omnetics) to ensure external connectivity for all the recording sites. External connection for the LED chip is made with welded wires to PCB.

## References

[1] A. Aravanis, L. Wang, F. Zhang, L. Meltzer, M. Mogri, M. Schneider, and K. Deisseroth, "An optical neural interface: in vivo control of rodent motor cortex with integrated fiberoptic and optogenetic technology," J Neural Eng, **4**, doi: 10.1088/1741-2560/4/3/S02, S143–S156, 2007.

[2] J. Zhang, F. Laiwalla, J. A. Kim, H. Urabe, R. Wagenen, Y. Song, B. W. Connors, F. Zhang, K. Deisseroth, and A. V. Nurmikko, "Integrated device for optical stimulation and spatiotemporal electrical recording of neural activity in light-sensitized brain tissue," J Neural Eng, **6**, doi: 10.1088/1741-2560/6/5/055007, 055007, 2009.

[3] H. Xu, K. M. Davitt, W. Dong, Y. Song, W. R. Patterson III, C. D. Aizenman, and A. V. Nurmikko, "Combining Multicore Imaging Fiber With Matrix Addressable Blue/Green LED Arrays

for Spatiotemporal Photonic Excitation at Cellular Level," IEEE Journal of Selected Topics in Quantum Electronics, **14**, doi: 10.1109/JSTQE.2007.912913, 167-170, 2008.

[4] E. Stark, T. Koos, and G. Buzsáki, "Diode probes for spatiotemporal optical control of multiple neurons in freely moving animals," J Neurophysiol, **108**, doi: 10.1152/jn.00153.2012, 349–363, 2012.

[5] J. G. Bernstein, B. D. Allen, A. A. Guerra, and E. S. Boyden, "Processes for design, construction and utilisation of arrays of light-emitting diodes and light-emitting diode-coupled optical fibres for multi-site brain light delivery," J Eng (Stevenage), doi: 10.1049/joe.2014.0304, 2015.

[6] S. Royer, B. V. Zemelman, M. Barbic, A. Losonczy, G. Buzsáki, and J. C. Magee, "Multi-array silicon probes with integrated optical fibers: light-assisted perturbation and recording of local neural circuits in the behaving animal," European Journal of Neuroscience, **31**, doi: 10.1111/j.1460-9568.2010.07250.x, 2279-2291, 2010.

[7] A. N. Zorzos, J. Scholvin, E. S. Boyden, and C. G. Fonstad, "Three-dimensional multiwaveguide probe array for light delivery to distributed brain circuits," Optics Letters, **37**(23), doi: 10.1364/OL.37.004841, 4841-4843, 2012.

[8] J. Wang, F. Wagner, D. A. Borton, J. Zhang, I. Ozden, R. D. Burwell, A. V. Nurmikko, R. Wagenen, I. Diester, and K. Deisseroth, "Integrated device for combined optical neuromodulation and electrical recording for chronic in vivo applications," J Neural Eng, **9**, doi: 0.1088/1741-2560/9/1/016001, 016001, 2012.

[9] K. Tamura, Y. Ohashi, T. Tsubota, D. Takeuchi, T. Hirabayashi, M. Yaguchi, M. Matsuyama, T. Sekine, and Y. Miyashita, "A glass-coated tungsten microelectrode enclosing optical fibers for optogenetic exploration in primate deep brain structures," J Neurosci Methods, **211**, doi: 10.1016/j.jneumeth.2012.08.004, 49–57, 2012.

[10] S. Chen, W. Pei, Q. Gui, Y. Chen, S. Zhao, H. Wang, and H. Chen, "A fiber-based implantable multi-optrode array with contiguous optical and electrical sites," J Neural Eng, **10**, doi: 10.1088/1741-2560/10/4/046020, 046020, 2013.

[11] S. Dufour, G. Lavertu, S. Dufour-Beauséjour, A. Juneau-Fecteau, N. Calakos, M. Deschênes, R. Vallée, and Y. De Koninck, "A Multimodal Micro-Optrode Combining Field and Single Unit Recording, Multispectral Detection and Photolabeling Capabilities," Plos One, **8**(2), doi: 10.1371/journal.pone.0057703, e57703, 2013.

[12] I. Ozden, J. Wang, Y. Lu, T. May, J. Lee, W. Goo, D. J. O'Shea, P. Kalanithi, I. Diester, M. Diagne, K. Deisseroth, K. V. Shenoy, and A. V. Nurmikko, "A coaxial optrode as multifunction write-read probe for optogenetic studies in non-human primates," J Neurosci Methods, **219**, doi: 10.1016/j.jneumeth.2013.06.011, 142–154, 2011.

[13] H. Park, H. Shin, I. Cho, E. Yoon, J. F. Suh, M. Im, E. Yoon, Y. Kim, and J. Kim, "The First Neural Probe Integrated with Light Source (Blue Laser Diode) for Optical Stimulation and Electrical Recording," IEEE 33$^{rd}$ Annual International Conference of the Engineering in Medicine & Biology Society, Boston, USA, doi: 10.1109/IEMBS.2011.6090813 2961-2964, 2011.

[14] J. G. Bernstein, X. Han, M. A. Henninger, E. Y. Ko, X. Qian, G. T. Franzesi, J. P. McConnell, P. Stern, R. Desimone, and E. S. Boyden, "Prosthetic systems for therapeutic optical activation and silencing of genetically-targeted neurons," Proc SPIE Int Soc Opt Eng, **6854**, doi: 10.1117/12.768798, 68540H, 2008.

[15] M. Schwaerzle, P. Elmlinger, O. Paul, and P. Ruther, "Miniaturized 3×3 Optical Fiber Array for Optogenetics With Integrated 460 nm Light Sources and Flexible Electrical Interconnection," Conf Proc MEMS, Estoril, Portugal, doi: 10.1109/MEMSYS.2015.7050911, 162-165, 2015.

[16] J. Voigts, J. H. Siegle, D. L. Pritchett, and C. I. Moore, "The flexDrive: an ultra-light implant for optical control and highly parallel chronic recording of neuronal ensembles in freely moving mice," Frontiers in Systems Neuroscience, **7**, doi: 10.3389/fnsys.2013.00008, 8, 2013.

[17] F. Pisanello, L. Sileo, I. A. Oldenburg, M. Pisanello, L. Martiradonna, J. A. Assad, B. L. Sabatini, and M. Vittorio, "Multipoint-Emitting Optical Fibers for Spatially Addressable In Vivo Optogenetics," Neuron, **82**, doi: 10.1016/j.neuron.2014.04.041, 1245-1254, 2014.

[18] Y. Hayashi, Y. Tagawa, S. Yawata, S. Nakanishi, and K. Funabiki, "Spatio-temporal control of neural activity in vivo using fluorescence microendoscopy," European Journal of Neuroscience, **36**, doi: 10.1111/j.1460-9568.2012.08191.x, 2722–2732, 2012.

[19] V. Gradinaru, K. R. Thompson, F. Zhang, M. Mogri, K. Kay, M. B. Schneider, and K. Deisseroth, "Targeting and Readout Strategies for Fast Optical Neural Control In Vitro and In Vivo," J Neurosci, **27**(52), doi: 10.1523/JNEUROSCI.3578-07.2007, 14231-14238, 2007.

[20] Y. LeChasseur, S. Dufour, G. Lavertu, C. Bories, M. Deschênes, R. Vallée, and Y. De Koninck, "A microprobe for parallel optical and electrical recordings from single neurons in vivo," Nature methods, **8**(4), doi: 10.1038/nmeth.1572, 319-325, 2011.

[21] B. A. Duffy, M. Choy, M. R. Chuapoco, M. Madsen, and J. H. Lee, "MRI compatible optrodes for simultaneous LFP and optogenetic fMRI investigation of seizure-like after discharges," NeuroImage, **123**, doi: 10.1016/j.neuroimage.2015.07.038 173–184, 2015.

[22] A. Canales, X. Jia, U. P. Froriep, R. A. Koppes, C. M. Tringides, J. Selvidge, C. Lu, C. Hou, L. Wei, Y. Fink, and P. Anikeeva, "Multifunctional fibers for simultaneous optical, electrical and chemical interrogation of neural circuits in vivo," Nature Biotechnology, **33**, doi: 10.1038/nbt.3093, 277-284, 2015.

[23] Y. Katz, O. Yizhar, J. Staiger, and I. Lampl, "Optopatcher—An electrode holder for simultaneous intracellular patch-clamp recording and optical manipulation," J Neurosci Methods, **214**, doi: 10.1016/j.jneumeth.2013.01.017, 113–117, 2003.

[24] E. Kim, H. Tu, H. Luo, B. Liu, S. Bao, J. Zhang, and Y. Xu, "3D Silicon Neural Probe with Integrated Optical Fibers for Optogenetic Modulation," Lab Chip, **15**(14), doi: 10.1039/c4lc01472c, 2939-2949, 2015.

[25] P. Anikeeva, A. S. Andalman, I. Witten, M. Warden, I. Goshen, L. Grosenick, L. A. Gunaydin, L. M. Frank, and K. Deisseroth, "Optetrode: a multichannel readout for optogenetic control in freely moving mice," Nature Neuroscience, **15**(1), doi: 10.1038/nn.2992, 163-170, 2012.

[26] J. M. Stujenske, T. Spellman, and J. A. Gordon, "Modeling the spatiotemporal dynamics of light and heat propagation for in vivo optogenetics," Cell Rep, **12**(3), doi: 10.1016/j.celrep.2015.06.036, 525-534, 2015.

[27] K. J. Paralikar, P. Cong, O. Yizhar, L. F. Fenno, W. Santa, C. Nielsen, D. Dinsmoor, B. Hocken, G. O. Munns, J. Giftakis, K. Deisseroth, and T. Denison, "An Implantable Optical Stimulation Delivery System for Actuating an Excitable Biosubstrate," IEEE J Solid-State Circuits, **46**(1), doi: 10.1109/JSSC.2010.2074110, 321-332, 2011.

[28] I. Cho, H. Baac, and E. Yoon, "A 16-site neural probe integrated with a waveguide for optical stimulation," $23^{rd}$ IEEE International Conference on Micro Electro Mechanical Systems (MEMS), Wanchai, Hong Kong, China, doi: 10.1109/MEMSYS.2010.5442376, 995-998, 2010.

[29] M. Im, I. Cho, F. Wu, K. D. Wise, and E. Yoon, "A Dual-Shank Neural Probe Integrated with Double Waveguides on Each Shank for Optogenetic Applications," IEEE $33^{rd}$ Annual International Conference of the Engineering in Medicine & Biology Society, Boston, USA, doi: 10.1109/IEMBS.2011.6091398, 5480-5483, 2011.

[30] F. Wu, E. Stark, M. Im, I. Cho, E. Yoon, G. Buzsáki, K. D. Wise, and E. Yoon, "An implantable neural probe with monolithically integrated dielectric waveguide and recording electrodes for optogenetics applications," J Neural Eng, **10**(5), doi: 10.1088/1741-2560/10/5/056012, 056012, 2013.

[31] A. N. Zorzos, E. S. Boyden, and C. G. Fonstad, "Multiwaveguide implantable probe for light delivery to sets of distributed brain targets," Optics Letters, **35**(24), doi: 10.1364/OL.35.004133, 4133-4135, 2010.

[32] M. Schwaerzle, K. Seidl, U. T. Schwarz, O. Paul, and P. Ruther, "Ultracompact Optrode With Integrated Laser Diode and SU-8 Waveguides for Optogenetic Applications," IEEE $26^{th}$ International Conference on Micro Electro Mechanical Systems (MEMS), Taipei, Taiwan, doi: 10.1109/MEMSYS.2013.6474424, 1029-1032, 2013.

[33] Y. Son, H. J. Lee, J. Kim, H. Shin, N. Choi, C. J. Lee, E. Yoon, E. Yoon, K. D. Wise, T. G. Kim, and I. Cho, "In vivo optical modulation of neural signals using monolithically integrated two-dimensional neural probe arrays," Scientific Reports, **5**, doi: 10.1038/srep15466, 15466, 2015.

[34] S. Yamagiwa, M. Ishida, and T. Kawano, "Flexible Optrode Array: Parylene-Film Waveguide Arrays With Microelectrodes For Optogenetics," Transducers, Alaska, USA, doi: 10.1109/TRANSDUCERS.2015.7180915, 277-280, 2015.

[35] K. Kampasi, D. F. English, J. Seymour, E. Stark, S. McKenzie, M. Vöröslakos, G. Buzsáki, K. D. Wise, and E. Yoon, "Dual color optogenetic control of neural populations using low-noise, multishank optoelectrodes," Microsystems & Nanoengineering, **4**, doi: 10.1038/s41378-018-0009-2, 10, 2018.

[36] T. V. F. Abaya, M. Diwekar, S. Blair, P. Tathireddy, L. Rieth, G. A. Clark, and F. Solzbacher, "Characterization of a 3D optrode array for infrared neural stimulation," Biomedical Optics Express, **3**(9), doi: 10.1364/BOE.3.002200, 2200-2219, 2012.

[37] T. V. F. Abaya, S. Blair, P. Tathireddy, L. Rieth, and F. Solzbacher, "A 3D glass optrode array for optical neural stimulation," Biomedical Optics Express, **3**(12), doi: 10.1364/BOE.3.003087, 3087-3104, 2013.

[38] J. Lee, I. Ozden, Y. Song, and A. V. Nurmikko, "Transparent intracortical microprobe array for simultaneous spatiotemporal optical stimulation and multichannel electrical recording," Nat

Meth, **12**(12), doi: 10.1038/nmeth.3620, 1157-1162, 2015.

[39] K. Y. Kwon, H. Lee, M. Ghovanloo, A. Weber, and W. Li, "Design, fabrication, and packaging of an integrated, wirelessly-powered optrode array for optogenetics application," Front. Syst. Neurosci., **9**, doi: 10.3389/fnsys.2015.00069, 69, 2015.

[40] B. Rubehn, S. Wolff, P. Tovote, A. L*ü*thi, and T. Stieglitz, "A polymer-based neural microimplant for optogenetic applications: design and first in vivo study," Lab Chip, **13**, doi: 10.1039/c2lc40874k, 579–588, 2013.

[41] E. Segev, T. Fowler, A. Faraon, and M. L. Roukes, "Visible Array Waveguide Gratings for Applications of Optical Neural Probes," Proc. SPIE, **9305**, doi: 10.1117/12.2078599, 93052L, 2015.

[42] E. Segev, J. Reimer, L. C. Moreaux, T. M. Fowler, D. Chi, W. D. Sacher, M. Lo, K. Deisseroth, A. S. Tolias, A. Faraon, and M. L. Roukes, "Patterned photostimulation via visible-wavelength photonic probes for deep brain optogenetics," Neurophoton, **4**(1), doi: 10.1117/1.NPh.4.1.011002, 011002, 2016.

[43] R. W. Boutte, and S. Blair, "Maskless wafer-level microfabrication of optical penetrating neural arrays out of soda-lime glass: Utah Optrode Array," Biomed Microdevices, **18**, doi: 10.1007/s10544-016-0140-5, 115, 2016.

[44] F. Wu, E. Stark, P. Ku, K. D. Wise, G. Buzs*á*ki, and E. Yoon, "Monolithically Integrated $\mu$LEDs on Silicon Neural Probes for High-Resolution Optogenetic Studies in Behaving Animals," Neuron, **88**, doi: 10.1016/j.neuron.2015.10.032, 1–13, 2015.

[45] R. Scharf, T. Tsunematsu, N. McAlinden, M. D. Dawson, S. Sakata, and K. Mathieson, "Depth-specific optogenetic control in vivo with a scalable, high-density $\mu$LED neural probe," Nature Scientific Reports, **8**, doi: 10.1038/srep28381, 28381, 2016.

[46] K. Y. Kwon, B. Sirowatka, A. Weber, and W. Li, "Opto-$\mu$EcoG Array: A Hybrid Neural Interface With Transparent $\mu$EcoG Electrode Array and Integrated LEDs for Optogenetics," IEEE Transactions on Biomedical Circuits and Systems, Rotterdam, Netherlands, **7**(5), doi: 10.1109/TBCAS.2013.2282318, 593-600, 2013.

[47] H. Cao, L. Gu, S. K. Mohanty, and J. C. Chiao, "An Integrated $\mu$-LED Optrode for Optogenetic Stimulation and Electrical Recording," IEEE Transaction on Biomedical Engineering, **60**(1), doi: 10.1109/TBME.2012.2217395, 225-229, 2013.

[48] S. Ayub, C. Gossler, M. Schwaerzle, E. Klein, O. Paul, U. T. Schwarz, and P. Ruther, "High-Density Probe With Integrated Thin-Film Micro Light Emitting Diodes ($\mu$-LEDs) For Optogenetic Applications," Proc MEMS, Shangai, China, 379-382, 2016.

[49] C. Go$\beta$ler, C. Bierbrauer, R. Moser, M. Kunzer, K. Holc, W. Pletschen, K. K$\ddot{o}$hler, J. Wagner, M. Schwaerzle, P. Ruther, O. Paul, J. Neef, D. Keppeler, G. Hoch, T. Moser, and U. T. Schwarz, "GaN-based micro-LED arrays on flexible substrates for optical cochlear implants," J. Phys. D: Appl. Phys, **47**, doi: 10.1088/0022-3727/47/20/205401, 205401, 2014.

[50] Y. Lai, C. Liu, and Z. Chen, "Tuning the emitting wavelength of InGaN/GaN superlattices from blue, green to yellow by controlling the size of InGaN quasi-quantum dot," Thin Solid Films, **498**, doi: 10.1016/j.tsf.2005.07.090, 128–132, 2006.

[51] J. J. D. McKendry, D. Massoubre, S. Zhang, B. R. Rae, R. P. Green, E. Gu, R. K. Henderson, A. E. Kelly, and M. D. Dawson, "Visible-Light Communications Using a CMOS-Controlled Micro-LightEmitting-Diode Array," J Lightwave Technology, **30**(1), doi: 10.1109/JLT.2011.2175090, 61-67, 2011.

[52] B. McGovern, R. B. Palmini, N. Grossman, E. M. Drakakis, V. Poher, M. A. A. Neil, and P. Degenaar, "A New Individually Addressable Micro-LED Array for Photogenetic Neural Stimulation," IEEE Transactions on Biomedical Circuits and Systems, Paphos, Cyprus, **4**(6), doi: 10.1109/TBCAS.2010.2081988, 469-476, 2010.

[53] N. Grossman, V. Poher, M. S. Grubb, G. T. Kennedy, K. Nikolic, B. McGovern, R. B. Palmini, Z. Gong, E. M. Drakakis, M. A. A. Neil, M. D. Dawson, J. Burrone, and P. Degenaar, "Multi-site optical excitation using ChR2 and micro-LED array," J Neural Eng, **7**, doi: 10.1088/1741-2560/7/1/016004, 016004, 2010.

[54] S. I. Park, D. S. Brenner, G. Shin, C. D. Morgan, B. A. Copits, H. U. Chung, M. Y. Pullen, K. N. Noh, S. Davidson, S. J. Oh, J. Yoon, K. I. Jang, V. K. Samineni, M. Norman, J. G. Grajales-Reyes, S. K. Vogt, S. S. Sundaram, K. M. Wilson, J. S. Ha, R. Xu, T. Pan, T. I. Kim, Y. Huang, M. C. Montana, J. P. Golden, M. R. Bruchas, R. W. Gereau, and J. A. Rogers, "Soft, stretchable, fully implantable miniaturized optoelectronic systems for wireless optogenetics," Nature Biotechnology, **12**, doi: 10.1038/nbt.3415, 1280-1286, 2015.

[55] A. Soltan, B. McGovern, E. Drakakis, M. Neil, P. Maaskant, M. Akhter, J. S. Lee, and P. Degenaar, "High density, high radiance $\mu$LED matrix for optogenetic retinal prostheses and

planar neural stimulation," IEEE Transactions on Biomedical Circuits and Systems, **11**(2), doi: 10.1109/TBCAS.2016.2623949, 1-13, 2016

[56] J. W. Jeong, J. G. McCall, G. Shin, Y. Zhang, R. Al-Hasani, M. Kim, S. Li, J. Y. Sim, K. I. Jang, Y. Shi, D. Y. Hong, Y. Liu, G. P. Schmitz, L. Xia, Z. He, P. Gamble, W. Z. Ray, Y. Huang, M. R. Bruchas, and J. A. Rogers, "Wireless Optofluidic Systems for Programmable In Vivo Pharmacology and Optogenetics," Cell, **162**(3), doi: 10.1016/j.cell.2015.06.058, 662-674, 2015.

[57] T. I. Kim, J. G. McCall, Y. H. Jung, X. Huang, E. R. Siuda, Y. Li, J. Song, Y. M. Song, H. A. Pao, R. H. Kim, C. Lu, S. D. Lee, I. S. Song, G. Shin, R. Al-Hasani, S. Kim, M. P. Tan, Y. Huang, F. G. Omenetto, J. A. Rogers, and M. R. Bruchas, "Injectable, Cellular-Scale Optoelectronics with Applications for Wireless Optogenetics," Science, **340**(6129), doi: 10.1126/science.1232437, 6129, 211-216, 2013.

[58] N. McAlinden, D. Massoubre, E. Richardson, E. Gu, S. Sakata, M. D. Dawson, and K. Mathieson, "Thermal and optical characterization of micro-LED probes for in vivo optogenetic neural stimulation," Optics Letters, **38**(6), doi: 10.1364/OL.38.000992, 992-994, 2013.

[59] N. McAlinden, E. Gu, M. D. Dawson, S. Sakata, and K. Mathieson, "Optogenetic activation of neocortical neurons in vivo with a sapphire-based micro-scale LED probe," Frontiers in Neural Circuits, **9**, doi: 10.3389/fncir.2015.00025, 25, 2015.

[60] S. Ayub, L. J. Gentet, R. Fiàth, M. Schwaerzle, M. Borel, F. David, P. Barthó, I. Ulbert, O. Paul, and P. Ruther, "Hybrid intracerebral probe with integrated bare LED chips for optogenetic studies," Biomed Microdevices, **19**, doi: 10.1007/s10544-017-0190-3, 49, 2017.

[61] C. Chang, and J. Chiou, "Development of a Three Dimensional Neural Sensing Device by a Stacking Method," Sensors, **2010**, 10, doi: 10.3390/s100504238, 4238-4252, 2010.

[62] S. F. Cogan, "Neural Stimulation and Recording Electrodes," Annu. Rev. Biomed. Eng., **10**, doi: 10.1146/annurev.bioeng.10.061807.160518, 275-309, 2008.

[63] A. Ivorra, R. Gòmez, N. Noguera, R. Villa, A. Sola, L. Palacios, G. Hotter, and J. Aguilò, "Minimally invasive silicon probe for electrical impedance measurements in small animals," Biosens. Bioelectron., **19**(4), doi: 10.1016/S0956-5663(03)00204-5, 391-399, 2003.

[64] R. B. McIntosh, P. E. Mauger, and S. R. Patterson, "Capacitive transducers with curved electrodes," IEEE Sensors J., **6**(1), doi: 10.1109/JSEN.2005.854137, 125-138, 2006.

[65]  B. Wessling, W. Mokwa, and U. Schnakenberg, "RF-sputtering of iridium oxide to be used as stimulation material in functional medical implants," J. Micromech. Microeng., **16**(6), doi: 10.1088/0960-1317/16/6/S21, 142-148, 2006.

[66]  S. Negi, R. Bhandari, L. Rieth, R. Van Wagenen, and F. Solzbacher, "Neural Electrode Degradation from Continuous Electrical Stimulation: Comparison of Sputtered and Activated Iridium Oxide," J Neurosci Methods, **186**(1), doi: 10.1016/j.jneumeth.2009.10.016, 8, 2010.

[67]  J. Scholvin, J.P. Kinney, J.G. Bernstein, C. Moore-Kochlacs, N. Kopell, C.G. Fonstad, and E.S. Boyden, "Close-Packed Silicon Microelectrodes for Scalable Spatially Oversampled Neural Recording," IEEE Trans Biomed Eng., **63**(1), doi: 10.1109/TBME.2015.2406113, 120-130, 2016.

[68]  J. E. Ferguson, C. Boldt, and A. D Redish, "Creating low-impedance tetrodes by electroplating with additives," Sens Actuators A Phys., **156**(2), doi: 10.1016/j.sna.2009.10.001, 388-393, 2009.

[69]  C. de Haro, R. Mas, G. Abadal, J. Muñoz, F. Perez-Murano, C. Domínguez, "Electrochemical platinum coatings for improving performance of implantable microelectrode arrays," Biomaterials, **23**, doi: 10.1016/S0142-9612(02)00195-3, 4515-4521, 2002.

[70]  R. A. Green, P. B. Matteucci, R. T. Hassarati, B. Giraud, C. W. D. Dodds, S. Chen, P. J. Byrnes-Preston, G. J. Suaning, L. A. Poole-Warren, and N. H. Lovell, "Performance of conducting polymer electrodes for stimulating neuroprosthetics," J Neural Eng, **10**, doi: 10.1088/1741-2560/10/1/016009, 016009, 2013.

[71]  S. Venkatraman, J. Hendricks, Z. A. King, A. J. Sereno, S. Richardson-Burns, D. Martin, and J. M. Carmena, "In Vitro and In Vivo Evaluation of PEDOT Microelectrodes for Neural Stimulation and Recording," IEEE Trans Neural Systems and Rehabilitation Engineering, **19**(3), doi: 10.1109/TNSRE.2011.2109399, 307-316, 2011.

[72]  X. Cui, and D. C. Martin, "Electrochemical deposition and characterization of poly(3,4-ethylenedioxythiophene) on neural microelectrode arrays," Sensors and Actuators B, **89**, doi: 10.1016/S0925-4005(02)00448-3, 92-102, 2003.

[73]  Roithner LaserTechnik GmbH. ELC-470-34 Datasheet. `http://www.roithner-laser.com/datasheets/led_chip/elc-470-34.pdf` [Accessed on October 2018]

[74]  K. D. Wise, A. M. Sodagar, Y. Yao, M. N. Gulari, G. E. Perlin, and K. Najafi,

"Microelectrodes, Microelectronics, and Implantable Neural Microsystems," Proc IEEE, **96**(7), doi: 10.1109/JPROC.2008.922564, 1184-1202, 2008.

[75] R. N. Dean, and A. Luque, "Applications of Microelectromechanical Systems in Industrial Processes and Services," IEEE Trans. Ind. Electron., **56**(4), doi: 10.1109/TIE.2009.2013691, 913-925, 2009."

[76] K. E. Petersen, "Silicon as a Mechanical Material," Proceedings of the IEEE, **70**(5), doi: 10.1109/PROC.1982.12331, 420-457, 1982.

[77] M. A. Hopcroft, W. D. Nix, and T. W. Kenny, "What is the Young's Modulus of Silicon?" Journal of Microelectromechanical Systems, **19**(2), doi: 10.1109/JMEMS.2009.2039697, 229-238, 2010.

[78] V. S. Polikov, P. A. Tresco, and W. M. Reichert, "Response of brain tissue to chronically implanted neural electrodes," J. Neurosci. Methods, **148**(1), doi: 10.1016/j.jneumeth.2005.08.015, 1-18, 2005.

[79] D. Mihov and B. Katerska, "Some biocompatible materials used in medical practice," Trakia J. Sci., **8**(8), doi: 10.13040/IJPSR.0975-8232.7(7).2748-55, 119-125, 2010.

[80] H. Y. Lai, L. D. Liao, C. T. Lin, J. H. Hsu, X. He, Y. Y. Chen, J. Y. Chang, H. F. Chen, S. Tsang, and Y. Y. Shih, "Design, simulation and experimental validation of a novel flexible neural probe for deep brain stimulation and multichannel recording," J Neural Eng, **9**(3), doi: 10.1088/1741-2560/9/3/036001, 36001, 2012.

[81] J. Du, M. L. Roukes, and S. C. Masmanidis, "Dual-side and three-dimensional microelectrode arrays fabricated from ultra-thin silicon substrates," J. Micromechanics Microengineering, **19**(7), doi: 10.1088/0960-1317/19/7/075008, 75008, 2009.

[82] S. P. Lacour, S. Benmerah, E. Tarte, J. FitzGerald, J. Serra, S. McMahon, J. Fawcett, O. Graudejus, Z. Yu, B. Morrison III, "Flexible and stretchable micro-electrodes for in vitro and in vivo neural interfaces," Med. Biol. Eng. Comput., **48**(10), doi: 10.1007/s11517-010-0644-8, 945-954, 2010.

[83] D. S. Finch, T. Oreskovic, K. Ramadurai, C. F. Herrmann, S. M. George, and R. L. Mahajan, "Biocompatibility of atomic layer-deposited alumina thin films," J. Biomed. Mater. Res. Part A, **87A**(1), doi: 10.1002/jbm.a.31732, 100-106, 2008.

[84] A. Neumann, T. Reske, M. Held, K. Jahnke, C. Ragoss, and H. R. Maier, "Comparative

investigation of the biocompatibility of various silicon nitride ceramic qualities in vitro," J. Mater. Sci. Mater. Med., **15**(10), doi: 10.1023/B:JMSM.0000046396.14073.92, 1135-1140, 2004.

[85] M. Casaletto, G. Ingo, S. Kaciulis, G. Mattogno, L. Pandolfi, and G. Scavia, "Surface studies of in vitro biocompatibility of titanium oxide coatings," Appl. Surf. Sci., **172**(1–2), doi: 10.1016/S0169-4332(00)00844-8, 167-177, 2001.

[86] P. Fattahi, "A Review of Organic and Inorganic Biomaterials for Neural Interfaces," Adv Mater, **26**12, doi: 10.1002/adma.201304496, 1846-1885, 2014.

[87] Omnetics. A79014-001 Connector Datasheet. `https://www.omnetics.com/Portals/0/Files/PartNo/A79014-001.pdf` [Accessed on October 2018]

# Chapter 3

# Microfabrication and Testing

In this chapter is presented the microfabrication technologies used for the development process of the proposed optrode system. Moreover, in vitro validation techniques are explained. The setups and parameters used during the manufacturing and characterization measurements are also detailed here.

## 3.1 Manufacturing Technologies

### 3.1.1 Blade Dicing

Blade dicing is a purely mechanical process widely used in the separation of Si wafers into individual chips/devices both in semiconductor and micro-electro-mechanical systems (MEMS) technologies [1, 2]. In the optrode manufacturing process, blade dicing has twofold purpose: (i) cut Si wafers into rectangular profile samples where fabrication process is made, and (ii) shape final single-shaft probes. The final shafts play a structural role, granting mechanical robustness to the final device. The aim is to fabricate long shaft probes (8 mm) that enable reaching deep and hard accessible neural brain structures.

All the cuts were performed in a dicing saw machine, model DAD-2H/6T (DISCO Corporation) – Figure 3.1. Dicing saw equipment uses saw blades, at a constant rotational speed (3.000 rpm) to perform cuts on the substrate. The cuts were performed using Z09 blade (DISCO Z09 SD2000 Y1 120 60 × 0.25A3 × 40 × 60E V), suitable for Si wafer dicing [3]. It is important to note that

blade datasheet specifies a theoretical thickness of 250 $\mu$m, but the presence of synthetic diamond particles in one the blade sides results in experimental cuts with a thickness of approximately 400 $\mu$m. This value is important since it defines minimum space between two consecutive cuts. Cut speed was maintained to the minimum (0.3 mm.s$^{-1}$), due to the fragile nature of the designs being produced.

The cutting process includes setting up various parameters. Table 3.1 shows the list of parameters and the respective function. Two preparation steps are required for cutting: 1) Calibration of the blade height (Z-axis level), measured from a reference level (surface of the chuck table – see Figure 3.1b). This is accomplished by promoting electrical contact between the blade edge and the chuck surface. Z-axis calibration determines when Z = 0 and sets the maximum cut depth of the blade; 2) Substrate must be properly fixed to the chuck, avoiding misalignment issues. Si wafers rest on an adhesive layer, which is vacuum-fixed to the chuck through vacuum pits. After substrate immobilization, they are placed and aligned using a double lens microscope, equipped with two 15 W lamps.

After the preparation steps, cutting parameters can be defined: 1) Cutting speed, which
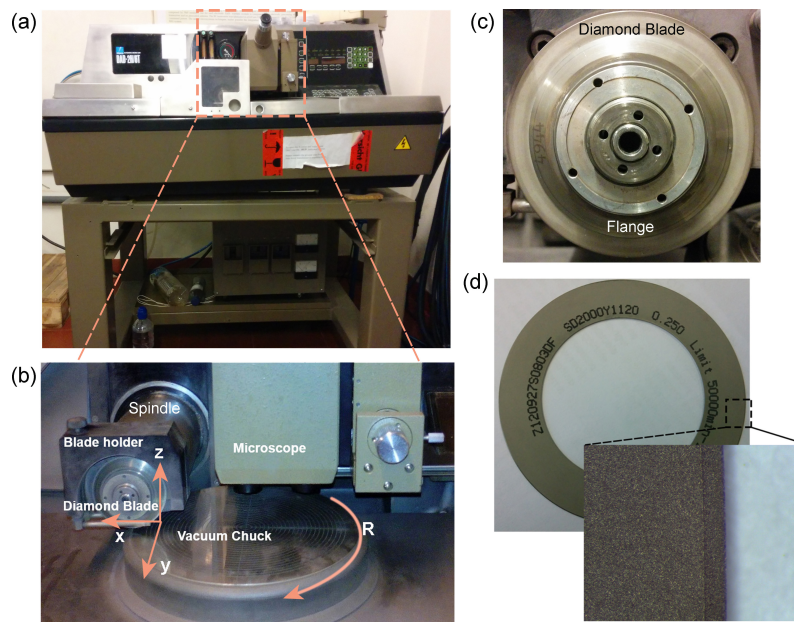


**Figure 3.1:** Blade cutting setup. (a) Photo of the dicing saw equipment. (b) Saw blade setup. (c) Blade mounting surface, and (d) photo of Z09 blade used in the cutting steps. Zoom images were performed with a LeicaM80$^{TM}$ stereo microscope.

**Table 3.1:** Parameters and respective function for a cutting program.

| Parameter | Function |
|---|---|
| Cutting speed | Determines how fast samples are diced |
| Y-axis step | Defines distance between two cuts |
| Z-axis step | Defines the depth of cuts |
| X-axis step | Defines length of the cuts |
| Blade thickness | Minimum space between two cuts. Experimental values of blade thickness usually exceed theoretical value. |

determines how fast samples are pressed against the saw blade; 2) Y-axis step, which determines the distance between two cuts; 3) Z-axis step, which determines the depth of cut; and, 4) X-axis step, which sets its length. The combination of these parameters represents a unique cutting program. The cutting programs are performed automatically, changing parameters depending on the fabrication step. After finishing each sequence of steps, the program repeats itself until the entire wafer is diced.

A substantial amount of heat within the blade is created during the dicing process, and thus a suitable cooling method (deionized water jet) is used to keep the blade at low temperature and ensure that the wheel does not lose its structural integrity. The use of deionized water ensures that substrate is free of ionic contamination. After dicing, a nitrogen spray gun can be used to dry off samples and chuck.

## 3.1.2  Photolithography

Photolithography is a standard method used in semiconductors industry and its objective is to transfer geometric patterns to a film or substrate. There are multiple steps within this process in order to get to the final geometry into the wafer [4]:

1. Clean the wafer. This step serves to remove impurities from the wafer surface and enhances adhesion to substrate.

2. Deposition of a photoresist (PR) layer, applied by a spin coating method in order to be evenly
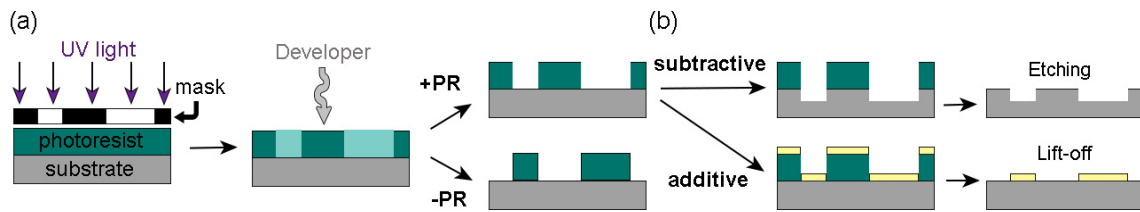
**Figure 3.2:** (a) Transfer of a pattern to a photosensitive (PR) material. Using a positive photoresist (+PR), the developer solution removes the material exposed to the UV light, while a negative photoresist (-PR) the process is the opposite. (b) Pattern transfer from patterned PR to underlying layer by etching (top) or lift-off technique (bottom).

thick throughout the entire wafer surface. There are two type of PR: positive and negative. With a positive PR (+PR), the mask contains an exact copy of the pattern which is to remain on the wafer and negative resists (-PR) behaves exactly opposite of this, i.e., the negative resist will contain an inverse of the pattern to be transferred. Figure 3.2(a) illustrates the different PR mechanisms.

3. Soft baking process. This step serves to remove all the solvents from the photoresist coating and to make the photoresist layers become photosensitive.

4. Mask alignment and ultra-violet (UV) exposure. In this step, the pattern that needs to be transferred onto the wafer is deposited in an opaque mask. The opacity part will work differently depending if one is working with a +PR or -PR. Once the mask is in contact with the wafer and has been properly aligned, the PR is exposed through the pattern with a high intensity UV light.

5. Post exposure bake and development phases. In the first step, the PR is stabilized and hardened, and also the adhesion of the PR to the wafer surface is improved. With a +PR, the development phase serves to remove the exposed PR layer.

6. Finally, the PR stripping step. The patterns at this point was transferred and then the PR must be stripped after the imaged wafer is processed.

The patterning transfer process can be done in two different ways: etching and lift-off – see Figure 3.2b. In an etching process, the material is already deposited on the substrate and the PR forms a protective layer to the etchant. It is known as a subtractive process. On the other hand,
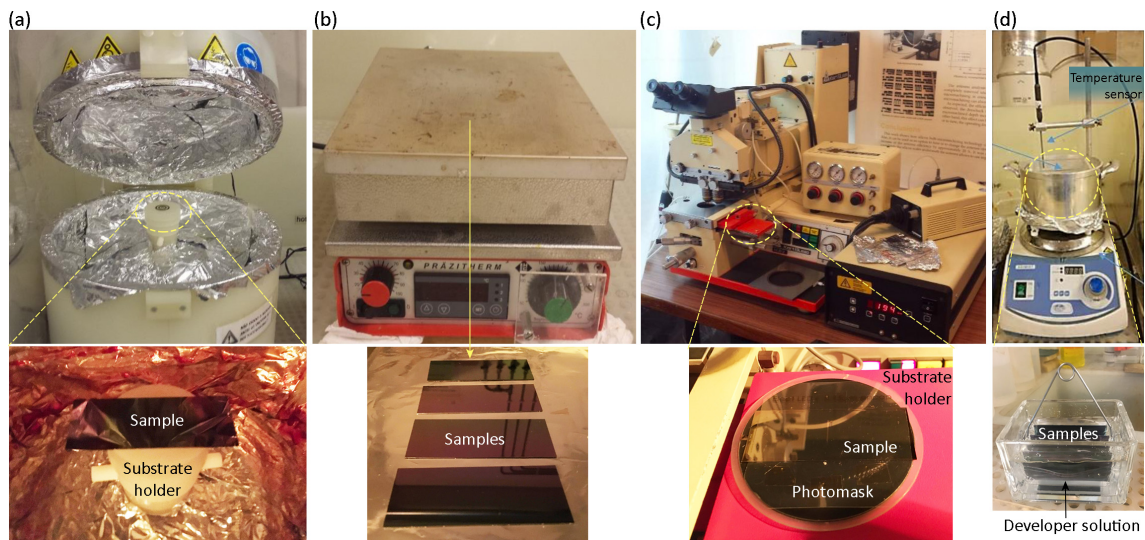
**Figure 3.3:** Laboratory equipment used in the photolithography processes of the optrode fabrication. (a) Spin-coater; (b) Hotplate (Präitherm PZ23-2, Harry Gestigkeit GmbH); (c) Mask aligner (Karl SUSS MUB3) that allows all-axis control and wavelength exposure of 365 nm or 405 nm; and (d) Hotplate and magnetic stirrer for the developing phase.

lift-off process is an additive technique. Here, the PR forms a mold, into which the desired material is deposited. The desired features are completed when the PR under unwanted areas is dissolved, and unwanted material is lifted off [5]. In this work, we use lift-off processes to pattern the recording sites, LED pads, and interconnection lines and pads.

The minimum feature size (resolution) that can be obtained with this technique has been improving with the years. It depends on the focusing of the optical source and the interaction with photoresist, i. e., exposure dose and time [6]. In this work, the minimum line width and pitch was 20 $\mu$m. Figure 3.3 shows the equipment used for all photolithographic processes during optrode manufacturing.

### 3.1.3   Physical Vapor Deposition

The fabrication of important components of the microsystem requires a number of the deposition made by physical vapor deposition (PVD) technology. PVD describes deposition methods under vacuum conditions to produce thin-films (ranging from few nanometers to thousands of nanometers) and coating layers. In contrast with CVD, physical techniques do not require chemical reactions to occur to deposit a material. A key advantage of PVD is that almost any type of inorganic material
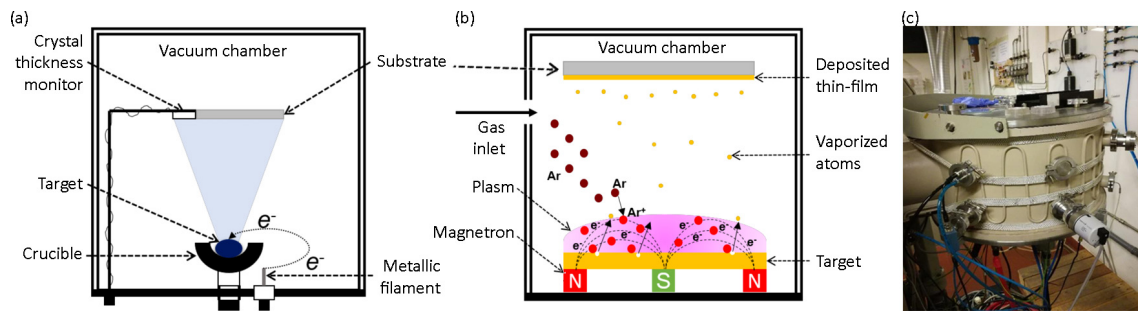
**Figure 3.4:** PVD process illustration. (a) E-beam and (b) magnetron sputtering thin-film deposition under vacuum conditions. (c) Deposition chamber used for thin-film depositions during optrode fabrication process.

can be used as well as some kinds of organic materials [7].

In this work, the optrode active sites, i.e, recordings sites, interconnection lines and pads are manufactured by the deposition of metallic thin-films (Ti/Al/Pt) over Si/SiO$_2$ wafers. Also, encapsulation phase is accomplished by deposit a coating layer of SiN over the optrode. Ti and Al thin-films are deposited by e-beam technique. Pt and SiN films are deposited by direct current (DC) and radio frequency (RF) sputtering, respectively.

### Electron-beam technique

Electron-beam (e-beam) is a form of PVD in which a target anode mounted on crucible is bombarded with an electron beam under vacuum conditions (Figure 3.4a). The e-beam is generated from a metallic filament and steered via electric and magnetic fields to strike the target surface. The energy of the e-beam is transferred to the target surface, heating it and causing its atoms to vaporize. The vaporized atoms then travel and precipitate into a solid form, coating the entire surface of the substrate. Generally, the substrates are placed at an appreciable distance away from the target to reduce the radiant heating of the substrate by the target. Average working distances between target and surface are 300 mm to 1 m [8].

E-beam technique has several advantages: (i) permits direct transfer of energy to the target during heating, and therefore becomes very efficient in depositing pure evaporated material to substrate; (ii) offers high coating uniformity and precise layer monitoring; (iii) material utilization efficiency is high relative to other methods; (iv) the process offers structural and morphological control of films; and (v) has a large range of deposition rates (it can be as low as 1 nm/min to

as high as few $\mu$/min). Due to high deposition rates, e-beam has potential for several industrial applications, e.g. electronic and optical films for semiconductor industry [9].

**Sputtering technique**

Sputtering deposition is a non-thermal process and the atoms are physically ejected from the target onto to the substrate. This effect is caused by momentum transfer from an atomic-sized energetic bombarding particle, usually a gaseous ion, accelerated from a plasma (Figure 4.5b). These particles are often from an inert gas such as argon (Ar) [8]. The basic sputtering setup includes an anode (substrate) and a cathode (target) within a vacuum system. By applying voltage between the anode and the cathode, and with the appropriate gas pressure, plasma is generated in the region close to the cathode surface. Ionization of the gas results in free electrons and their respective ion pairs, whereby an electrically neutral plasma is formed. The ions are rapidly accelerated towards the cathode (negatively charged), causing the target to be sputtered. From this sputtering results the release of atoms and secondary electrons from the target. The secondary electrons are accelerated off the cathode, colliding against atoms, forming new ions. The atoms migrate to the substrate where they are deposited and finally form a layer of a thin-film [8].

Sputtering processes can be implemented with DC or alternating current (AC) using RF. The first is frequently used when the target material is a good electrical conductor, such as metals. RF sputtering uses AC at high frequencies (13.56 MHz) and differs from DC deposition because it avoids charge accumulations on the target surface by alternating ions and electrons production according to RF cycle. Thus, RF sputtering enables deposition of insulation materials (e.g. SiN). A magnetron can also be used in a sputtering deposition. In this case, the cathode is mounted over magnets that are used to create a static magnetic field on the target surface. The secondary electrons that are emitted from the bombardment of the target ions, are maintained in the proximity of the cathode, by the action of the magnetic field. This cause the ionization of the molecules of the gas, which generates a higher-density plasma and thus higher sputtering rates. The atoms removed from the target (electrically neutral) are not affected by the generated magnetic field [8].

Sputtering is extensively used in the semiconductor industry to deposit thin films of various materials in integrated circuit processing [9]. Compared to evaporation techniques (e.g. e-beam), sputtering allows better film uniformity, especially in regions with steps or grooves. Also, another

important advantage of sputtering is that even materials with very high melting points are easily sputtered while evaporation of these materials is difficult [9].

## 3.2 Packaging

After the optrode fabrication process is completed, the active sites must be connected to external hardware. The packaging process of this microsystem implements essentially wirebonding technique. This will ensure electrical connection between the optrode device and a PCB.

### 3.2.1 Wirebonding

Wirebonding is a process that provides electrical connection between two components, normally between an integrated circuit chip and its package. The interconnection is formed by a thin metal wire, which is mechanically and electrically connected to the chip and the package using a wirebonding tool. The wire used in this technique is usually made of Au or Al [10].

There are two common wirebonding processes: ball bonding and wedge bonding. For the optrodes wirebonding process, it was employed wedge bonding technique. This bonding process uses ultrasonic energy and pressure to create the bond between the wire and the bond pad. Generally, Al wire is the most predominant wire used, since it enables the process to occur with low or even room temperature, whereas when Au wire is used, temperature go up to 150 °C. Figure 3.5 illustrates the wedge bonding process. Initially the bond wedge moves the wire towards the bond pad. After the contact with the bond pad, adequate amounts of pressure and ultrasonic forces are applied to the wire for a specific amount of time, forming the initial metallurgical weld between the wire and the bond pad (first bond). Regardless of the temperature, the wedge process deforms the
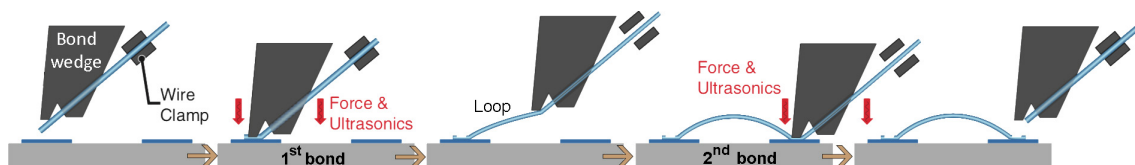


**Figure 3.5:** Wedge bonding process illustration: the wire is wedge-bonded to a metal pad, and after generating a specific loop shape of the wire, it is stitch bonded to the second bond pad (adapted from [10]).
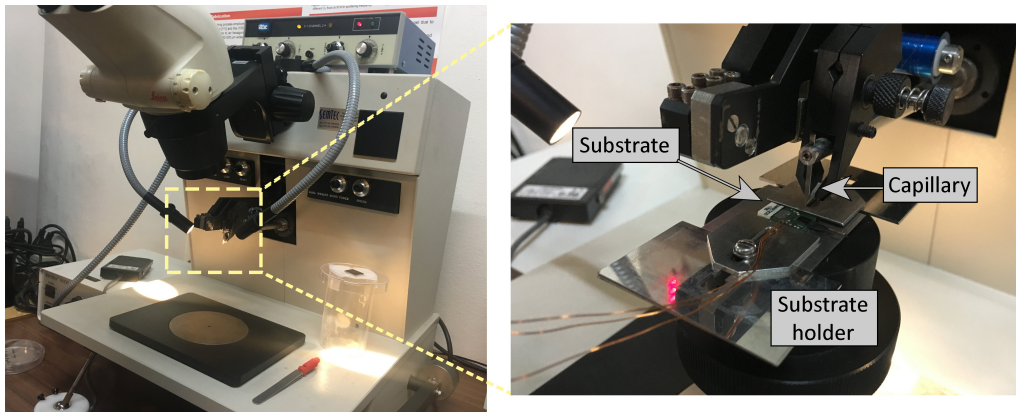
**Figure 3.6:** Wirebonding machine used for the optrode fabrication process.

wire into a flat elongated shape of a wedge. The wire is then run to the corresponding package location, forming a gradual arc or "loop" between the bond pad and the destination. Pressure and ultrasonic forces are applied to the wire to form the second bond. The wirebonding machine breaks the wire in preparation for the next wirebonding cycle by clamping the wire and raising the capillary. Unlike ball bonding, the first bond for a wedge bond does not have a ball, which is why this wire bonding process is called wedge-wedge bonding. The absence of the ball on the first bond gives wedge bonding an advantage for much finer pitch applications of 40 $\mu$m or less.

In this work, the interconnection pads patterned in the backside of the Si probe are connected to the metallic pads of a PCB using Al wires. Figure 3.6 shows the wirebonder (1204W, Mech-El Industries Inc., USA) used in this phase.

The optrode device is physically and electrically connected to a PCB, whose layout is shown in Figure 3.7a. PCB layout consists of a double metal-layer with thirteen output connections: ten for the recording sites; two for the LED; and one for ground (GND). This layout was carried out using Altium software. Figure 3.7b shows a photo of the final PCB.
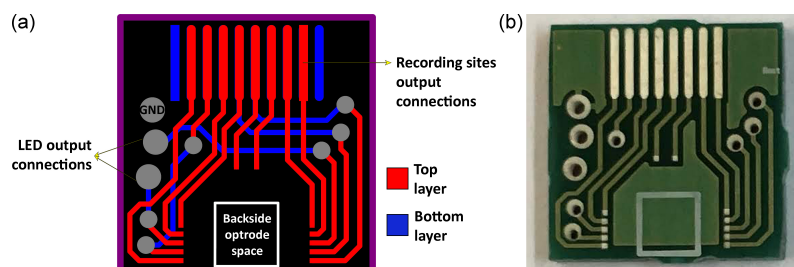


**Figure 3.7:** (a) PCB layout and (b) photo connected to the optrode microsystem.

# 3.3 In vitro Characterization Technologies

As previously discussed in section 1.4, optrode devices must meet a number of requirements to be a safe and useful tool for brain mapping and modulation. The characterization process is an essential step for any device. Although there are sophisticated simulation tools used to predict complex multiple behavior (mechanical, optical, thermal, etc.), there will be always a disparity between the performance of a device as predicted in theory and as observed in practice. The fabrication equipment and materials perform non-ideally, and thus it is important to understand how well a device performs under specific conditions. In this section, it is described the testing methods used to validate in vitro the proposed microsystem.

## 3.3.1 Mechanical tests

Probes mechanical robustness is essential to prevent that they break during insertion and withdrawal into brain tissue. Thus, implantation and extraction tests were performed in different mediums and at different speeds. Besides assessing probe integrity after this process, the force required to implant and extract the probe was also measured under different conditions. Finally, it was also performed longitudinal and axial compressive tests to quantify maximum load supported by the probes.

Figure 3.8 shows the setup arrangement for all mechanical tests. All tests were carried on a Shimadzu AG-IS dynamometer equipped with a 10 N $\pm$ 1% load cell (Shimadzu AG-IS, SLBL-10N). The load cell holds the probe and moves it towards a specific target. During implantation, the probe is lowered to the point of piercing the medium, whereas in the extraction the probe goes in the opposite direction until it stops touching the medium (Figure 3.8a). Measurements were made in two different substrates: 0.6% agar gel and calf cadaver brains. The use of 0.6% agar gel as a brain phantom was previously reported [11, 12]. Brain samples were preserved 12 hours at 5° C. Trials were carried out at room temperature. For both mediums, three different speeds were used: 50 mm.min$^{-1}$, 120 mm.min$^{-1}$ and 180 mm.min$^{-1}$. Different speeds aim to study the impact of this variables on the maximum implantation and extraction load magnitude.

Compressive strength tests assess the capacity of a material/device withstand loads. Here, probe shafts are subjected to compressive stress, buckling until they fracture. Theoretical maximum
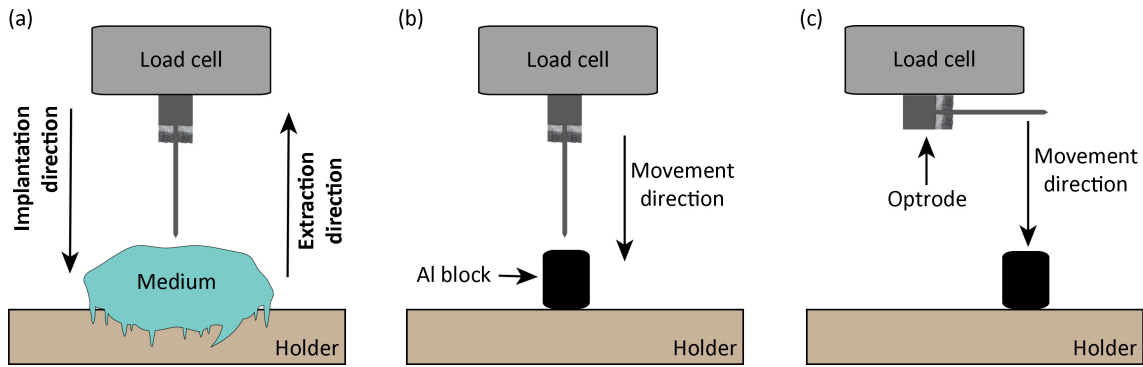
**Figure 3.8:** Illustration of the setup used for mechanical tests on the optrode. (a) Implantation and extraction tests on a certain medium. (b) Longitudinal and (c) Axial compression strength failure tests, where probe moves towards a hard block until it breaks.

load can also be obtained by the Euler equation 3.1:

$$P_{cr} = \frac{\pi^2 E A}{(kL/r)^2} \tag{3.1}$$

$P_{cr}$ is the longitudinal compression load on the sample, $E$ is the Young's modulus of shaft material, $A$ is the minimum area cross-section of a rectangular area: $t$ and $w$ is the shaft thickness and width, respectively. $k$ is the effective length factor, $L$ is the shaft length, and $r$ is the radius of gyration of a square cross-section, given by the equation 3.2. $I$ is the moment of inertia of a rectangular area.

$$r_{x=y} = \sqrt{\frac{I_{x=y}}{A}} = \sqrt{\frac{w^3 t}{12wt}} = \frac{w}{\sqrt{12}} \tag{3.2}$$

For longitudinal compression tests (Figure 3.8b), Si shafts are fixed perpendicularly to the dynamometer Al block surface, while in axial compression test (Figure 3.8c), shafts are positioned horizontally to the Al support. In both tests, the device moves towards the aluminum block, at a constant rate of 50 mm.min$^{-1}$, until it breaks.

## 3.3.2   Electrochemical tests

The amplitude of action potentials can be quite large, more than 500 $\mu$V, but is more typically on the order of 100 $\mu$V [13]. Low-amplitude signals are quite sensitive to noise. Although the majority of the noise signal encountered in single-unit recording arises from the multitude of undifferentiated
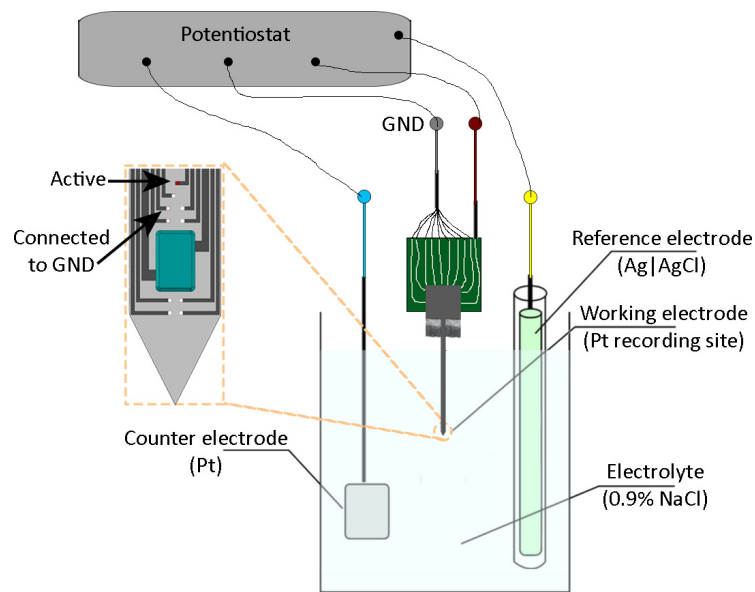
**Figure 3.9:** EIS three-electrode configuration measurement setup. In this configuration a fixed voltage is applied to the working electrode and the output current is read, and converted to a voltage signal by the transimpedance amplifier.

background action potentials (neural noise), the electrode impedance also affects the recording signals quality [14]. Therefore, higher impedance electrodes are expected to have lower signal-to-noise ratios (SNR) [13].

Electrochemical impedance spectroscopy (EIS) involves measuring the electrical impedance and phase angle obtained with sinusoidal voltage or current excitation of the electrode. EIS spectra are probably the most valuable in assessing the recording capabilities of electrodes and, because the voltage excursions at the electrode are small, may also be a useful and benign method for the in vivo assessment of an electrode [15]. Recording electrodes are typically characterized by their impedance at 1 kHz (firing rate of neurons), which is quite variable, ranging in vivo from approximately 50 k$\Omega$ to 1 M$\Omega$ [13]. The phase angle describes how capacitive or resistive the interface is. Low capacitance is desirable for neural recording since it will provide an overall lower electrode impedance [15].

EIS was used to characterize the impedance of the Pt recording sites of fabricated optrodes. The impedance measurements were performed in a potentiostat using a standard three-electrode configuration, as shown in Figure 3.9, immersed in a 0.9% saline solution at room temperature.

The electrode-electrolyte interface can be modeled by an electrical equivalent circuit, as shown in Figure 3.10. Signals at the surface of the electrical active site ($V_{sig}$) generate currents ($I$) that
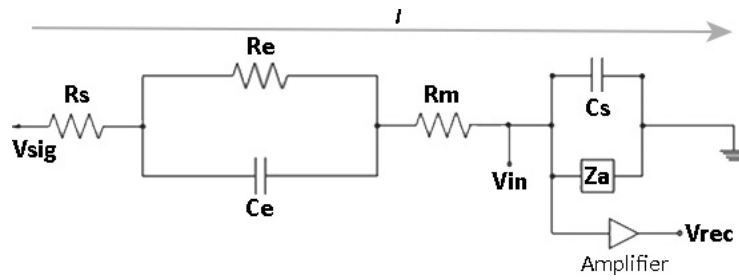
**Figure 3.10:** Equivalent circuit of an electrode-electrolyte interface (adapted from [16]).

flow to ground through the electrical recording site within the probe, and effective amplifier circuit, creating the potential ($V_{in}$) at the input of the amplifier before being recorded ($V_{rec}$) [16]. Equivalent circuit includes: $R_s$, electrolyte resistance; $R_e$, leakage resistance, which models the flow of the charge carriers crossing the electric double layer; $C_e$, electrode-electrolyte interface capacitance; $R_m$, electrode resistance; $C_s$, shunt capacitance to ground; $Z_a$, input impedance of the amplifier.

### Lifetime Testing

Most implantable probes are used (and intended) for acute (few hours) in vivo applications, as they perform inconsistently in chronic applications [17]. This poses a significant barrier to adopt this technology into clinical practice. The challenge to chronically record neural signals is the lifespan of the interface in use. The use of in vivo methods to assess the reliability of the interface is not only expensive but highly time-consuming. As an alternative, high temperatures are used to accelerate failure mechanisms [18]. The Eyring equation describes the temperature effect and is written in terms of a reaction rate $K$ [19] – equation 3.3.

$$K = k\frac{k_B T}{h}e^{\frac{-\Delta A\ddagger}{RT}} \tag{3.3}$$

where k is the transmission coefficient (assumed as 1, k=1), $k_B$ is the Boltzmann's constant, $h$ is the Planck's constant, $R$ is the ideal gas constant, $T$ is the absolute temperature in kelvin and $\Delta A\ddagger$ is the activation energy. To calculate the activation energy, the mean lifetime equation is related to the reaction rate [19] – equation 3.4.

$$Lifetime = \frac{1}{K} \tag{3.4}$$

Lifetime is estimated by the mean time to failure (MTTF) on a per-interconnect basis at elevated temperature. Using this correlation, the activation energy is given by equation 3.5:

$$\Delta A\ddagger \ = \ -RTln(\frac{h}{k_B T \cdot MTTF(T)}) \tag{3.5}$$

MTTF is estimated experimentally by measuring magnitude impedance of the probe recording sites over time at a constant elevated temperature (80° C), until failure occurs. The accelerated lifetime tests employ the same setup shown in Figure 3.9, using 1x phosphate buffer solution (PBS) as electrolyte with pH of 7.5. PBS is a saline buffer solution similar in composition to cerebrospinal fluid [20].

### 3.3.3   Optical tests

Optical measurements served to ensure enough optical power is delivered to the neural tissue. Besides light intensity, it is important to ensure the light source presented the adequate wavelength, since the engineered neurons expressing opsins are only activated when light is delivered at target wavelength with a minimum of optical power.

Two major tests were performed with optrode light source (LED): peak wavelength ($\lambda_p$) measurement and optical power test. An illustration of the setups used for these tests is shown in Figure 3.11. All tests were carried out in a controlled light ambient, in order to keep at a minimum the influence of the light outside the LED.

The first test serves to specify the color of the LED used, i.e., the maximum point of the spectral curve. A spectral curve shows the intensity of light recorded for a range of wavelengths. In addition to the $\lambda_p$, with the spectral curves, it is also possible to obtain the LED main wavelength ($\lambda_s$) and dominant wavelength ($\lambda_d$). $\lambda_s$ is the main point of the spectral curve, and it is identical with $\lambda_p$ in the case of a symmetrical spectral curve. $\lambda_d$ is a measure of the hue perceived by the human eye. The peak wavelength test uses a monochromator that gives a precise determination of the emission spectrum. The specified amount of light emitted by the LED is focused through an optical system onto the inlet window of the monochromator. The part of the light (which is not absorbed) arrives at a calibrated detector, whereby external and reflected light must be carefully screened. The peak wavelength is obtained by tuning the monochromator until the meter indicates a maximum
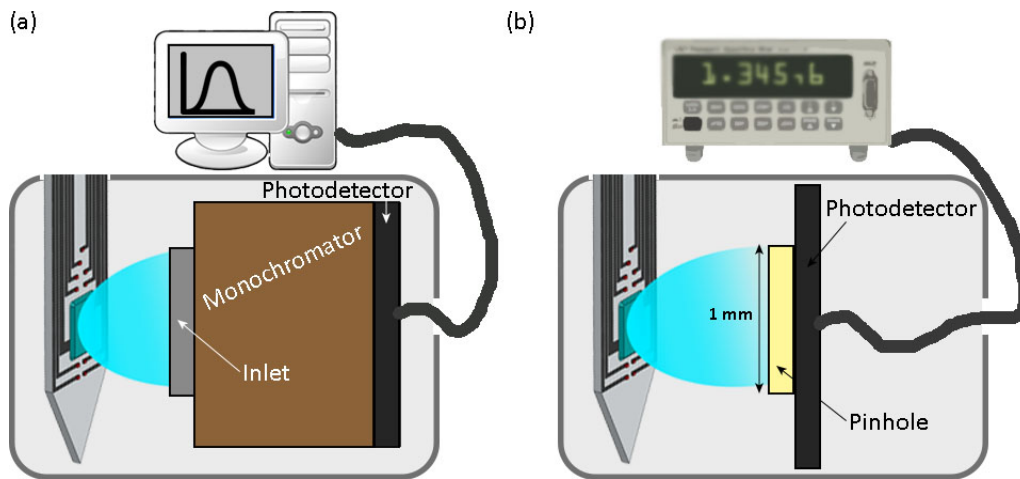
**Figure 3.11:** Illustration of the setup used for optical tests on the optrode. (a) Peak wavelength and (b) optical power measurements.

value [21]. The current values are obtained by a photodetector coupled to the monochomator outlet.

The optical power is decisive for characterization of any light source, as it corresponds most closely to the final application of the component [21]. It is measured in the direction of the mechanical axis of the LED with a small measuring angle. In this configuration, the LED is positioned in front of the suitable photodetec- tor, which is connected to a power meter. Coupled to the photodetector is a 1 mm-diameter pinhole that aims to limit the active photodetector area of detection, and thus obtaining LED optical current in A.mm$^{-2}$. Optical power ($P$) value (in mW.mm$^{-2}$) is obtained by the equation 3.6, where $I$ is the current produced by the photodiode (in A.mm$^{-2}$) and $\Re_\lambda$ (in A/W) is the photodiode responsivity at a specific wavelength.

$$ P_\lambda \; = \; \frac{I}{\Re_\lambda} \tag{3.6} $$

# References

[1] M. Arif, M. Rahman, W. San, "A state-of-the-art review of ductile cutting of silicon wafers for semiconductor and microelectronics industries", Int J Adv Manuf Technol, **63**, doi: 10.1007/s00170-012-3937-2, 481-504, 2012.

[2] H. Zhou, S. Qiu, Y. Huo, N. Zhang, "High-speed dicing of silicon wafers conducted using ultrathin

blades", Int J Adv Manuf Technol, **66**, doi: 10.1007/s00170-012-4379-6, 947–953, 2013.

[3] Disco Technologies. Electroformed bond blades: Z09 Series. `https://www.disco.co.jp/eg/products/catalog/pdf/z09.pdf` [Accessed on July 2018]

[4] Wafer World. Photolithography: Its Importance in Semiconductor Manufacturing. `https://www.waferworld.com/photolithography-its-importance-in-semiconductor-manufacturing/` [Accessed on July 2018]

[5] MEMSnet. Pattern Transfer. `https://www.memsnet.org/mems/processes/lithography.html` [Accessed on July 2018]

[6] L. Yiyong, and Y. Guoguang, "Linewidth control by overexposure in laser lithography," Optica Applicata, **XXXVIII**(2), doi: 10.1.1.557.4406, 399-404, 2008.

[7] Azo Materials. Physical Vapour Deposition (PVD) - An Introduction. `https://www.azom.com/article.aspx?ArticleID=1558` [Accessed on July 2018]

[8] D. M. Mattox. Handbook of Physical Vapor Deposition (PVD) Processing. Second ed. Elsevier Inc. 2010.

[9] Abrisa technologies. Physical Vapor Deposition - Sputtering vs. Electron Beam Evaporation. `http://abrisatechnologies.com/2012/09/physical-vapor-deposition-sputtering-vs-electron-beam-evaporation/` [Accessed on July 2018]

[10] A. C. Fischer, J. G. Korvink, N. Roxhed, G. Stemme, U. Wallrabe, and F. Niklaus, "Unconventional applications of wire bonding create opportunities for microsystem integration," J. Micromech. Microeng., **23**, doi: 10.1088/0960-1317/23/8/08300, 083001, 2013.

[11] R. Pomfret, G. Miranpuri, and K. Sillay, "The Substitute Brain and the Potential of the Gel Model," Annals of Neurosciences, **20**(3), doi: 10.5214/ans.0972.7531.200309, 118-122, 2013.

[12] R. Das, D. Gandhi, S. Krishnan, L. Saggere, and P. J. Rousche, "A Benchtop System to Assess Cortical Neural Interface Micromechanics," IEEE Transactions on Biomedical Engineering, **4**(6), doi: 10.1109/TBME.2007.897139, 1089-1096, 2007.

[13] S. F. Cogan, "Neural Stimulation and Recording Electrodes," Annu. Rev. Biomed. Eng., **10**, doi: 10.1146/annurev.bioeng.10.061807.160518, 275-309, 2008.

[14] T. Chung, J. Q. Wang, J. Wang, B. Cao, Y. Li, and S. W. Pang, "Electrode modifications to lower

electrode impedance and improve neural signal recording sensitivity," J Neural Eng, **12**(5), 056018, doi: 10.1088/1741-2560/12/5/056018, 2015.

[15] B. Chang, and S. Park, "Electrochemical Impedance Spectroscopy," Annu. Rev. Anal. Chem., **3**, doi: 10.1146/annurev.anchem.012809.102211, 207-229, 2010.

[16] M. Jorfi, J. L. Skousen, C. Weder, and J. R. Capadona, "Progress towards biocompatible intracortical microelectrodes for neural interfacing applications," J. Neural Eng., , doi: 10.1088/1741-2560/12/1/011001, 011001, 2015.

[17] V. S. Polikov, P. A. Tresco, and W. M. Reichert, "Response of brain tissue to chronically implanted neural electrodes," J. Neurosci. Methods, **148**(1), doi: 10.1016/j.jneumeth.2005.08.015, 1-18, 2005.

[18] L. A. Escobar, and W. Q. Meeker, "A Review of Accelerated Test Models," Statistical Science, **21**(4), doi: 10.1214/088342306000000321, 552-577, 2007.

[19] P. W. Atkins, and J. De Paula, Elements of physical chemistry. Fifth ed. Oxford University Press, 2009.

[20] Medicago Inc. Smart Buffers: Phosphate Buffered Saline (PBS), pH 7.4 and 7.2. `http://www.medicago.se/phosphate-buffered-saline-pbs-ph-74-and-72` [Accessed on August 2018]

[21] Vishay Telefunken. Measuring Technique. `https://www.vishay.com/docs/led_measure.pdf` [Accessed on August 2018]

# Chapter 4

# Experimental Results

This chapter presents the fabrication and in vitro characterization experimental results of the optrode microsystem. All manufacturing steps are detailed and discussed here, resulting in an optrode 8 mm long and 600 $\mu$m wide with a sharp tip. Active components of this device include 10 recording sites and one LED chip for electrical recording and optical stimulation, respectively. Electrochemical, optical and mechanical testing results of the device is also addressed in this chapter.

## 4.1    Manufacturing results

Figure 4.1 summarizes the manufacturing process of the proposed single-shaft device. As discussed in the previous chapter, the optrode fabrication process combines several microtechnologies, such as dicing blade, photolithography and PVD processes. All photos and measurements were performed with a Leica M80$^{TM}$ stereo microscope and Leica LAS$^{TM}$ software.

Initially, Si wafers are diced into 75 $\times$ 30 mm$^2$ wafers using a dicing machine (DAD-2H/6T, Disco), as illustrated in Figure 4.2. This individualization aims to facilitate fabrication steps further ahead. The chosen Si doping and crystal orientation ensures the maximum shaft robustness after the dicing step that defines shafts outline. As illustrated in Figure 4.1a, Si samples are coated with a thin layer (1 $\mu$m) of SiO$_2$ that ensures electrical insulation between patterned components. Next, Si samples are cleaned with acetone on a 20 min ultrasonic bath, then rinsed with deionized (DI) water and heated at 110 $^\circ$C during 20 min for dehydration. The cleaning step promotes a better
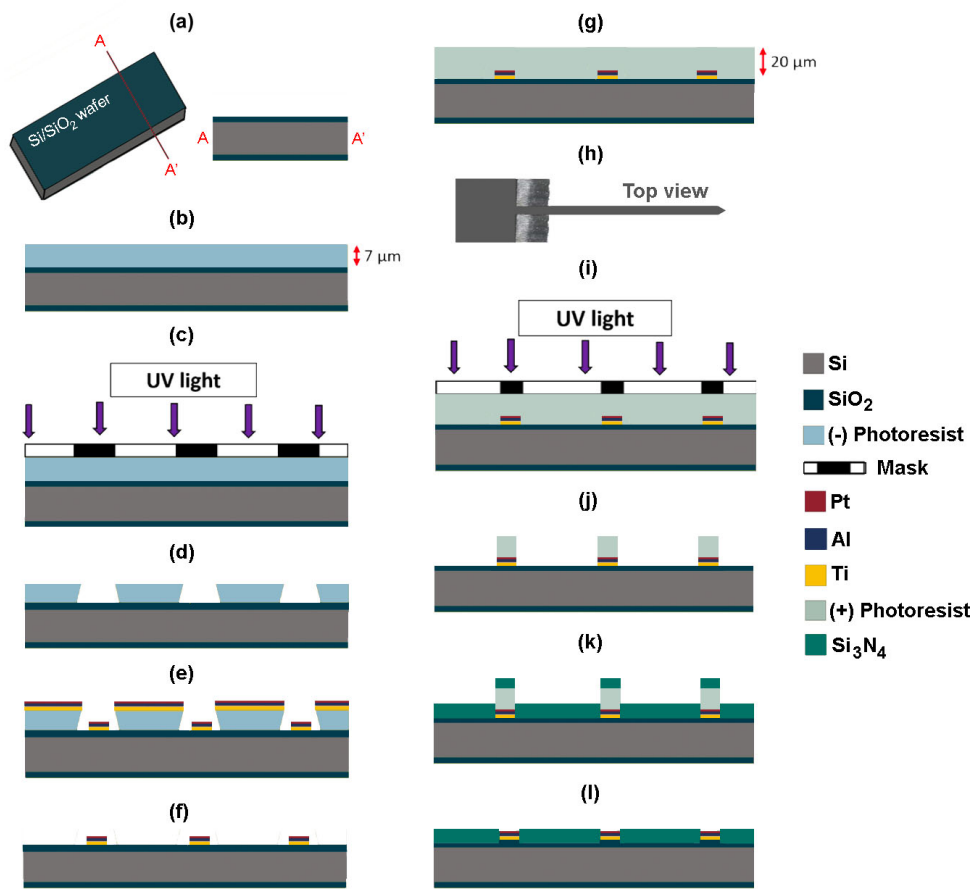
**Figure 4.1:** Cross-section view of the optrode fabrication process flow (not to scale).

adhesion of the substrate surface in the next fabrication steps.

After cleaning, it follows a lithographic step (Figure 4.1b to f) to pattern the recording sites, LED pads and interconnection lines. This phase starts by spin-coating a 7 $\mu$m thick layer of -PR (AZ nLOF 2070, MicroChemicals GmbH) that is an image reversal resist (Figure 4.1b). Then, the samples are exposed to UV light (Figure 4.1c), using the lithographic mask shown in Figure 4.3a. Next, the samples are immersed in developer (AZ 726 MIF, MicroChemicals GmbH) to dissolve the unexposed PR (Figure 4.1d). Figure 4.4 shows SEM images (NanoSEM, FEI Nova 200) of the patterning and the developing phases using the reversal PR.

Next, it is performed a metalization step of Ti/Al/Pt (15 nm/200 nm/60 nm) over the samples (Figure 4.1e). Thin-film deposition parameters are shown in Table 4.1 and the setup in Figure 4.5. Ti layer serves as an adhesion layer between $SiO_2$ surface and the above metallic thin-film. Al layer provides high currents to the LED, and therefore, increases light power delivered to target
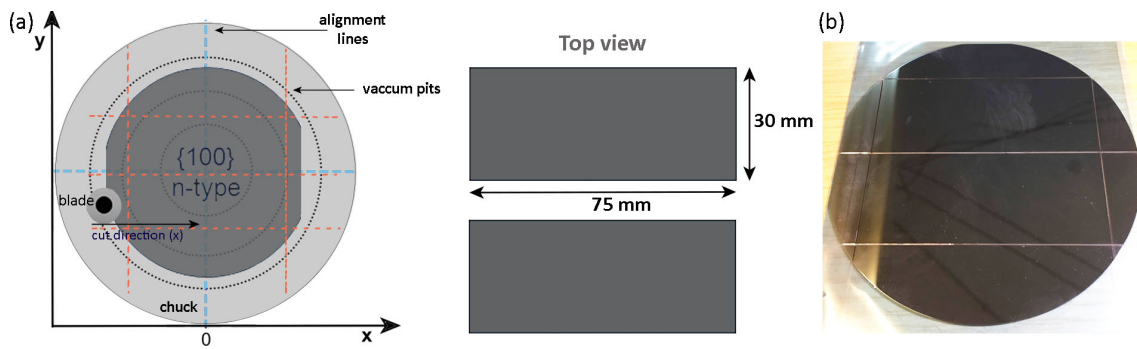
**Figure 4.2:** (a) Illustration of the individualization dicing step of Si/SiO$_2$ wafers into $75 \times 30$ mm$^2$ samples. (b) Dicing result.
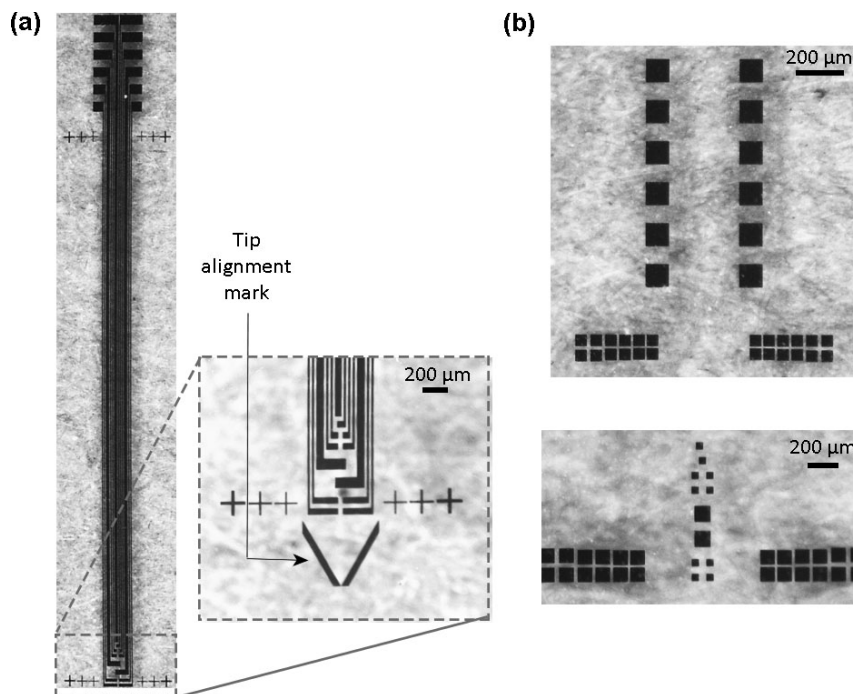


**Figure 4.3:** Lithographic masks used during fabrication process of the optrode. (a) Interconnection lines, recording sites, and pads for the LED; (b) Connection pads to external electronics (top) and exposure of the recording sites areas and LED contact pads (bottom).

cells. Finally, Pt thin-film, which is only exposed to neural tissue in the recording sites areas ($50 \times 50$ $\mu$m$^2$), aims to transduce ionic current into electrical currents and acquire the biosignals. The samples are then immersed in a stripper solution (TechniStrip NI555, MicroChemicals GmbH), removing PR from the wafer. At this phase of the fabrication process, the recording sites, LED pads, interconnection lines and external connection pads of the device are patterned (Figure 4.1f).
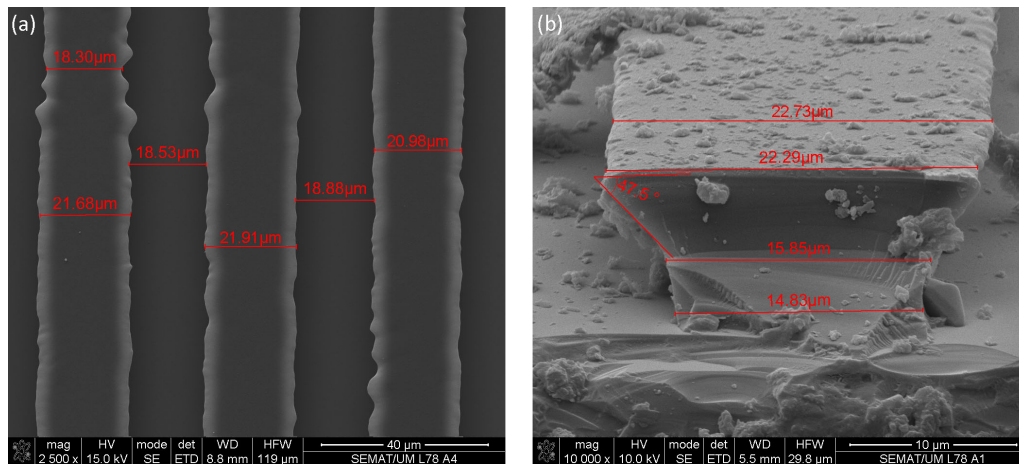
**Figure 4.4:** SEM images of the first lithographic step using AZ nLOF 2070 -PR. (a) Top view of the interconnection lines for the recording sites. Lines are $\approx$ 20 $\mu$m wide and spaced by $\approx$ 20 $\mu$m. (b) Cross-section of post-developing PR, showing its undercut profile.

The following step is another photolithographic process that consists on the deposition of a 20 $\mu$m thick +PR layer (AZ 4562, MicroChemicals GmbH) by spin-coating (Figure 4.1g). This phase has a twofold purpose: (i) to protect the samples against Si dust during the next dicing phase, and (ii) pattern the encapsulation layer of the optrode.

This cutting phase is done to get the desired probe profile (Figure 4.1h). The cuts are performed using the same dicing machine. Figure 4.6 shows the schematic of the dicing process

**Table 4.1:** Parameters of the thin-films deposition to manufacture the optrode microsystem.

| Parameters | Unit | Ti | Al | Pt | SiN |
|---|---|---|---|---|---|
| Technology | | E-beam | E-beam | DC sputtering | RF sputtering |
| Target | | Ti | Al | Pt | Si |
| Thickness | nm | 15 | 200 | 60 | 400 |
| Pressure | mbar | $4.3\times10^{-6}$ | $5.3\times10^{-6}$ | $6\times10^{-3}$ | $6\times10^{-3}$ |
| Gas injection | sccm | – | – | 40 (Ar) | 7 (Ar) and 13 (N$_2$) |
| Power | W | 350 | 700 | 100 | 150 |
| Rate | Å/s | 0.8 | 23 | 3.4 | 0.3 |
| Temperature | °C | 98 | 68 | 80 | 60 |
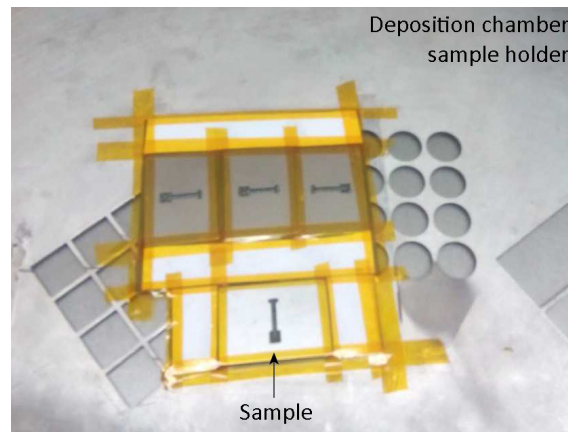
**Figure 4.5:** Setup used for the metalization step of Ti/Al/Pt (15 nm/200 nm/60 nm) thin-films.

to define the shaft profile: $\approx$ 8 mm long, $\approx$ 600 $\mu$m wide and a sharp tip. While shaft width is set exclusively by Y-axis step (600 $\mu$m), its length is accomplished by altering: (1) X-axis range of the blade, and (2) sample alignment on chuck table. During cuts in X-axis, the blade is expected to cover the distance correspondent to X-axis step value. As the equipment restricts X-axis value to a minimum of 24 mm, using a range value inferior to its limits will inevitably result in a 24 mm long cut – Figure 4.6. Thus, depending on the desired shaft length, substrate might be aligned differently in the chuck surface. Here, the wafer is aligned by midline of the chuck and define X-step to 24 mm, which results on 12 mm long shafts (Figure 4.6, Top view). Alignments left from midline allow increasing shaft length, while right alignments would decrease it. It is important to note that long cuts in X-axis direction result in lengths 4 mm shorter than intended, i.e., 12 mm cuts in substrate produce shafts as long as 8 mm. This phenomenon is shown in cross-section view of Figure 4.6. The explanation for this occurrence is due to round geometry of the blade, which by the end of the
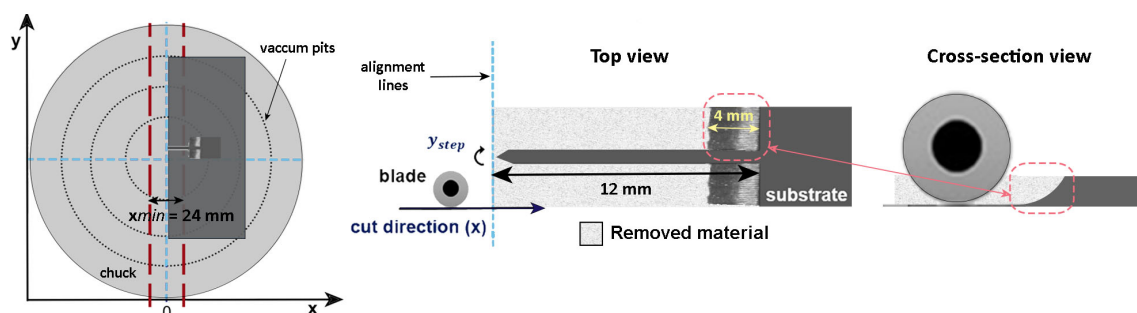


**Figure 4.6:** Schematic of the dicing process in the chuck (left), and top (middle) and cross-section (right) view detailing the cutting plan to produce the shafts profile.

**Table 4.2:** Experimental cutting parameters for single-shaft devices 8 mm long. Square brackets represent sequential Y-axis steps repeated during cutting program.

| Cut Parameter | Unit | Value |
|---|---|---|
| Blade thickness | $\mu$m | 80 |
| Cut Thickness | $\mu$m | 150 |
| Cut speed | mm.s$^{-1}$ | 0.3 |
| Z-axis step | mm | 0 (chuck surface) |
| X-axis step | mm | 24 |
| Y-axis step (shaft width) | $\mu$m | ([7 $\times$ 150], 600, [8 $\times$ 150]) |
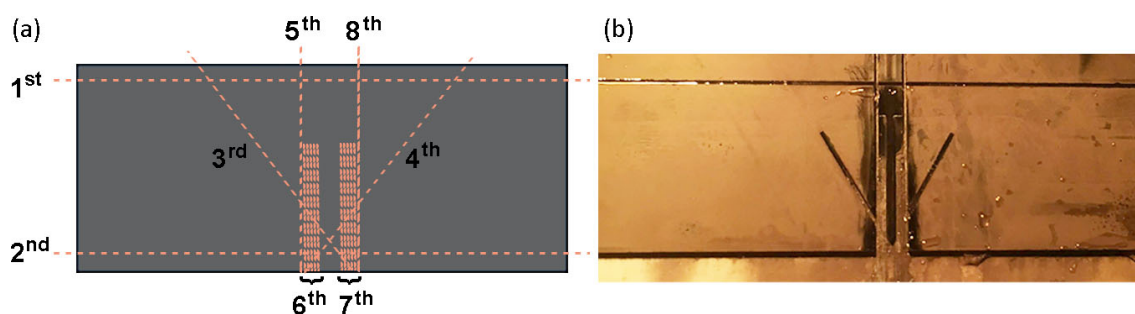


**Figure 4.7:** Dicing cuts sequence to produce shaft profile. (a) Schematic drawing. (b) Photo of the dicing result.

cut cannot completely remove the diced substrate.

The cutting program has most of its parameters with fixed values, while Y-axis steps include several steps – see Table 4.2. Y-axis blade movements consist on several different stages, as illustrated in the schematic of Figure 4.7a. Four cuts ($1^{st}$, $2^{nd}$, $5^{th}$ and $8^{th}$) serve to detach most Si parts from the samples. Sharp tip is accomplished with the $3^{rd}$ and $4^{th}$ cuts by rotating the chuck surface and align the sample by the tip alignment mark (see Figure 4.3a) previously patterned to facilitate this specific dicing step. Finally, the shaft width is defined by a set of cuts: initially, seven 150 $\mu$m-wide cuts remove excess of Si, followed by a 600 $\mu$m-wide step that determines shaft width. Then, eight more 150 $\mu$m wide-cuts remove excess of Si on the other side of the shaft. In Figure 4.7b is presented the result of the cuts sequence for the dicing step that outline optrode shafts.

After the last dicing step, the samples are exposed to UV light (Figure 4.1i), using the mask shown in Figure 4.3b. It follows a cleaning step with DI water, and the PR is removed with developer
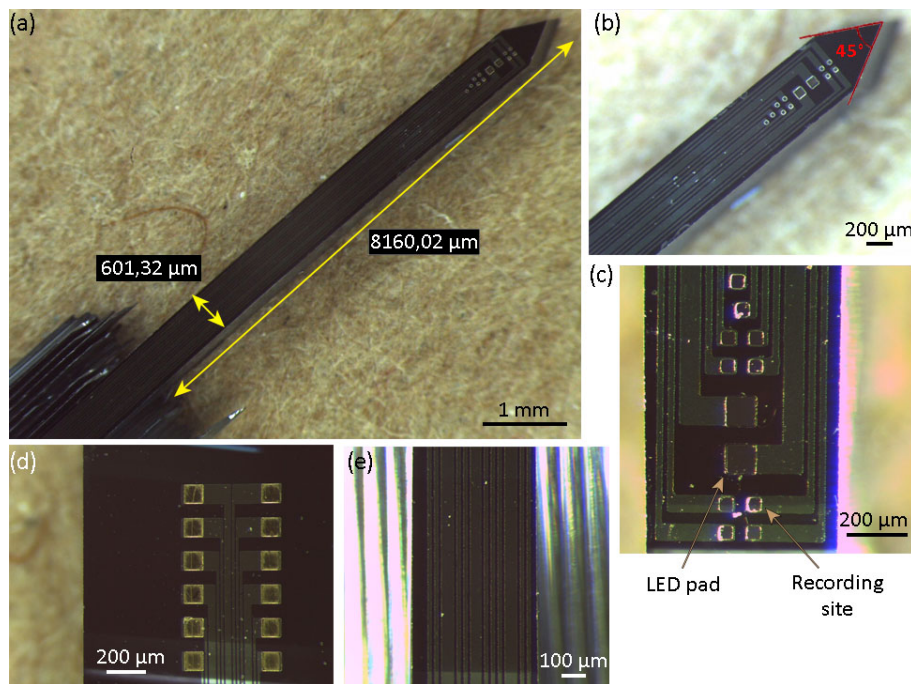
**Figure 4.8:** Fabrication result of the optrode without LED. (a) Overview photo of the encapsulated Si shaft with patterned (b) $50 \times 50\ \mu m^2$ recording sites and LED pads ($100 \times 100\ \mu m^2$) with a sharp tip ($45\,^\circ$ opening angle). (c) Zoomed image with the recording sites and LED pads. (d) External connection pads. (e) Interconnection lines.

(AZ 351B, MicroChemicals GmbH), exposing only the desired passivation area (Figure 4.1j). A deposition of 400 nm thick layer of SiN as the insulation material was performed by RF sputtering (Figure 4.1k). Deposition parameters for SiN layer are shown in Table 4.1. Then, it followed the removal of the PR layer with acetone, exposing the recording sites, LED pads and pads for external connection (Figure 4.1l). Figure 4.8 shows the result of the fabrication process without LED coupling. At this point, recording sites, LED pads, interconnection lines, external connection pads and device encapsulation are completed.

The final phase to produce the optrode consists on coupling the commercial blue-light LED chip (ELC-470-37, Roithner LaserTechnik GmbH) into the optrode shaft. This process is accomplished by manual transferring the chip into the patterned pads using sharp tweezers. The chip pads are welded at 230 °C with solder paste (EM907, Kester) dropped on the LED contact pads. LED is coated with a thin layer of a biocompatible transparent glue (PERMABOND 102), in order to protect it against wet conditions. Figure 4.9 shows the LED coupling process and result into the optrode shaft.
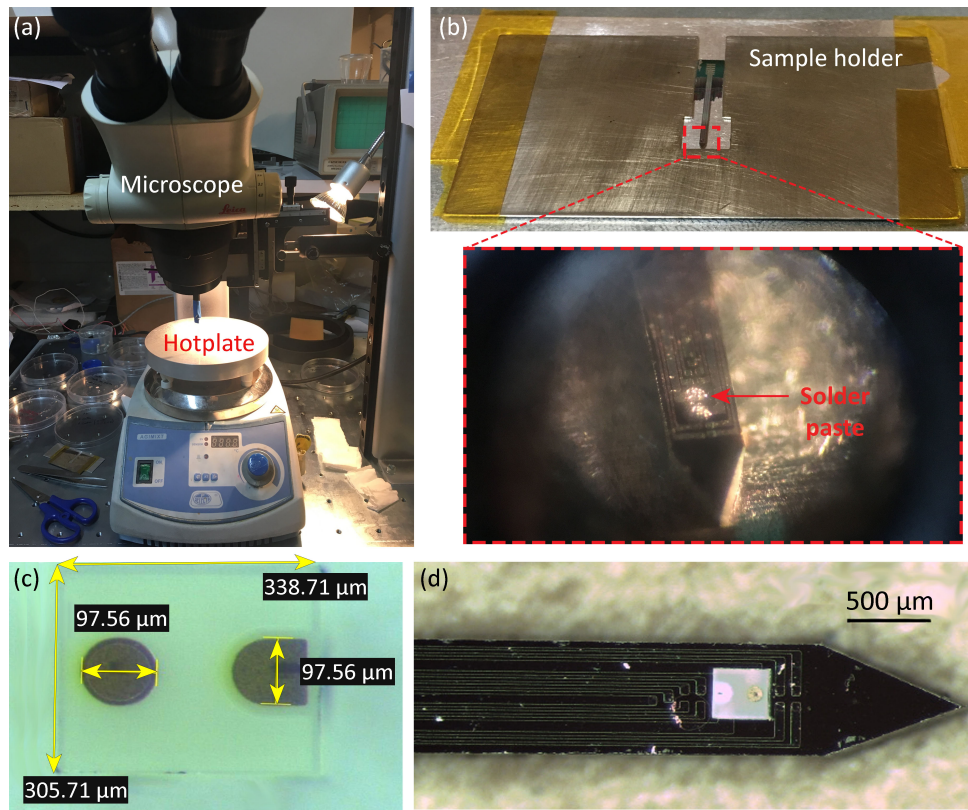
**Figure 4.9:** LED coupling into the optrode shaft. (a) Setup includes a microscope used for guidance as the LED chip is manually placed into LED contact pads. The hotplate is used to heat the optrode shaft and to weld the solder paste. (b) Optrode shaft holder that avoids probe movements during the process. (c) Dimension measurements of a LED chip encapsulation and pads; (d) LED chip coupling result.
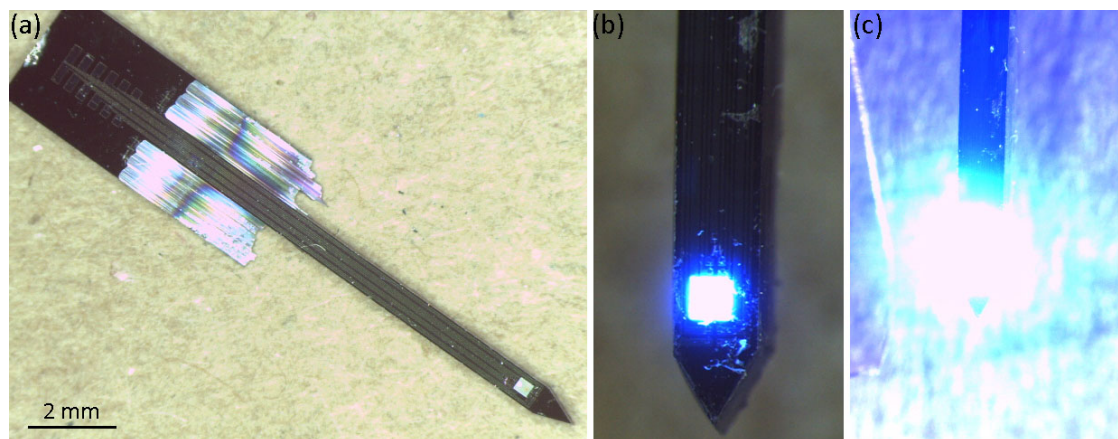


**Figure 4.10:** (a) Final optrode with 10 patterned recording sites and one commercial LED chip coupled to its shaft. LED is ON with a driving current of (b) 0.3 mA and (c) 20 mA. Higher driving current generates higher optical power and brightness.
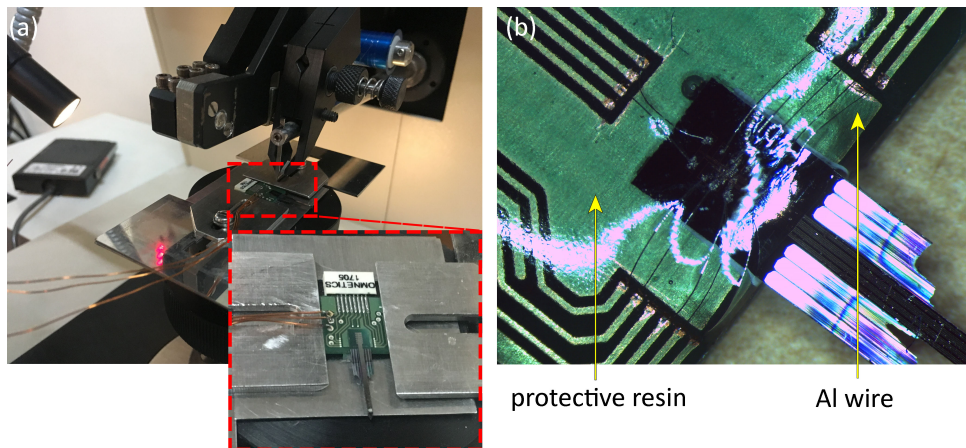
**Figure 4.11:** Optrode packaging results. (a) Setup and (b) results from Al wire-bonding of the optrode to the designed PCB.

The final optrode is presented in Figure 4.10 with 10 recording sites and one LED chip in an 8 mm long and 600 $\mu$m wide shaft, with a thick layer of SiN as insulation material. After manufacturing, the optrode is fixed to a PCB using cyanoacrylate, and its contact pads are packaged by Al wire-bonding. Figure 4.11 shows the setup and results for wire-bonding the probe to the PCB. Al wires are protected with glue resin dropped over the area. The PCB provides connection for external hardware for the LED chip and it is also coupled to an 18-pin connector (A79014-001, Omnetics) to ensure external connectivity for recording sites.

## 4.2  Fabrication discussion

The fabrication methodology based on lithography, thin-film depositions and blade dicing successfully accomplished an optrode design with the proposed features: 10 recording sites for electrical recording of neural activity, and integration of one commercial LED chip for optical stimulation of the surrounding tissue.

Microfabrication results are shown in Figure 4.8 and Figure 4.10. Geometrical features of Si optrodes resulted in $\approx$ 8 mm long, $\approx$ 600 $\mu$m wide and 525 $\mu$m thick shafts. Maximize the length of penetrating interfaces is important so the device is capable of reaching deeper neural structures than current designs [1]. 8 mm long probes can reach almost any deep region of a mouse brain [2]. However, for rodents' applications, the probe cross-section must still be optimized to reduce tissue

damage. Here it was demonstrated a single LED-based probe concept, whose dimensions are mainly limited by the dimensions of the commercial LED chip.

By using blade cutting technology to produce the single-shaft probes some level of chipping might occur at the edge of Si shafts. As a brittle material, microcracks and chipping might be created within Si wafers during mechanical processing [3]. These phenomena influence final device quality and can be reduce by optimizing cutting parameters such as: feed speed, spindle speed, cutting depth, saw street pattern and blade characteristics (diamond grit size, exposure, and thickness) [4]. The manufacturing process presented here kept to the minimum the feed and spindle speed: 0.3 mm.s$^{-1}$ and 3.000 rpm, respectively. The cutting depth is imposed by the thickness of the wafer, as final samples need to be detached from it. The choice of blade was optimized for dicing Si wafers. Nevertheless, blades wear can enhance edge chipping and explain the residual chipping sometimes observed in the final devices.

Shafts geometrical profile results in 4 mm excess of Si in the opposite site of its tip (see cross-section view of Figure 4.6). This excess could be easily removed by adding an etching step in the fabrication process. Nevertheless, due to high length of the shafts and depending on the requirement depth of application to implant the probe, this etching step may not be necessary.

Another important geometrical characteristic of the probe is its tip shape. Here, Si probe shafts present sharpened tips (opening angle 45°) – see Figure 4.8b. Sharp tips on these devices have been reported to result in lower implantation forces, and thus lowering tissue damage [5–7].

Currently, high-density probes include more than 1000 channels [8–10], which advantageously span wider tissue areas and allow unprecedented opportunities for extracellular electrophysiology studies. On the other hand, they suffer higher signal attenuations by noise and crosstalk wiring. Conversely to these high-density designs, the proposed approach includes also optical stimulation functionality, and not only recording capability as those reports. In this sense, Kim et al. [11] demonstrated a successful multi-functional optrode that includes only a single 400 $\mu$m$^2$ Pt recording site.

As previously discussed, $\mu$-LEDs are either (1) monolithical manufactured onto the device structure by deposition of GaN layers on a substrate [1, 12], or (2) integrated in the probe by LED transfer techniques [13–16]. Here, it was used the latter approach due to employment of a commercial LED chip. While the first approach has the disadvantage of offering limited substrate

choices, manual assembly of LED to substrate represents a harder task and might have yield challenges. On the other hand, the use of different wavelength LED chip for simultaneous activation and inhibition of engineered tissue is possible with commercial chip coupling approach. Further developments to our probe could include monolithically manufacture LEDs onto the probe, as demonstrated by other studies [1, 17], ultimately leading to probe cross-section reduction. An interesting approach to address high-footprint commercial LED chips is reported by Ayub et al. [18]. In that study, LED chips are mounted on a thin polyimide-based substrate, stiffened using a micromachined ladder-like Si structure. This approach avoids thicker probes by transfer LED chip to the surface of a stiff and thick substrate. Although minimizing probes cross-section is a preferable feature, with our approach wider probes are necessary to accommodate wide LED chips and recording sites.

Passivation layer on RTD is a required step with a twofold goal: (1) electrical insulation, and (2) avoid electrical stimulation of neurons in its vicinity. Indeed, current as low as 10 $\mu$A have been reported to promote microstimulation of neurons as far as 4 mm away [19].

## 4.3   Mechanical results

The fabricated devices were mechanically tested to prove their robustness. It was measured the critical load shaft withstand into axial and longitudinal directions before breaking. Also, the force needed during implantation and withdrawal in 0.6% agar gel and calf cadaver brain mediums at different speeds was obtained.

Figure 4.12 shows the setup arrangement for the compressive strength failure tests (n = 3) and the results using 8 mm long shafts. For longitudinal compression tests, shafts are fixed perpendicularly to the Al block surface (Figure 4.12a), while in axial compression test (Figure 4.12b), shafts are parallel to it. In the first case, the shaft moves towards the Al block, and in the second, probe support is lower towards the probe, at a constant rate of 50 mm.min$^{-1}$, until it breaks. Results demonstrate that shafts withstand high longitudinal and axial loads before they fracture.

Single-shaft 8 mm long devices break after undergoing longitudinal and axial loads of an average of 35.48 $\pm$0.93 N and 0.54 $\pm$0.06 N, respectively – Figure 4.12c and d. Longitudinal theoretical critical force was calculated using Equation 3.1. Si Young's modulus ($E$) is 166 GPa,
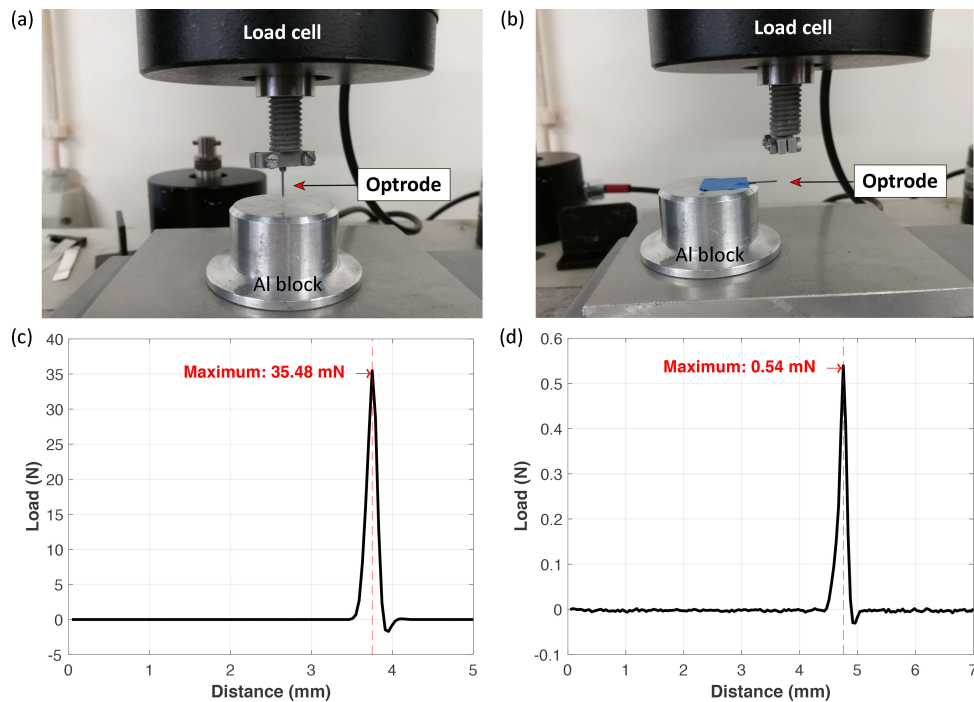
**Figure 4.12:** Experimental setup used for the compressive strength failure tests on the optrode: (a) Longitudinal and (b) axial tests. Plot with (c) longitudinal and (d) axial results.

when subjected to stress concentrations [20]. In this case, stress is concentrated in the geometrical discontinuity caused by the reduction in cross-section area of the shaft. $k$ accounts for the end conditions of the shaft. As it can be seen in the setup photos, shaft fixation to load cell does not allow rotation but it can occur some translation. On the other shaft's end, rotation and translation are fixed, resulting in $k$ = 2. This results in a theoretical maximum compressive load of 39.30 N. Thus, the measured critical load magnitude shows an error of only 10% compared to theoretical value.

The maximum insertion and extraction forces during implantation and extraction were also measured using two different mediums: 0.6% agar gel (n = 20) and calf cadaver brain (n = 20). Figure 4.13 shows the setup arrangement for testing both mediums: shafts were fixed to the dynamo-meter perpendicular to medium surface, moving towards it at a certain speed. After the shaft fully penetrates the medium, it stops for a few seconds before starting extraction tests. For both mediums, three different speeds were used: 50 mm.min$^{-1}$ (n = 20), 120 mm.min$^{-1}$ (n = 10) and 180 mm.min$^{-1}$ (n = 10).

Implantation and extraction tests (Figure 4.13c to e) reveal quick increase of the force for the
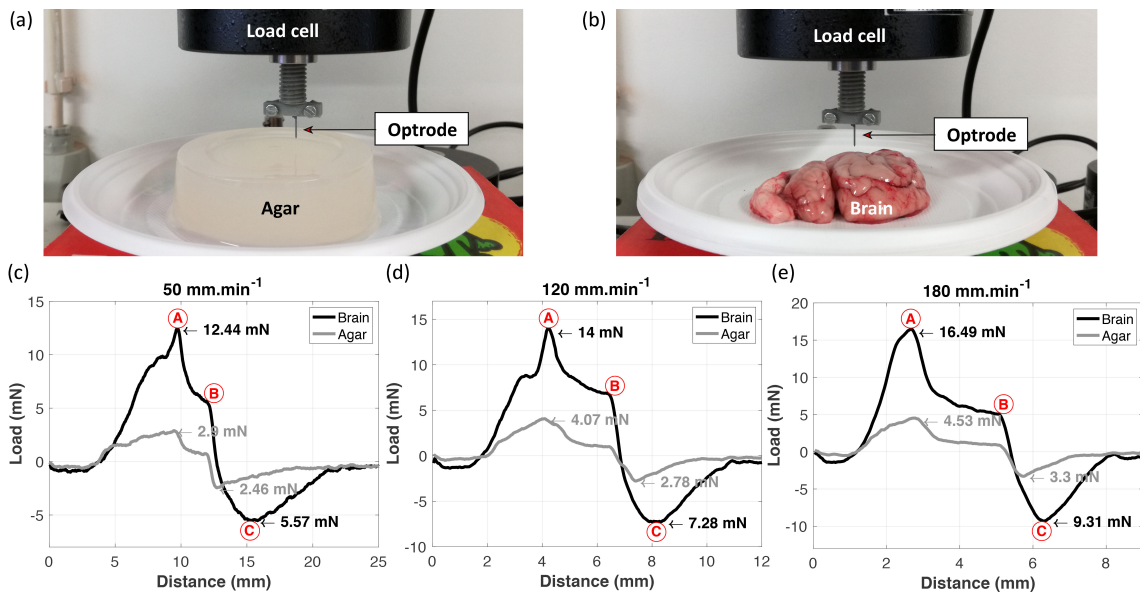
**Figure 4.13:** Experimental setup photo used in mechanical tests on (a) 0.6% agar gel, and (b) calf cadaver brain. Average displacement vs force plots for implantation and extraction trials at (c) 50 mm.min$^{-1}$, (d) 120 mm.min$^{-1}$ and (e) 180 mm.min$^{-1}$.

initial insertion phase, as the shaft is subject to medium resistance. At this point, the shaft reaches its peak force (moment A), until its tip pierces gel or brain surface. After implantation, the load required to penetrate the substrate is quickly reduced (moment B). At the time of shaft extraction, an increase in the required load (moment C, absolute value) is achieved until a complete detachment between the shaft and the tested medium happens (load stabilizes $\approx$ 0 N).
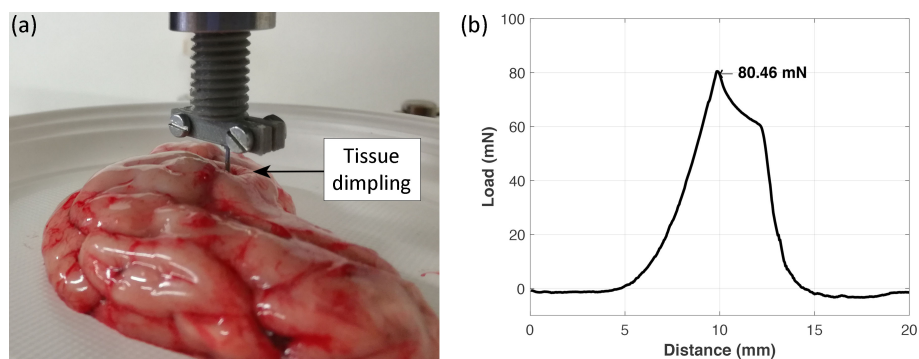


**Figure 4.14:** (a) Brain dimpling during an implantation test without dura removal. (b) Average displacement vs force plot for implantation tests at 50 mm.min$^{-1}$.

The average forces require to implant and extract the shaft of the optrode device are presented in Table 4.3. Implantation required load to pierce the 0.6% agar gel and calf brain tissue was around

**Table 4.3:** Average load required for implantation and extraction trials of the devices into agar gel and brain tissue mediums, at different speeds.

| Speed | Unit | Implantation load | | Extraction load | |
|---|---|---|---|---|---|
| | | 0.6% Agar | Calf Brain | 0.6% Agar | Calf Brain |
| 50 mm.min$^{-1}$ | mN | $2.90 \pm 0.32$ | $12.44 \pm 3.23$ | $2.46 \pm 0.01$ | $5.57 \pm 1.12$ |
| 120 mm.min$^{-1}$ | mN | $4.07 \pm 0.45$ | $14.00 \pm 5.17$ | $2.78 \pm 0.26$ | $7.28 \pm 0.63$ |
| 180 mm.min$^{-1}$ | mN | $4.53 \pm 0.13$ | $16.49 \pm 5.07$ | $3.30 \pm 0.01$ | $9.31 \pm 1.03$ |

3.83 mN and 14.31 mN, respectively, for all speeds. During shafts extraction, the required force was 2.85 mN and 7.39 mN for agar and brain, respectively, for all speeds. In tests performed with calf brains, dura mater layer was removed for load measurements. Attempts of shafts implantation with dura layer (n = 5) showed significant brain tissue dimpling, hindering shaft penetration into the medium. This phenomenon is shown in Figure 4.14a, where tissue penetration required $80.46 \pm$ 7.08 mN to occur (Figure 4.14b).

## 4.4  Electrochemical results

EIS measurements were used to characterize the impedance of the $50 \times 50$ $\mu$m$^2$ Pt recording sites of optrode devices. The setup used for these tests is shown in Figure 4.15. Measurements were performed in a Gamry system (Gamry Instruments, Reference 600$^{TM}$), using a standard three-electrode configuration (Figure 4.15a): $40 \times 40 \times 0.25$ mm$^3$ Pt foil as counter electrode, Ag|AgCl as reference electrode, and 0.9% NaCl solution as electrolyte at room temperature. Impedance was measured for frequencies from 100 Hz to 1 MHz at a constant 10 mV AC voltage. In this setup, all microelectrodes were connected to the ground (except the one being tested) to prevent capacitive coupling between them. Figure 4.15b presents the average impedance values (n = 10) of 400.80 $\pm$20.32 k$\Omega$ and capacitive phase angle (n = 10) of $68.86 \pm 2.96°$, at 1 kHz.

Device lifetime test requires performing EIS measurements when the probe is soaked in a heated electrolyte. The setup used was practically the same as presented in Figure 4.15a, with the exception that for these tests, electrolyte was PBS and its container was heated to 80 °C. Impedance values were recorded every 24 h until failure occurs. Failure was defined as a substantial change in
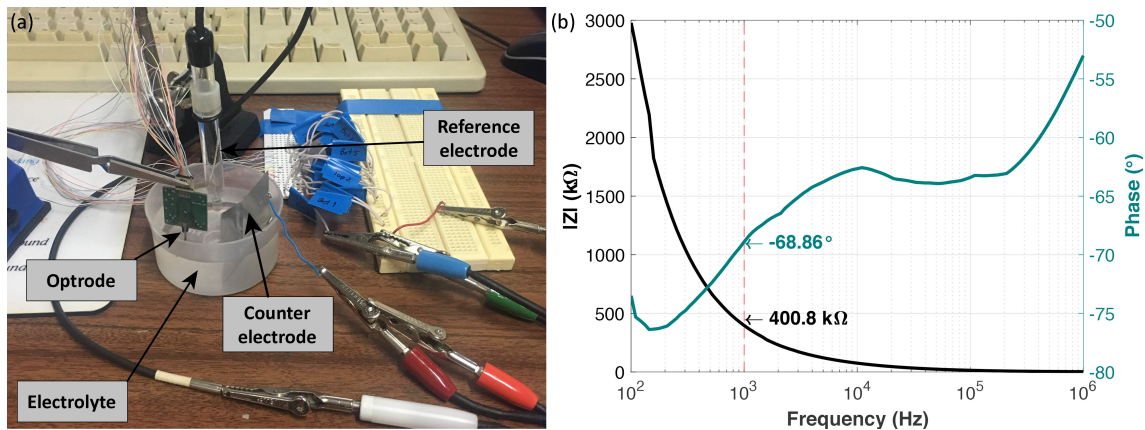
**Figure 4.15:** (a) Experimental setup used for electrochemical tests on the optrode. (b) Bode diagram for the $50 \times 50 \ \mu m^2$ Pt recording sites of optrode device.
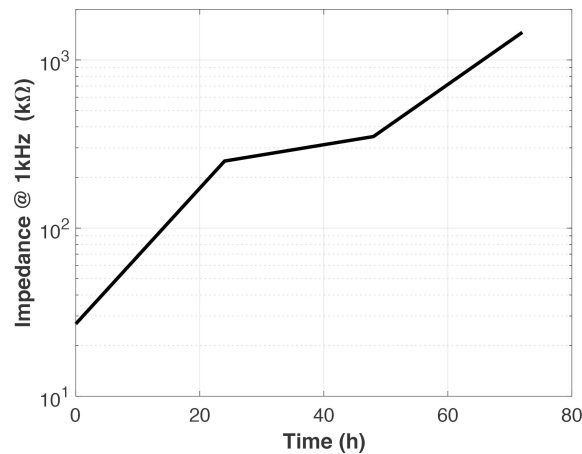


**Figure 4.16:** Average recording sites impedance at 1 kHz in function of soak time at 80 °C.

impedance at 1 kHz (> 1MHz), indicating an open circuit due to conductor fracturing/dissolution.

Figure 4.16 shows the impedance results of 10 recording sites of probes (n = 5) over time. After 72 h soaked in the heated saline solution, the average impedance of the recording sites increased from about 200 k$\Omega$ to above 1.3 M$\Omega$. Therefore, the MTTF considered was 48 h, as it was the last experimental results with the impedance under 1 M$\Omega$. Using the Equation 3.5 at $T$ = 80°C, the activation energy ($\Delta A\ddagger$) was calculated. The lifetime at physiological temperature (37 °C) was estimated using Equation 4.1. Table 4.4 summarizes the parameters used to calculate the accelerated lifetime testing, which results in a physiological lifetime is approximately two years.

$$Lifetime \ (T \ = \ 37\,^\circ C) \ = \ \frac{h}{k_B T} e^{\frac{\Delta A\ddagger}{RT}} \tag{4.1}$$

Table 4.4: Accelerated lifetime testing parameters and result.

| Parameter | Value |
|---|---|
| MTTF | 48 h |
| Soak temperature | 353.15 K |
| Physiological temperature | 310.15 K |
| $\Delta A\ddagger$ | 123 kJ.mol$^{-1}$ |
| Lifetime | 2.02 years |

## 4.5 Optical results

Optical measurements aim to prove that optrode device provides enough light intensity to the tissue at the expected wavelength. Figure 4.17a shows the setup used to measure LED peak wavelength. For this measurement, optrodes are aligned with the monochromator (74125, Newport) inlet. Connected to the monochromator is a photodiode detector (71675, Newport) that records the current generated for a range of wavelengths (350-550 nm). The LED peak wavelength is the one that emits the highest current. Figure 4.17c shows that LEDs peak wavelength is 467 nm (n = 3). This value is confirmed by the LED chip datasheet. LEDs employed in the devices are commercial chip and its datasheet reports a peak wavelength from 467 nm to 473 nm.

LED light power was measured using a photodiode sensor (FDS100-CAL, Thorlabs), coupled to a 1 mm diameter pinhole (P1000D, Thorlabs). Connected to the photodiode is a power meter (1918-R, Newport) that records the current generated by the LED. Figure 4.17b shows the setup used to measure LED light intensity. From Equation 3.6 and the photodiode responsivity ($\Re$) at 467 nm (0.14 A/W), the LED optical power was calculated. Figure 4.17d shows the result of the light intensity emitted by the LED chips as a function of its driven current. At its maximum forward current (20 mA), LED chips are capable of delivering 1.2 mW.mm$^{-2}$ intensity of light.

## 4.6 Characterization discussion

Mechanical tests comprehending compression strength tests, implantation and extraction forces were presented. Si 8 mm long shafts demonstrated to be more robust when longitudinal loads are
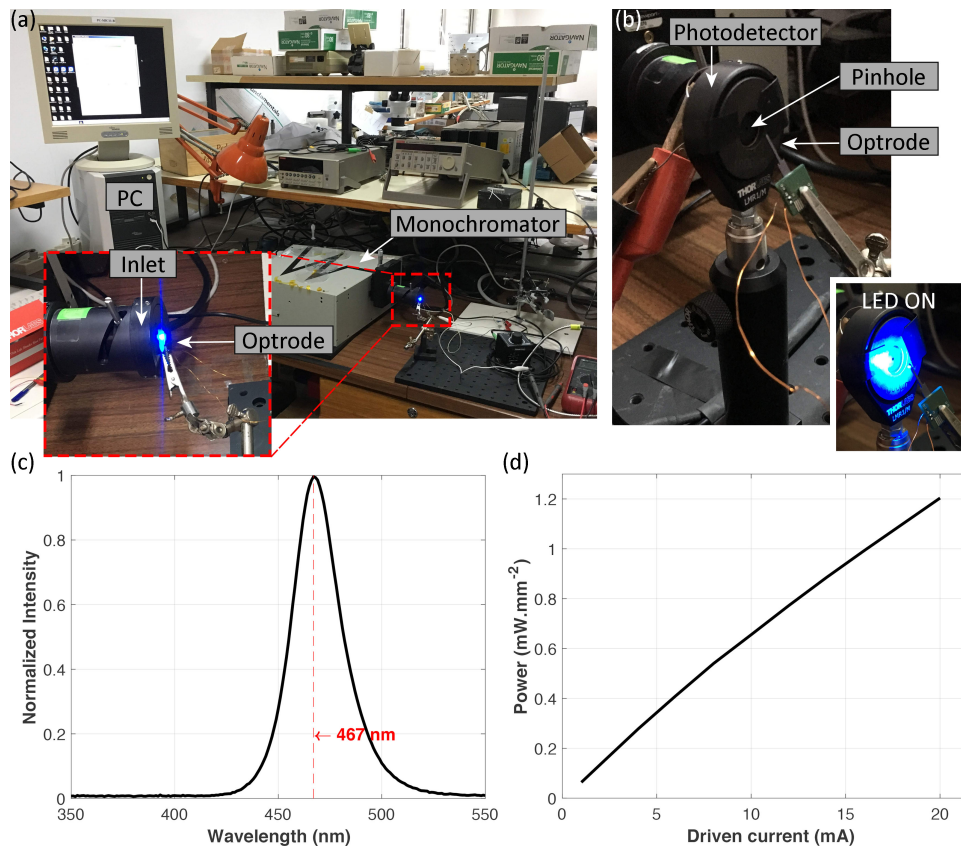
**Figure 4.17:** Experimental setup used for optical tests on the optrode. (a) Peak wavelength and (b) optical power measurements apparatus. (c) LED chip normalized light intensity as a function of the wavelength. (d) Optical power vs LED driven current graph.

applied than with axial forces. This presents as an advantageous feature, since longitudinal forces are the ones playing a key role while implanting devices into the brain [21]. This phenomenon is particularly relevant for long-shafts devices, where small cross-section combined with enhanced length inevitably result in more frail devices.

Average implantation and extraction forces differ from medium, speed applied and test performed, as shown in Table 4.3. Implantation tests consistently required higher forces than with extraction. In average, piercing the agar medium with the probes takes more 25% effort than to extract it, whilst in the brain, implantation forces are 50% higher than extraction. Average implantation and extraction forces for both mediums are in the magnitude of tens of mN (2.9 nM to 16.49 mN). Those values are consistent with those reported in literature for Si shafts [5, 7, 22]. As expected, extraction forces have consistently lower magnitudes, as they only represent drag forces

between the device and the surrounding material.

For both mediums, higher speeds averagely required higher implantation and extraction forces. Although this is true for most cases, implantation tests in brain tissue presents high standard deviation values, which makes it difficult to reach a correlation between the increased speed and load. Nonetheless, low insertion speeds are expected to result in lower required forces, as they generate less vibration and better accommodation of the implant to the tissue [22].

For all tests, brain tissue trials required higher forces to penetrate and remove the shafts compared to agar gel medium: $\approx$ 70% and $\approx$ 60% higher forces for implanting and removing the probes, respectively. A possible explanation for this difference between mediums could be due to heterogeneous structure of the brain, which could difficult shaft movement and considerably affect tissue deformation. This suggests that the shaft robustness is dependent on medium composition. Moreover, probe implantation with dura layer represents an increase of more than 85% in the load needed to pierce the brain. Therefore, dura mater layer must be removed before probe implantation.

Other reported long-shaft designs prove not be able to withstand the forces exerted by the neural tissue during implantation, eventually breaking [21]. In this work, mechanical characterization demonstrated overall robust high-length shaft probes. In both the agar gel and brain tissue, none of the tested samples showed any sign of shaft breakage during and after trials.

Electrochemical results for the fabricated $50 \times 50$ $\mu$m$^2$ sputtered Pt recording sites show impedance magnitudes below M$\Omega$. These values are reported to be suitable for electrophysiology studies [23]. With a negative phase angle, Pt recording sites show capacitive behavior. This feature is more relevant for recording sites that are also used for neural stimulation. With this technique, charges are applied to the surface of the electrode and constant reduction and oxidation reactions take place at the electrode-electrolyte interface. Charge-injection can be based on capacitive or faradaic currents, depending on the electrode material. The last is more desirable because, in principle, no chemical species are created or consumed during a stimulation pulse [24].

Accelerated lifetime testing aims to be a preliminary study to assess probes reliability for chronic recording experiments. By increasing recording environment temperature, the failure mechanism is accelerated [25]. Results show an estimated physiological lifetime up to two years. Since the most common implant duration in a mouse brain is several weeks [26], the fabricated interface could be a promising tool for reliable chronic in vivo neural recordings.

Photostimulation capability of an optrode device is validated by measuring the power intensity of the light source at a specific wavelength. Reported minimum light intensity to promote a biological effect in engineered cells is 1 mW.mm$^{-2}$ [27]. At 467 nm (peak wavelength), LED chip used in the optrode showed a result of 1.2 mW.mm$^{-2}$, which suggests that the fabricated optrode is capable of photostimulation cells engineered with a blue-light sensitive opsin.

Although LED chip transferring technique presents several advantages previously discussed, a major drawback is the impossibility of increasing the optical power, once it reaches the maximum driven current of the LED chip. In this case, the LED chip allows to forward a continuously current of 20 mA. A possible solution consists on using a photostimulation protocol with discrete light pulses that would enable to increase light intensity at specific times.

By directly exposing light sources to tissue, LED-based optrodes could be easily affected by overheating around the stimulation focus area, as light emitter converts energy into heat [28]. Rises in temperature of approximately 2 °C have been used as threshold to prevent brain damage [29], corresponding nowadays to the regulatory limit recommended by the AAMI. This temperature reference may vary depending on different species, animal age and brain activity state [29, 30]. In this regard, McAlinden et al. [31] and, more recently, Dong et al. [32] measured the heating profile of LEDs using thermal cameras. McAlinden et al. [31] measured the temperature rise profile of 40 $\mu$m-diameter GaN LEDS and reported a maximum temperature rise of 1.5 °C over 100 ms light pulse. Dong et al. [32] demonstrated temperature variation over pulsed and continuous illumination regime, using the same forward current (20 mA) and a similar area (240 $\times$ 320 $\mu$m$^2$) LEDs as the emitter proposed in this work (305 $\times$ 338 $\mu$m$^2$). Their results show a maximum temperature rise of 2 °C for 350 ms pulse light train and 3 °C for continuous irradiance over 15 min. This data suggests that the proposed optrode might safely provide photostimulation using discrete light train protocols.

Moreover, an important feature to consider is the activation area of photostimulation that the optrode can provide. Although it was not measured in this work, a good estimation is presented by Dong et al. [32] that measured a 400 $\mu$m penetration depth (depth that can be attained while still presenting the optical power of 1 mW.mm$^{-2}$) for a Lambertian emitter. The LED chip used for the fabricated optrode is an ideal diffuse radiator, suggesting that light can reach up to a depth of 400 $\mu$m into neural tissue.

# References

[1] F. Wu, E. Stark, P. Ku, K. D. Wise, G. Buzsáki, and E. Yoon, "Monolithically Integrated $\mu$LEDs on Silicon Neural Probes for High-Resolution Optogenetic Studies in Behaving Animals," Neuron, **88**, doi: 10.1016/j.neuron.2015.10.032, 1–13, 2015.

[2] G. Paxinos, and C. Watson, "The Rat Brain in Stereotaxic Coordinates," 6th ed Academic Press, 2007.

[3] A. Bidiville, K. Wasmer, J. Michler, P. Nasch, M. Van der Meer, and C. Ballif, "Mechanisms of wafer sawing and impact on wafer properties," Prog Photovolt Res Appl, **18**(8), doi: 10.1002/pip.972, 563-572, 2010.

[4] Z. Wang, J. Wang, S. Lee, S. Yao, R. Han, and Y. Su, "300 mm low-k wafer dicing saw development," IEEE Trans Electronics Packaging Manufacturing, **30**(4), doi: 10.1109/ICEPT.2005.1564687, 313-319, 2007.

[5] W. Jensen, K. Yoshida, and U. G. Hofmann, "In-Vivo Implant Mechanics of Flexible, Silicon-Based ACREO Microelectrode Arrays in Rat Cerebral Cortex," IEEE Trans. Biomed. Eng., **53**(5), doi: 10.1109/TBME.2006.872824, 934-940, 2006.

[6] M. Han, P. S. Manoonkitiwongsa, C. X. Wang, and D. B. McCreery, "In Vivo Validation of Custom-Designed Silicon-Based Microelectrode Arrays for Long-Term Neural Recording and Stimulation," IEEE Trans. Biomed. Eng., **59**(2), doi: 10.1109/TBME.2011.2172440, 346-354, 2012.

[7] A. A. Sharp, A. M. Ortega, D. Restrepo, D. Curran-Everett, and K. Gall, "In Vivo Penetration Mechanics and Mechanical Properties of Mouse Brain Tissue at Micrometer Scales," IEEE Trans. Biomed. Eng., **56**(1), doi: 10.1109/TBME.2008.2003261, 45-53, 2009.

[8] C. M. Lopez, J. Putzeys, B. C. Raducanu, M. Ballini, S. Wang, A. Andrei, V. Rochus, R. Vandebriel, S. Severi, C. Hoof, S. Musa, N. Helleputte, R. F. Yazicioglu, and S. Mitra, "A Neural Probe With Up to 966 Electrodes and Up to 384 Configurable Channels in 0.13 $\mu$m SOI CMOS," IEEE Trans. Biomed. Eng., **11**(3), doi: 10.1109/TBCAS.2016.2646901, 510-522, 2017.

[9] J. Scholvin, J. P. Kinney, J. G. Bernstein, C. Moore-Kochlacs, N. Kopell, C. G. Fonstad, and E. S. Boyden, "Close-Packed Silicon Microelectrodes for Scalable Spatially Oversampled Neural Recording," IEEE Trans. Biomed. Eng., **63**(1), doi: 10.1109/TBME.2015.2406113, 120-130, 2016.

[10] B.C. Raducanu, R. F. Yazicioglu, C. M. Lopez, M. Ballini, J. Putzeys, S. Wang, A. Andrei, V. Rochus, M. Welkenhuysen, N. V. Helleputte, S. Musa, R. Puers, F. Kloosterman, C. V. Hoof, R. Fiáth, I. Ulbert, and S. Mitra, "Time Multiplexed Active Neural Probe with 1356 Parallel Recording Sites," Sensors, **17**, doi: 10.3390/s17102388, 2388, 2017.

[11] T. I. Kim, J. G. McCall, Y. H. Jung, X. Huang, E. R. Siuda, Y. Li, J. Song, Y. M. Song, H. A. Pao, R. H. Kim, C. Lu, S. D. Lee, I. S. Song, G. Shin, R. Al-Hasani, S. Kim, M. P. Tan, Y. Huang, F. G. Omenetto, J. A. Rogers, and M. R. Bruchas, "Injectable, Cellular-Scale Optoelectronics with Applications for Wireless Optogenetics," Science, **340**(6129), doi: 10.1126/science.1232437, 6129, 211-216, 2013.

[12] R. Scharf, T. Tsunematsu, N. McAlinden, M. D. Dawson, S. Sakata, and K. Mathieson, "Depth-specific optogenetic control in vivo with a scalable, high-density $\mu$LED neural probe," Nature Scientific Reports, **8**, doi: 10.1038/srep28381, 28381, 2016.

[13] K. Y. Kwon, B. Sirowatka, A. Weber, and W. Li, "Opto-$\mu$EcoG Array: A Hybrid Neural Interface With Transparent $\mu$EcoG Electrode Array and Integrated LEDs for Optogenetics," IEEE Transactions on Biomedical Circuits and Systems, Rotterdam, Netherlands, **7**(5), doi: 10.1109/TBCAS.2013.2282318, 593-600, 2013.

[14] H. Cao, L. Gu, S. K. Mohanty, and J. C. Chiao, "An Integrated $\mu$-LED Optrode for Optogenetic Stimulation and Electrical Recording," IEEE Transaction on Biomedical Engineering, **60**(1), doi: 10.1109/TBME.2012.2217395, 225-229, 2013.

[15] S. Ayub, C. Gossler, M. Schwaerzle, E. Klein, O. Paul, U. T. Schwarz, and P. Ruther, "High-Density Probe With Integrated Thin-Film Micro Light Emitting Diodes ($\mu$-LEDs) For Optogenetic Applications," Proc MEMS, Shangai, China, 379-382, 2016.

[16] C. Goβler, C. Bierbrauer, R. Moser, M. Kunzer, K. Holc, W. Pletschen, K. Köhler, J. Wagner, M. Schwaerzle, P. Ruther, O. Paul, J. Neef, D. Keppeler, G. Hoch, T. Moser, and U. T. Schwarz, "GaN-based micro-LED arrays on flexible substrates for optical cochlear implants," J. Phys. D: Appl. Phys, **47**, doi: 10.1088/0022-3727/47/20/205401, 205401, 2014.

[17] N. McAlinden, E. Gu, M. D. Dawson, S. Sakata, and K. Mathieson, "Optogenetic activation of neocortical neurons in vivo with a sapphire-based micro-scale LED probe," Frontiers in Neural Circuits, **9**, doi: 10.3389/fncir.2015.00025, 25, 2015.

[18] S. Ayub, L. J. Gentet, R. Fiàth, M. Schwaerzle, M. Borel, F. David, P. Barthó, I. Ulbert, O.

Paul, and P. Ruther, "Hybrid intracerebral probe with integrated bare LED chips for optogenetic studies," Biomed Microdevices, **19**, doi: 10.1007/s10544-017-0190-3, 49, 2017.

[19]  E. J. Tehovnik, "Electrical stimulation of neural tissue to evoke behavioral responses," Journal of Neuroscience Methods, **65**(1), doi: 10.1016/0165-0270(95)00131-X, 1-17, 1996.

[20]  M. A. Hopcroft, W. D. Nix, and T. W. Kenny, "What is the Young's Modulus of Silicon?," Journal of Microelectromechanical Systems, **19**(2), doi: 10.1109/JMEMS.2009.2039697, 229-238, 2010.

[21]  M. Hajjhassan, V. Chodavarapu and S. Musallam, "NeuroMEMS: Neural Probe Microtechnologies," Sensors, vol. 8(10), doi: 10.3390/s8106704, 6704-6726, 2008.

[22]  K. J. Paralikar, and R. Clement, "Collagenase-Aided Intracortical Microelectrode Array Insertion: Effects on Insertion Force and Recording Performance," IEEE Transactions on Biomedical Engineering, **55**(9), doi: 10.1109/TBME.2008.923150, 2258-2267, 2008.

[23]  S. Negi, R. Bhandari, L. Rieth, and F. Solzbacher, "In vitro comparison of sputtered iridium oxide and platinum-coated neural implantable microelectrode arrays." Biomed. Mater., **5**, doi: 10.1088/1748-6041/5/1/015007, 015007, 2010.

[24]  S. F. Cogan, "Neural Stimulation and Recording Electrodes," Annu. Rev. Biomed. Eng., **10**, doi: 10.1146/annurev.bioeng.10.061807.160518, 275-309, 2008.

[25]  L. A. Escobar, and W. Q. Meeker, "A Review of Accelerated Test Models," Statist. Sci., **21**(4), doi: 10.1214/088342306000000321, 552-577, 2007.

[26]  G. Kook, S. W. Lee, H. C. Lee, I. Cho, and H. J. Lee, "Neural Probes for Chronic Applications," Micromachines, **7**(10), doi: 10.3390/mi7100179, 179, 2016.

[27]  E .S. Boyden, F. Zhang, E. Bamberg, G. Nagel, and K. Deisseroth, "Millisecond-timescale, genetically targeted optical control of neural activity," Nat. Neurosci., **8**(9), doi: 10.1038/nn1525, 1263–1268, 2005.

[28]  M. T. Alt, E. Fiedler, L. Rudmann, J. S. Ordonez, P. Ruther, and T. Stieglitz, "Let There Be Light - Optoprobes for Neural Implants," Proceedings of the IEEE, **105**, doi: 10.1109/JPROC.2016.2577518, 101-138, 2017.

[29]  C. Childs, "Human brain temperature: regulation, measurement and relationship with cerebral trauma: Part 1," British Journal of Neurosurgery, **22**, doi: 10.1080/02688690802245541, 486-496, 2008.

[30] E. A. Kiyatkin, "Brain Hyperthermia During Physiological and Pathological Conditions: Causes, Mechanisms, and Functional Implications," Current Neurovascular Research, **1**, doi: 10.2174/1567202043480233, 77-90, 2004.

[31] N. McAlinden, D. Massoubre, E. Richardson, E. Gu, S. Sakata, M. D. Dawson, and K. Mathieson, "Thermal and optical characterization of micro-LED probes for in vivo optogenetic neural stimulation," Optics Letters, **38**(6), doi: 10.1364/OL.38.000992, 992-994, 2013.

[32] N. Dong, R. Berlinguer-Palmini, A. Soltan, N. Ponon, A. O'Neil, A. Travelyan, P. Maaskant, P. Degenaar, and X. Sun, "Opto-electro-thermal optimization of photonic probes for optogenetic neural stimulation," J. Biophotonics, **30**, doi: 10.1002/jbio.201700358, e201700358, 2018.

# Chapter 5

# Acute In Vivo Studies

In this chapter in vivo recording and optical stimulation studies are presented using different probes solutions. For the extracellular electrophysiology recordings, it was used high-density close-packed probes developed at the Massachusetts Institute of Technology (MIT). For photostimulation experiments, a commercial tetrode bundle was employed. The apparatus, results and analysis pipeline are detailed in the next sections. The electrophysiology experiments were performed in Boyden Lab (headed by Edward Boyden), the Synthetic Neurobiology Group, at MIT (Boston, USA), and the optogenetic study was done in Costa Lab (headed by Rui Costa) at Champalimaud Foundation (Lisbon, PT).

## 5.1 Extracellular electrophysiology recordings using close-packed probes

### 5.1.1 Probe design and preparation

Two types of probes were used in the extracellular recording experiments, both showing high-density and close-packed recording sites, fabricated in a hybrid lithography process. Recording sites that are closely packed, such as in tetrodes, enable spatial oversampling of neural activity, which means recording the activity of a single neuron from multiple points in space. Such spatial oversampling helps greatly with data analysis (the "spike sorting" problem), in which recorded electrical events
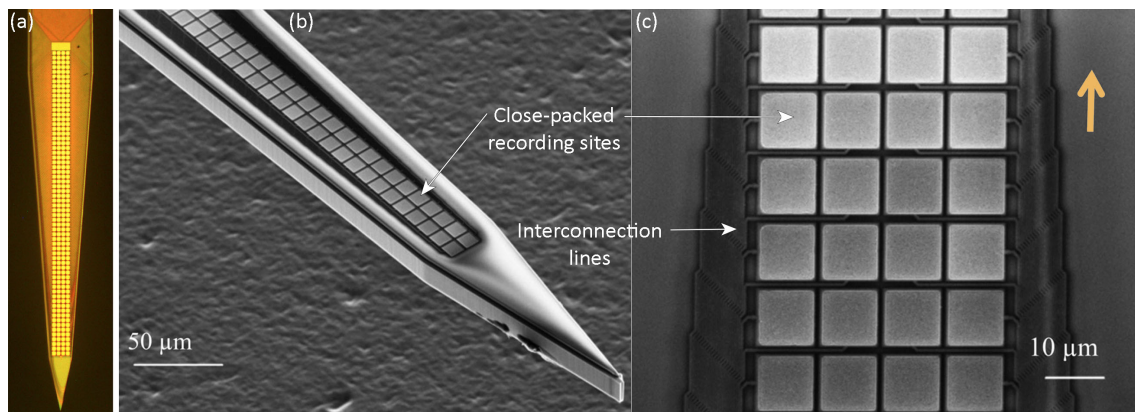
**Figure 5.1:** (a) Close-packed recording sites on the Si shaft. (b) SEM of the tip of a recording shaft with two columns of 100 rows each. (c) Top-down view SEM of a four-column Au electrodes probe [2].
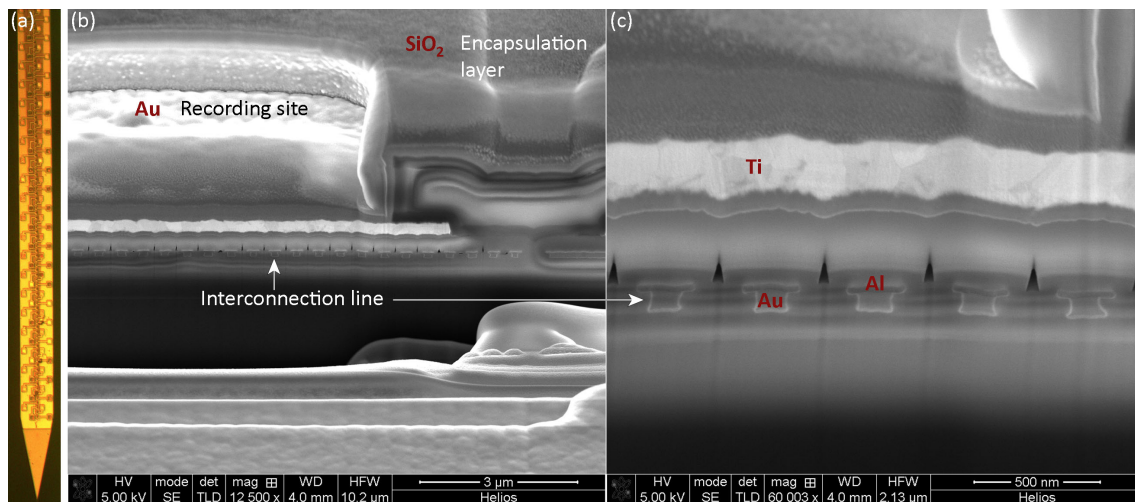


**Figure 5.2:** (a) Most recent close-packed design probe. Tilted FIB views detailing critical structures of the probe: (b) Ti/Au recording site overview, and (c) electrically insulated metal wiring (Al/Ti).

are attributed to individual neurons [1].

Figure 5.1 and 5.2 show the two probes used for the in vivo recordings. The manufacturing process of the probe shown in Figure 5.1 is described elsewhere [2], while the probe shown in Figure 5.2 is still under development and not published yet. The manufacturing process, in both cases, results in a single-shaft probe with a dense array of recording sites (up to 256 channels per shaft), organized differently on the shaft.

Figure 5.1a shows a top view image of the 256-electrodes probe. All microscope images were taken with a 5X-50X LED Binocular Compound microscope (AmScope, USA). Au recording sites are

**Figure 5.3:** (a) Setup used for Au wirebonding the probes to PCB. (b) Photo of a final and packaged device mounted in a PCB and with black epoxy encapsulation.

arranged in four columns by sixty-four rows, at the shaft tip, and distributed along its axis, spanning 1-1.5 mm. Electrodes dimensions are $9 \times 9$ $\mu$m$^2$ with a pitch of 11 $\mu$m, visible as the light squares in SEM images (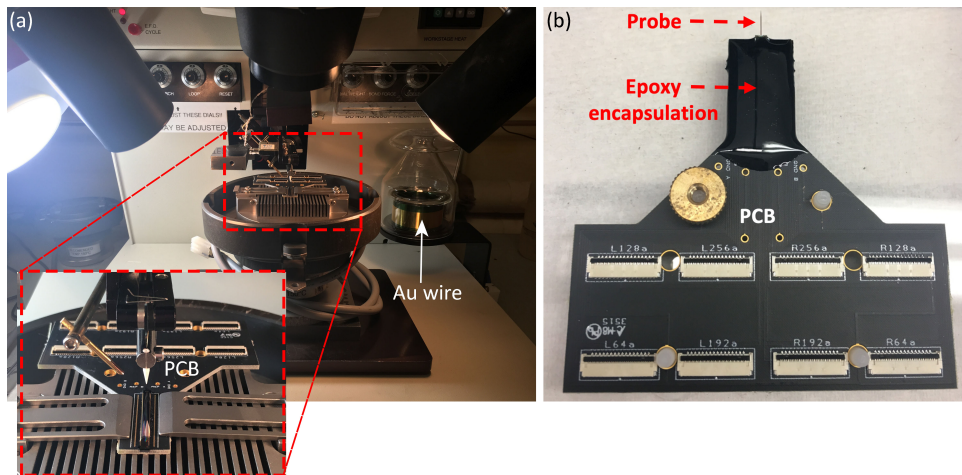Orion NanoFab Helium Ion Microscope, Zeiss, USA) of Figure 5.1b and c. Probes length is between 4 and 5 mm and are 15 $\mu$m thick. Insulated metal interconnection lines run along the length of the shank, visible as dark lines flanking the rows of light squares. The tip shaft has a width of $\approx$50 $\mu$m in the region shown in Figure 5.1b. Shaft width increases along its length up to 200 $\mu$m so it can accommodate all the interconnection lines. The center columns are connected by wiring running in-between the outer pads, and all columns are then collected and routed along the two sides. The direction toward the shank tip is indicated by the yellow arrow in Figure 5.1c.

Figure 5.2a presents the most recent single-shaft probe design with 128 recording sites. In terms of design, the main differences of this probe compared to the probe shown in Figure 5.1 are (i) the recording points distribution on the shaft and (ii) uniform and reduced width ($\approx$70 $\mu$m). The recording sites are connected to submicron dimension dual wiring layer that runs under the recording sites, as it shows in transversal FIB images (Helios Nanolab 600 Dual Beam Focused Ion Beam Milling System, ThermoFisher Scientific, USA) in Figures 5.2b and c. The dual-metal layer allows to reduce the overall width of the probe. FIB images were used to assess surface structures, as well as their topology. These images are also important to debug possible defects introduced during the probe fabrication.

After fabrication, probes are connected to a PCB and are wirebonded with Au wire (1204W,
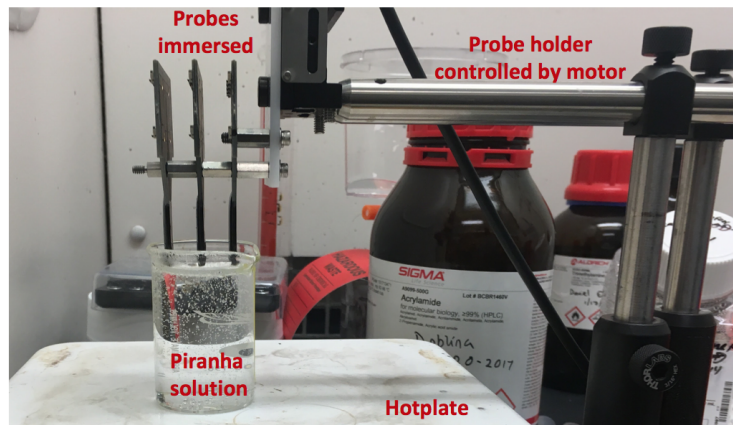
**Figure 5.4:** Cleaning probes setup.

Mech-EI Industries Inc., USA). Figure 5.3a shows the wirebonding setup and the result of probe packaging (Figure 5.3b). A layer of black epoxy encapsulates and protects wirebonding connections.

Prior to the recordings and in order to removed possible organic materials, probes are cleaned by immersion in base piranha solution (5:1:1 DI water, 30% hydrogen peroxide ($H_2O_2$) and 30% ammonium hydroxide ($NH_4OH$)) for 10 min, at 70°, and then rinsed with DI water. This step is carried out in a chemical hood, using the proper personal protection equipment. Figure 5.4 shows the setup used for the probes cleaning protocol.

A standard step to improve the quality of recorded biosignals is to perform EIS measurements and ensure a suitable impedance of recording sites [3]. In the case of these probes, due to the small area of the electrodes (81 $\mu m^2$), impedance values were consistently over 1 M$\Omega$, and a strategy was needed to reduce it. Changing the surface properties of a recording site to improve its electrical characteristics is a common practice [4, 5]. PEDOT coatings for neural stimulation and recording electrodes have been widely reported [6]. PEDOT is an electrically conducting polymer (ECP) that, like iridium oxide, exhibits both electronic and ionic conductivity. PEDOT has emerged as the most promising of the ECPs, and it can drastically decrease recording site impedance, which in turn is hypothesized to reduce thermal noise and signal loss through shunt pathways [7].

PEDOT was coated over Au recording sites by electrodeposition. In this process, there is anion doping of PEDOT, which is necessary to obtain the high electronic conductivity required for low-impedance recording or for charge-injection. PEDOT solution was obtained by mixing the monomer 3,4-Ethylenedioxythiophene (EDOT, 483028, Sigma-Aldrich) and Poly(sodium 4-styrenesulfonate)
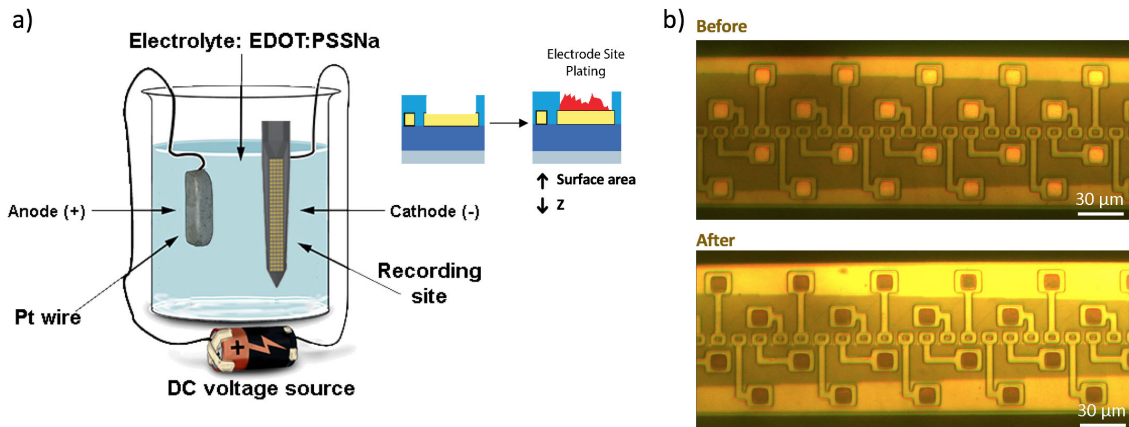
**Figure 5.5:** (a) Schematic of electroplating setup. (b) Results showing Au recording sites surface before and after plating with PEDOT.
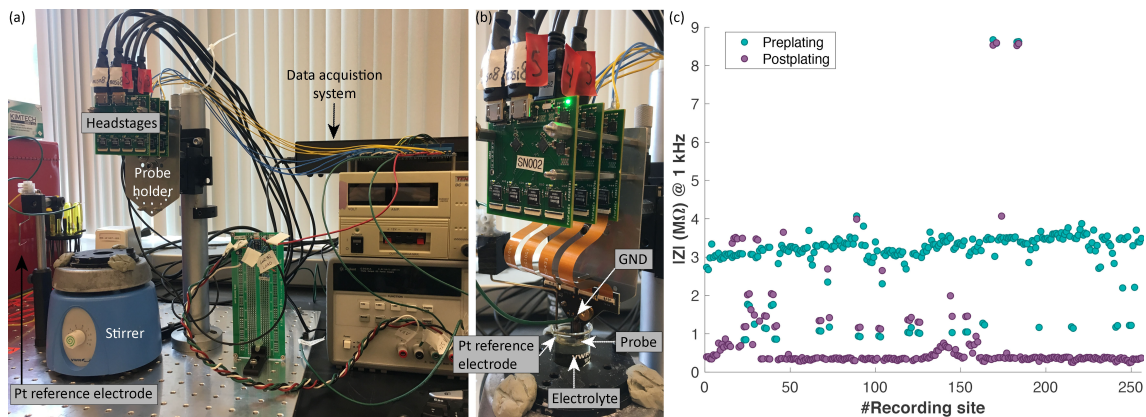


**Figure 5.6:** (a) EIS and plating setup using Willow system. (b) EIS measurement setup. (c) Impedance magnitude results of a 256-channel probe, before and after electrodeposition of PEDOT over the Au recording sites.

solution (PSS, 527483, Sigma-Aldrich) with DI water. PSS is used as the dopant, which is incorporated into the polymer during the electropolymerization process [8–10]. PSS is physically entrained in the EDOT solution and forms a charge-transfer complex that results in oxidation of the PEDOT and consequent high electronic conductivity. EDOT:PSS combination, here referred as PEDOT, was reported to retain approximately 90% of the original electrochemical properties after long-term implantation [11].

The setup and concept of electrodeposition of PEDOT in Au recoding sites of close-packed probes is illustrated in Figure 5.5a. This process was carried out at room temperature using magnetic stirring of the electrolyte (PEDOT). Currents of 1 nA were applied for 10 s per electrode.

Both EIS and electrodeposition processes were performed using the Willow system (LeafLabs, USA). Figure 5.5b shows recording sites surface before and after plating with PEDOT. The plating results are visible in the images as Au recording sites switch from gold-color to a brown-color surface after plating.

EIS measurements employed a two-electrodes configuration (Figure 5.6a): recording site as working electrode, Pt wire as counter electrode, and 0.9% NaCl solution as electrolyte at room temperature. Impedance (Z) was measured for 1 kHz at a constant 10 mV AC voltage for each electrode. Figure 5.6b shows an example of measuring impedance for a 256-channel probe before and after plating of PEDOT over the Au recording sites. As it can be observed, the average impedance magnitude (at 1 kHz) decreases from 3 M$\Omega$ to 500 k$\Omega$ for the majority of sites, making them suitable for electrophysiology studies [3].

## 5.1.2 In vivo validation

In vivo recording experiments require a number of steps to perform them and extract biological data. Figure 5.7 shows an illustration of these steps: (1) Promote the interface between probe and brain, which implicates a surgical procedure for a craniotomy, followed by the probe implantation into the animal's brain; (2) Connect probe to the acquisition system (Willow system) and perform electrophysiology studies. Acquisition system is responsible for collecting, amplify and digitalize the data; (3) Extract recorded in vivo raw data from acquisition system and store it into HDF5 format files; (4) Develop software tools for data analysis.
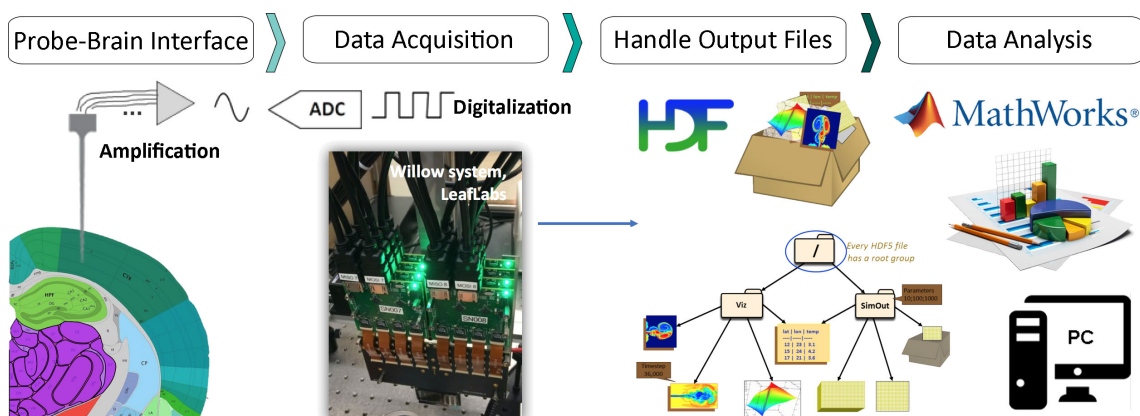


**Figure 5.7:** Schematic of the in vivo recording process flow using the close-packed probes.

### 5.1.3 Surgical procedure

All procedures involving animals were approved by the Committee on Animal Care at MIT (Protocol 1115-111-18). Eleven C57Bl/6 male mice, between 10-12 weeks of age, were implanted with custom-made head plates under 2% isoflurane anesthesia. During surgery, the animals were placed in a rodent stereotaxic frame (David Kopf Instruments, USA). Normothermia ($37°$) was ensured during the procedure using a closed-loop heating pad (Fine Science Tools, USA). As preparation for surgery, the head skin was shaved and cleaned with three alternating scrubs of betadine and 70% alcohol. Then, a small incision was made using a scalpel blade, and fascia was removed using a micro-curette. Three small craniotomies were made using an air drill with a dental burr in it. Then, three stainless steel screws were implanted in the three craniotomies to serve as anchors for the head plate. In addition, the two occipital screws had stainless steel wire (A-M Systems) attached to them, to be used as electrical reference and ground, respectively. The head plate was then placed on top of the skull, with its central aperture around the screws, and affixed to them with dental cement (C&B-Metabond, Parkell). A fourth craniotomy ($\oslash$ = 200-300 $\mu$m) was drilled for probe insertion, either aiming at prefrontal cortex ([2.1 A/P, - 0.8 M/L], nine mice) or to primary somatosensory cortex ([- 2.5 A/P, - 3.5 M/L], two mice). Craniotomies were periodically doused with lactated Ringer's solution to prevent dehydration.

### 5.1.4 Implantation and recording apparatus

Acute recordings were performed immediately after implantation of the head plates, with mice still under isoflurane anesthesia (1.0–1.5%). In preparation for the recording session, mice were affixed to a custom-made metal holder using the head plate, and a cone was placed over the mouse nose for continuous delivery of isoflurane. Normothermia was ensured during recordings with a water-heated pad (Gaymar T/Pump, Braintree Scientific, USA). The back of the probe was painted with DiI, a lipophilic tracer, (2% w/v in ethanol, Millipore, USA) for subsequent histological assessment of the probe position. Before insertion, the probes were positioned perpendicular to the brain surface using a rotation stage (Thorlabs, USA). The probe was inserted at a constant speed of 10 $\mu$m.s$^{-1}$ using a servo motor (Thorlabs, USA) to a final depth of 1.2 mm. The recording setup is shown in Figure 5.8. The electrical ground and reference of the probes were connected to the respective

skull screws. After implantation to its target depth, the probe was allowed to settle for 5 min before starting the recordings. Recordings were made at 30 kHz using a Willow system. Data was recorded continuously in a raw format (filesystem-free) with direct-to-drive data acquisition [12].
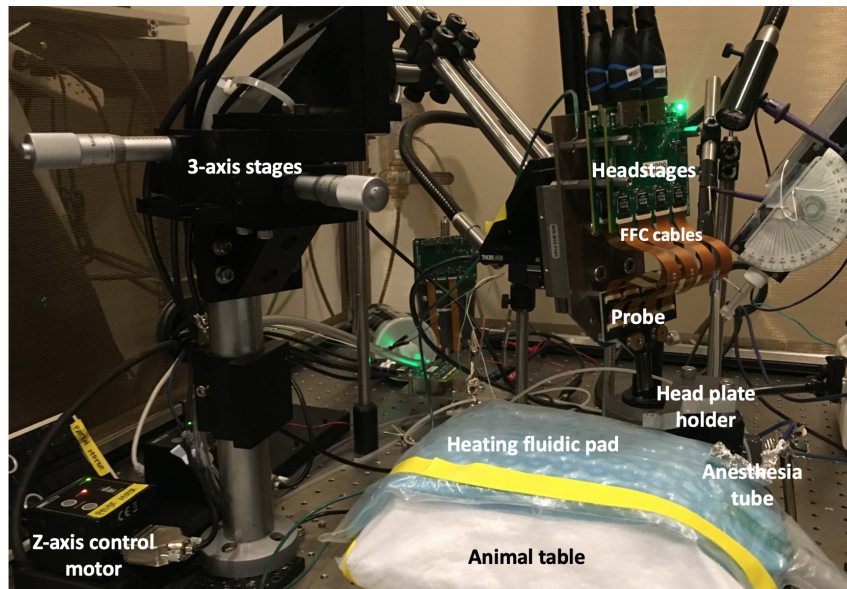


**Figure 5.8:** Setup of the in vivo recordings in mice.

## 5.1.5   Histology

After recordings, mice were euthanized with an anesthetic overdose, and perfused transcardially with 4% paraformaldehyde in 1x PBS. The brains were harvested and sliced on a vibratome to obtain coronal sections 100 $\mu$m thick. The slices were then mounted in glass slides using mounting media that contained DAPI staining (VectaShield, Thermo Scientific, USA). Slices were imaged on a widefield microscope (Nikon Eclipse Ti, USA), and the images were acquired using the NIS Elements software (Nikon, USA).

## 5.1.6   Data acquisition and analysis pipeline

The raw data on the solid-state drives was downloaded and compiled into HDF5 format using the HDF5 library [13] and custom-written scripts. For analysis, it was used MatLab computing environment (The Mathworks), running both built-in and custom-written scripts. The data analysis

flow is illustrated in Figure 5.9. First, signals were pre-processed by bandpass filtering in the frequency band between [0.4-6] kHz to obtain Local Field Potentials (LFP) and in the frequency band between [0.3-500] Hz to obtain spikes. Spike detection and extraction was performed by threshold crossing (voltage peak superior to 25o $\mu$V and minimum peaks distance of 5 ms).
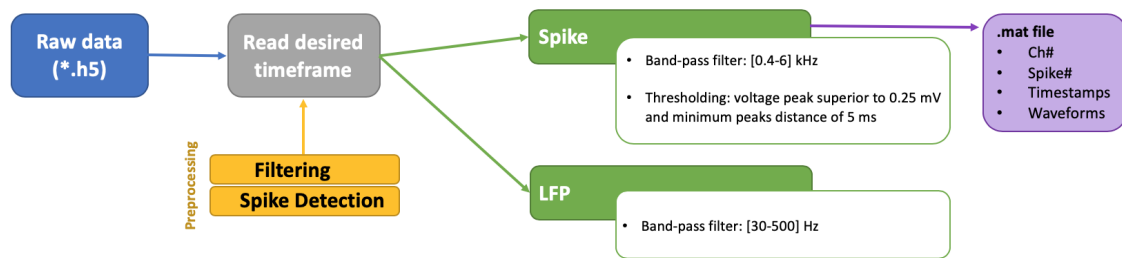


**Figure 5.9:** In vivo data analysis flow.

## 5.1.7 Electrophysiology recording results and discussion

In this section, it is presented the experimental results described in the previous sections from the perspective of the central goal of this work, i.e. demonstration of the capability of the implantable close-packed probes, developed in Boyden lab, to acutely record electrical signals from anesthetized animals. Overall, electrophysiology studies were performed successfully using both close-packed probes. The acute experiments (up to 1 h per experiment) enable to record both extracellular single units (spikes) and LPFs from different areas of the mice's brain tissue. The measurement of this brain activity is crucial since it reflects the highly dynamic flow of information across neural networks [14].

The steps presented for in vivo validation were successfully and consistently accomplished over experiments. The setup used for experiments enable reliable probe implantation due to the use of micrometer-precision motor control stages. Willow system acquired the neural data, generating large output files ($\approx$120 GB for an 1 h experiment), which incurred as an extra challenge to handle, process and analyze data.

After implantation, probes remain precisely positioned at the targeted area inside the brain of the mouse within the entire experiment. The precision of this position was verified with 100 $\mu$m-thick brain slices that were prepared out of the brain of the mice studied in experiments. The different
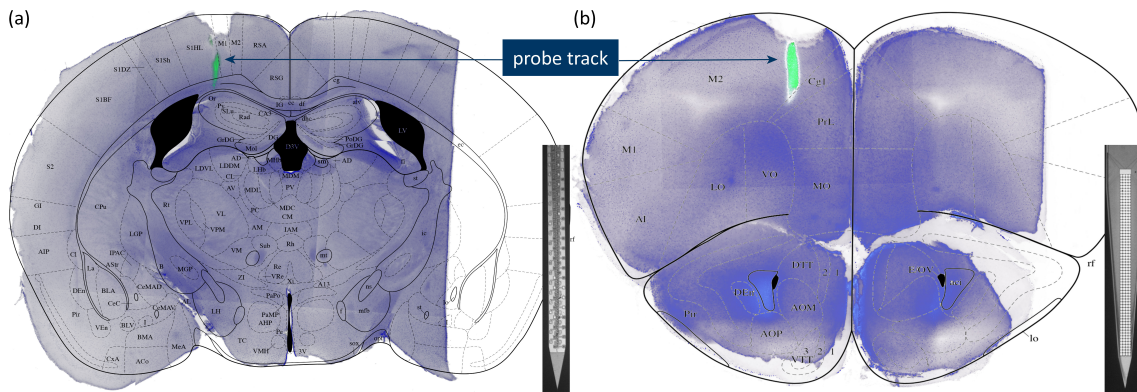
**Figure 5.10:** Histology results. Coronal stained images showings the exact probe position in the mouse brain (green stain). A stereotaxic atlas is overlapped in the stained image for anatomic identification of the probe implantation in (a) primary somatosensory cortex, hindlimb region (S1HL) and (b) secondary motor cortex (M2) in the prefrontal area.

brain structures are visible due to DAPI staining (purple color in Figure 5.10) and the track from the probe is visualized on these slices by means of DiI staining (green color in Figure 5.10). The images of such DAPI-stained slices are shown in Figure 5.10 against the stereotaxic atlas of the mouse brain [15], visualizing the track from the probe positioned in the hindlimb region of primary somatosensory cortex (S1HL) (Figure 5.10a) and the secondary motor cortex (M2) in the prefrontal area (Figure 5.10b). In Figure 5.10a, the staining track position is extended to hippocampus, probably due to the diffusion of DiI tracer in the brain tissue. The damaged region presented in implantation area (slight depression above green traces) happens due to manual drilling of the animal skull during surgery to create craniotomy openings, rather than due to probe implantation. Despite the damage, neural activity is preserved. The drilling effect could be minimized with the
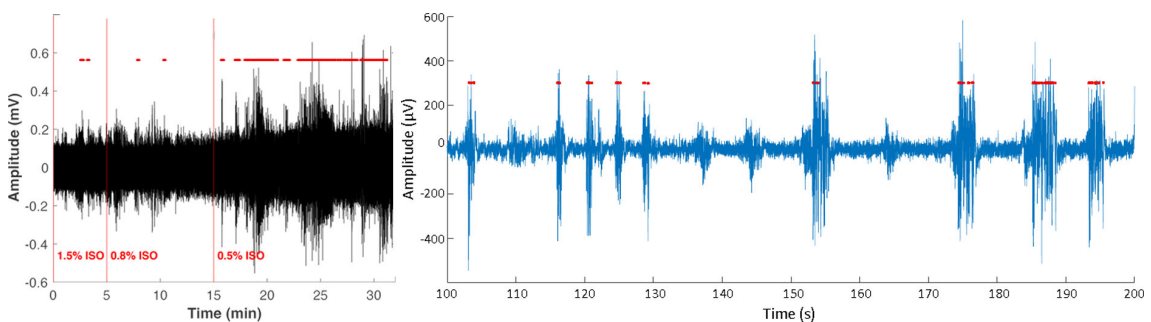


**Figure 5.11:** (a) Spike activity of an individual recording site over a 32-min experiment. The anesthesia volume was decreasing over time from 1.5% to 0.5% (from deeply anesthetized to almost awake animal). (b) Single unit activity (red dots) and LFP data (blue traces) synchronized during burst-suppression.
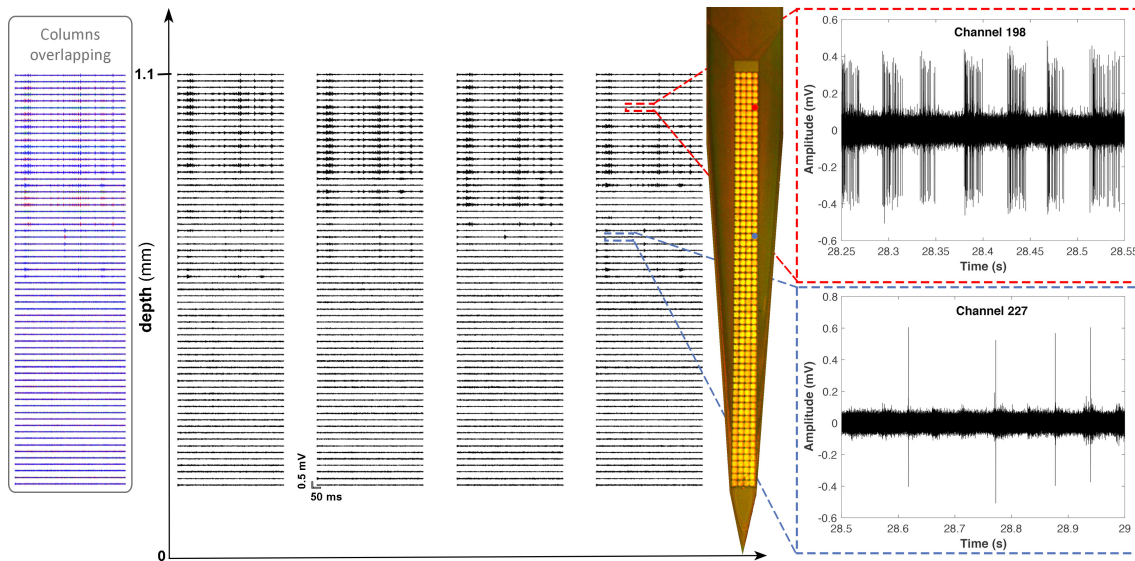
**Figure 5.12:** Spike data from all recording channels of a probe (middle). Spatial oversampling is observed by overlapping spike-traces from adjacent electrodes (combination of the 4 columns, left). Spike train pattern showing burst-suppression (top right) and a sparse firing cell (bottom right).

use of an automatic drilling setup.

Results show that probes were able to extract neural data either from individual recording sites (Figure 5.11) or from the entire probe (Figure 5.12). As an example, Figure 5.11a shows the filtered spike data from an individual channel over a 32-min experiment. The anesthesia volume given to the animal was being decreased over time from 1.5% to 0.5% – Figure 5.11a. As expected, a deeply anesthetized animal shows less activity compared to when it is almost awake where a higher spikes density is observed. As mentioned before, the spike threshold applied was 250 $\mu$V, as a typical recorded extracellular spike shows an amplitude around 400 $\mu$V [3]. Figure 5.11b shows an individual recording channel with filtered LFP data that is perfectly synchronized with a single unit firing rate (visible as the raster plot in red).

Figure 5.12 presents the recording data for all channels at a specific time in the experiment. By overlapping data from adjacent recording electrodes, spatial overlapping can also be observed (overlapping columns, left). This data is important to understand the overall behavior of neural activity in a wide area of the tissue. In this case, in a few-seconds data, it can be simply seen a cell with sparse firing rate (blue zoom area, bottom right), as well as burst-suppression (top right). Burst-suppression pattern is characterized by bursts of high-voltage activity separated by intervals of
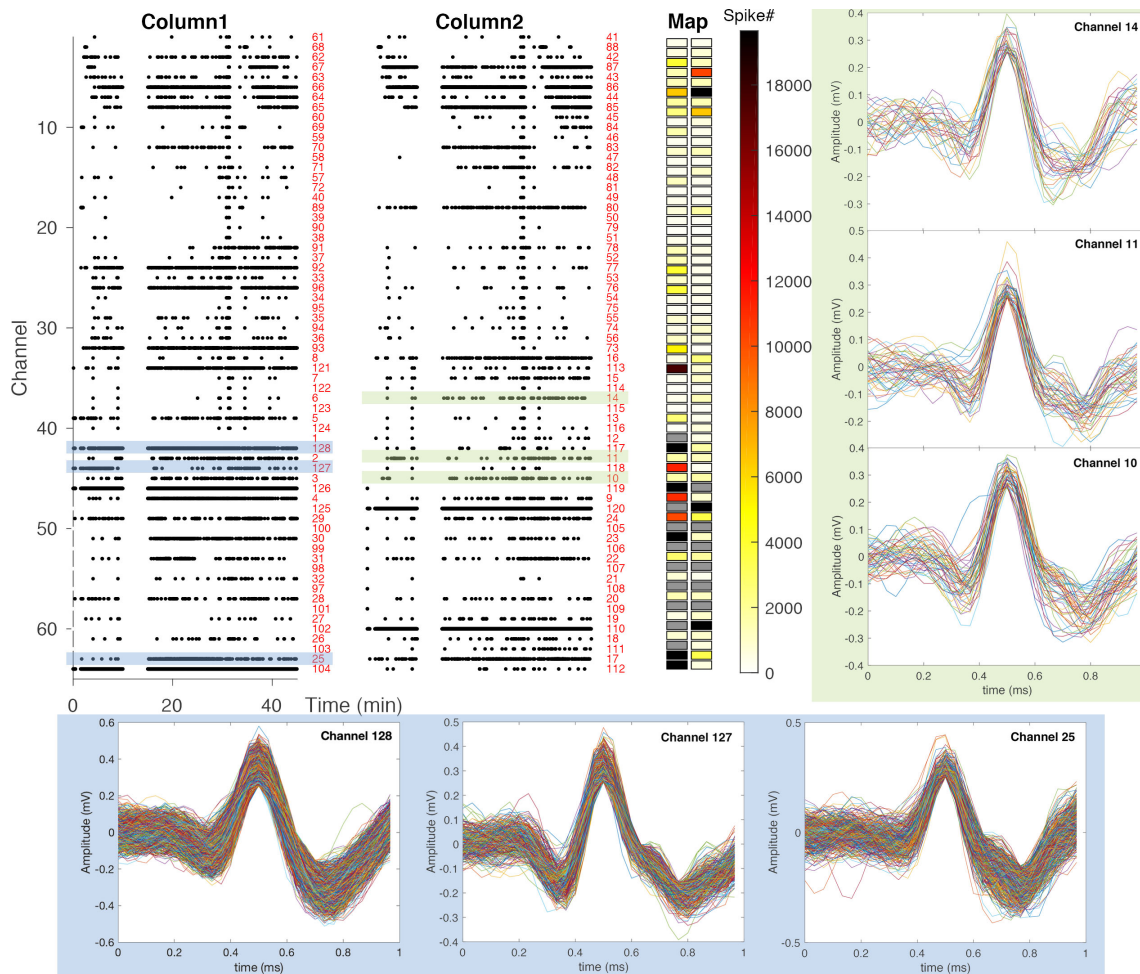
**Figure 5.13:** Raster plot of the all recording sites during an entire experiment using a 128-channel probe. Color map displays color channels as a function of spikes density. Grey-color channels are electrodes with impedance values over 5 MΩ.

apparent inactivity that may last for no more than a few seconds or as long as several minutes [16]. Topically, burst-suppression occurs during the deeper stages of anesthesia [16].

Figure 5.13 shows raster plots of all 128-channels for the entire experiment (≈45 min). This data is important to spatially understand the origin of higher neural activity, and further analyze the corresponding recording points. Due to the large amount of data, only recording channels presenting impedance magnitudes between 100 kΩ and 5 MΩ were analyzed. Channels outside this impedance range are not processed and are colored grey in the color map of Figure 5.13. Highlighted in green is a single neuron that fires with less frequency compared to the cell highlighted in blue. As shown in the image, single units can be recorded redundantly with different recording

channels (channels 10, 11 and 14; or channels 25, 127, and 128). Recorded cells are here sorted exclusively by their firing rate and waveform. Nevertheless, further spike sorting analysis is needed to assess the exact number of single and multi-units were recorded by the probe during the experiment.

## 5.2 Optogenetic silencing in behaving mice

The overall goal of this optogenetic research was to assess silencing process of an optogenetic inhibitor opsin named Jaws, which exhibits an activation spectrum around 632 nm. Although there is a wide range of excitatory and inhibitory opsins reported [17], Jaws seems like a promising tool for optogenetics due to a study reported by Chuong et al. [18]. In this study, it was demonstrated that Jaws can generate red light-induced photocurrents three times those of other silencers.
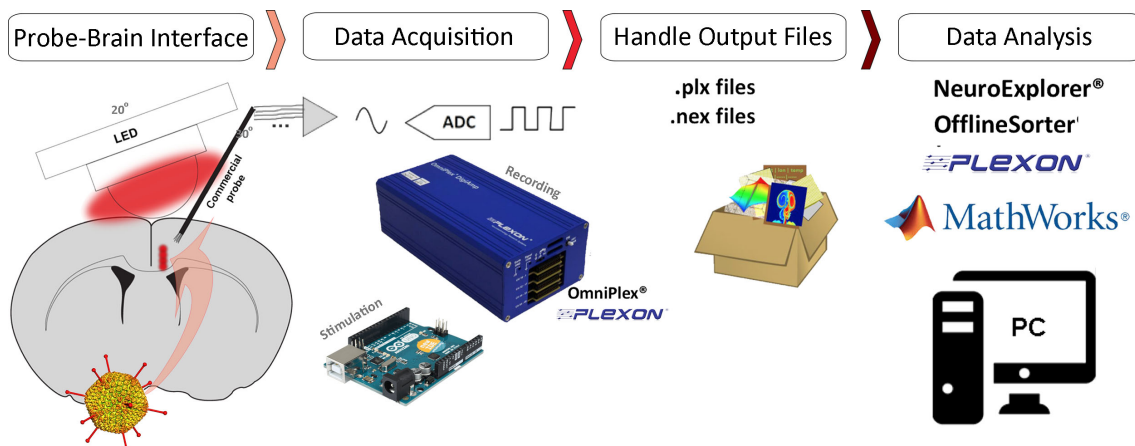


**Figure 5.14:** Schematic of the in vivo recording and optical stimulation process.

In vivo optogenetic recording experiments require a number of steps to perform them and extract biological data. Figure 5.14 shows an illustration of these steps: (1) Promote the interface between probe and brain, which implicates a surgical procedure for a craniotomy, followed by the probe implantation into the animal's brain. The probe was positioned with an angle of 30 ° relative to the animals' skull in order to accommodate the light source. In this case, a LED chip was responsible to delivery light to tissue, and therefore was also attached into the animal head with an angle of 20 °. For optogenetic studies, during surgery it is also necessary to inject a virus with the photosensitive protein (in this case, Jaws) into brain tissue causing the targeted cells to become light-sensitive. After surgery, it was necessary to wait around four weeks for Jaws' expression in the

cells. This time was also important for the animal recovery from the surgery and to adapt to the additional head weight from the probe, rotatory joint and LED; (2) Connect probe to the acquisition system (OmniPlex, Plexon) and perform daily electrophysiology studies in all subjects. Stimulation protocol was needed to be defined a priori and it was implemented using Arduino during recording sessions. The Plexon acquisition system was responsible for collecting, amplifying and digitalizing the data; (3) Extract the recorded raw data from acquisition system and store it into .plx and .nex format files; (4) Use Plexon software (NeuroExplorer and OfflineSorter) and MatLab environment for data analysis. Data analysis consisted in quantifying inhibition efficiency of the infected tissue.

## 5.2.1  Surgical procedure

All experiments were carried out on two C57Bl/6 male mice and were conducted according to local animal care protocols. Surgery was performed in three-week old mice, under ketamine/medetomidine (50/50) anesthesia and using standard stereotaxic procedures. The surgical procedure had a threefold purpose: (i) Viral vector injection to express light-sensitive chloride pump opsin (Jaws). (ii) Probe implantation in the anterior cingulate cortex (ACC) for neural activity recording. This area plays a key role in the expression of remote spatial memories in mice [19]. (iii) LED fixation in mouse's skull to deliver red light to cells.

Viral vector implantation consisted on a unilateral injection of AAV5-CamKII-Jaws-eYFP into the ACC brain area – coordinates [+0.8 mm A/P, -1.0 mm M/L] – so cells express Jaws. Neurons with Jaws and CaMKII expression would inhibit action potentials upon the delivery of red light (wavelength range from 550 nm to 625 nm), silencing neural activity [17].

During surgery, mice were implanted (initial depth was 500 $\mu$m) with a commercial probe that consisted on a 16-metal microwire bundle, equipped with a single screw that allows the user to increment electrodes depth during experiments (Figure 5.15a). This drive implant is used for extracellular electrophysiology and is commercialized by Open Ephys [20]. The implant weighs $\approx$2 g so it can be used in freely moving mice, as intended in this project. Also, it is compatible with a variety of recording systems, in this case it was used the Plexon acquisition system [21]. A LED with 0.9$\times$0.9 mm$^2$ area and a peak wavelength on red light was also implanted and fixed to the animal's skull (Figure 5.15b). Both devices were fixed by dental cement (Figure 5.15c), exposing

electrical connection leads: LED connects to Arduino hardware, and probe connects to a headstage (Omnetics), as shows in Figure 5.15d. Mice were allowed to recover for four weeks after surgery, in order to brain tissue to properly express the light-sensitive protein (Jaws).
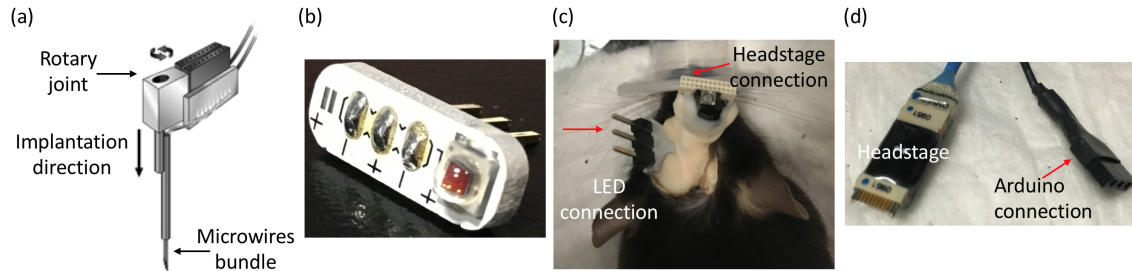


**Figure 5.15:** Surgically implanted tools. (a) Schematic of the microwires bundle with rotary joint (single screw). The whole rotation of the screw represents 200 $\mu$m in depth [21]. (b) $0.9 \times 0.9$ mm$^2$ area LED; (c) Implantation result in mice, covering LED and probe with dental cement and exposing electrical connections. (d) Omnetics headstage that connects to probe, and cable connecting LED to Arduino hardware.

## 5.2.2   Implantation and recording apparatus

Mice were seven-weeks old at the start of experiments. Daily optogenetic recording and stimulation experiments were conducted with behaving awake animals during four consecutive weeks. Immediately before experiments, mice were briefly anesthetized, under isoflurane anesthesia (3-5%), so cable connections could be ensured. During experiments, animals were awake and physically restricted to a cage that enables cables connection of Arduino hardware and OnmiPlex acquisition system to the implanted tools. Real time electrical brain activity data was continuously recorded at 30 kHz, and it was displayed in a monitor connected to OmniPlex hardware. The recording setup is shown in Figure 5.16. Probe electrical ground and reference was connected to the headstage.

In order to keep track of the daily results, every recording session for each specific stimulation and animal required to fill a log. This record basically helped to keep track of how many single or multi-units each channel (representing a single microwire in the probe bundle) is acquiring signal from, and also, to know last position of the rotary screw, since every session screw was turned by 1/4, i.e., 50 $\mu$m.
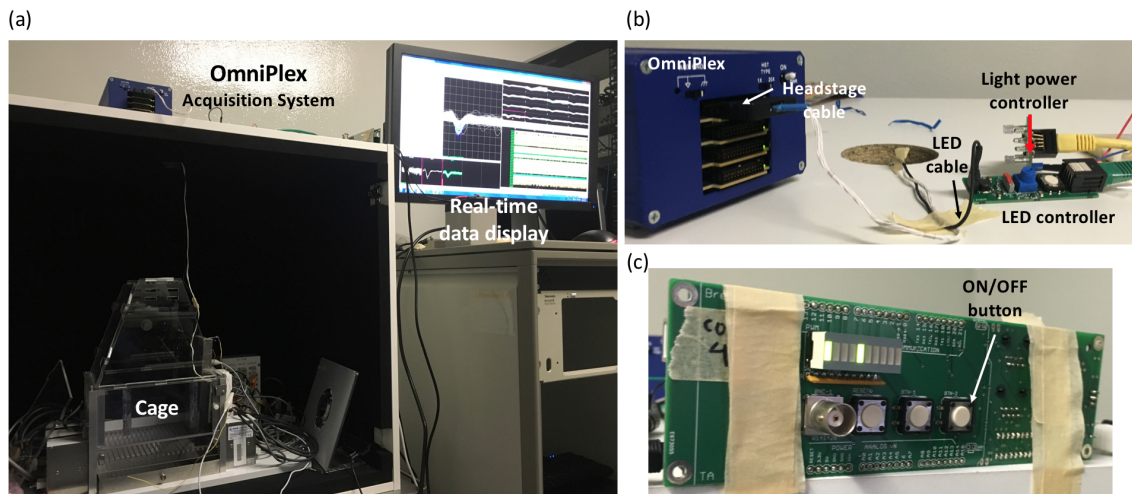
**Figure 5.16:** (a) Setup for optogenetic stimulation and electrical recording experiments in mice. (b) Circuit board for light power controlling of the LED; (c) Circuit board to turn on or off Arduino board, powered by a 12 V battery.

## 5.2.3 Stimulation protocol

Stimulation protocol defines the duration and frequency by which the LED is activated and is delivering light to brain tissue. LED control was performed by Arduino hardware. In order to assess Jaws sensibility to light power, it was used two different light intensities: 10 mW.mm$^{-2}$ and 60 mW.mm$^{-2}$. Also, protocol includes sequential light pulses with 1 s and 5 s duration, with a random interval between them (from 20 s to 40 s). Stimulation protocol follows the schematic of Figure 5.17. Figure 5.18 shows one awake animal with the optical stimulation and electrical recording apparatus and LED turned on and off.



**Figure 5.17:** Light pulse train (1 s and 5 s duration) used in stimulation protocol for different light power intensities (10 mW.mm$^{-2}$ and 60 mW.mm$^{-2}$).

**Figure 5.18:** Awake animal with the optical stimulation and electrical recording apparatus and LED turned on (right) and off (left).
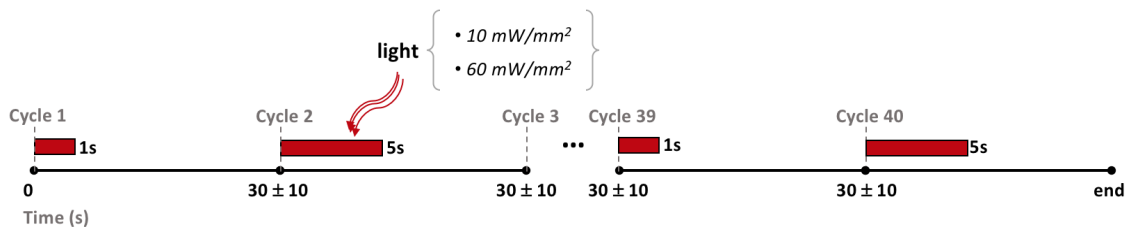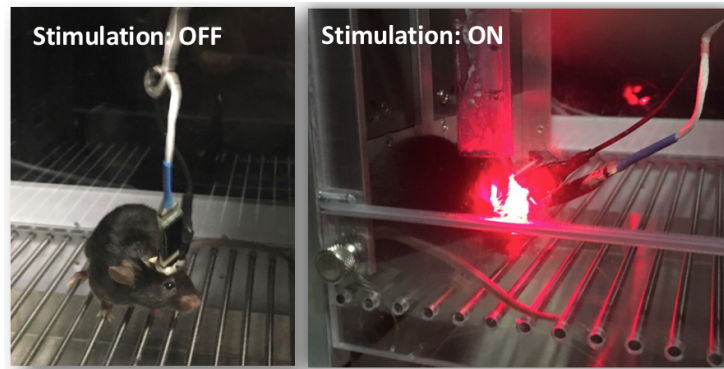
## 5.2.4 Data acquisition and analysis pipeline

**Online Neural Data Processing:** During data acquisition process, it was used OmniPlex Server application (Plexon), which sends the flow of data from hardware devices into software processing module. The application defines the algorithm used for data plotting and filtering for each individual micro-wire electrode (in this case, 16 electrodes).

The PlexControl user interface was used for plotting each channel individually. This tool was useful for real time spike detection of single cells and multi-units based on their waveforms. This process is complicated by common-noise signals resulting from motion artifacts, electromyographic activity and electric field pickup, especially in awake behaving subjects [22]. An example of the spike detection process is shown in the Figure 5.19, where different color in each window channel represents a different cell.

In this electrophysiology setup, there was no additional reference electrode implanted in the animal's brain. Here the approach to contrast the data acquired from each electrode was to introduce a virtual reference. This solution consists of select one of the active recording sites (1 out of 16) to serve as the reference, and therefore, its signal could be subtracted from all recording channels [23]. The virtual reference approach reduces common-noise signal, because common-noise spikes are very similar to neural spikes in their magnitude, spectral, and temporal features [22].

Finally, the raw data and neural signal corresponding to each manual selected unit are saved in a .plx file created by the acquisition system. This is a useful feature for the offline data processing.
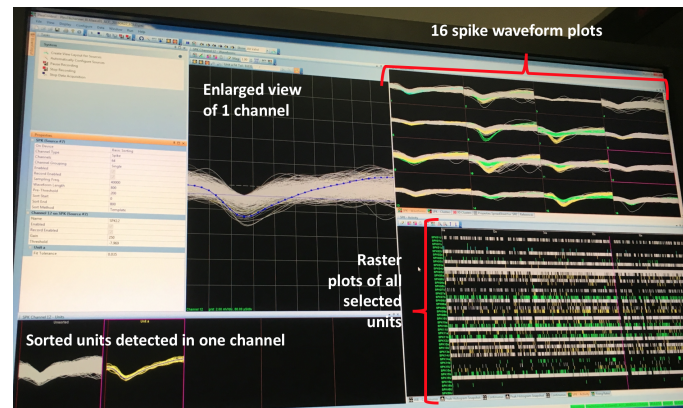
**Figure 5.19:** PlexControl user interface showing the result of a sorting process in the 16 channels (each channel corresponds to a micro-wire electrode).

**Offline Neural Data Processing:** After experiments, neural data processing served to quantify inhibition volumes of the infected mice using Jaws. Firstly, .plx files were converted to .nex files using NeuroExplorer (Plexon). A custom-written script was run in this application to identify light stimulation time event in the data, and thus identify if a specific spike event occurs when light was on or off. OfflineSorter (Plexon) application was used for improving the units sorting, which consequently improves data analysis.

For inhibition quantification, it was used MatLab computing environment (Mathworks), running both built-in and custom-written scripts. Every experimental session for each animal was assessed in order to quantify Jaws inhibition in each cell for all stimulation protocols. Inhibition (in percentage) is obtained with equation 5.1, where mean value of spike events during stimulation is divided by spike events occurring randomly when stimulation is off, using the same time frame.

$$Inhibition_{Jaws}\ (\%)\ =\ \frac{\overline{x}_{spikes\ stimulation\ ON}}{\overline{x}_{random\ spikes\ stimulation\ OFF}} \times 100 \qquad (5.1)$$

## 5.2.5 Photostimulation results and discussion

This optogenetic study aimed to test and quantify a red-light sensitive opsin in the ACC brain area. Although the electrophysiology recordings were performed while the animals were awake, the neural circuits underlying behavior were not assessed. This work demonstrated the capability of Jaws inhibiting neural activity chronically in the target cortex area from awake behaving animals.
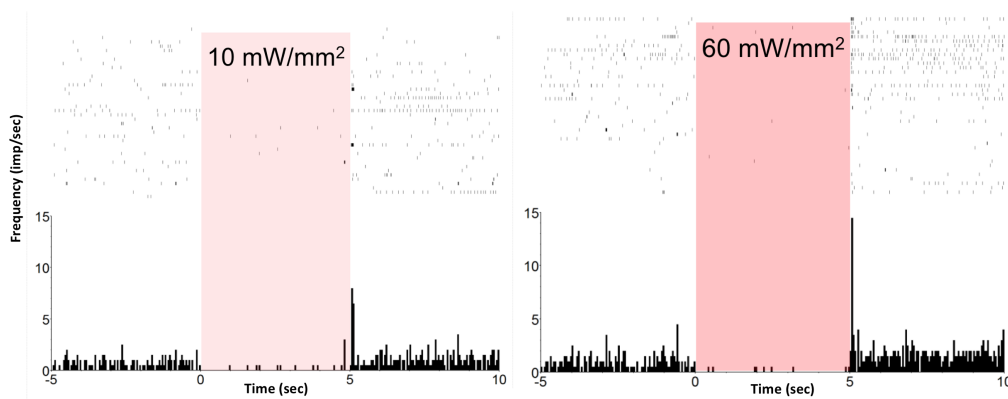
**Figure 5.20:** Results of Jaws inhibition for (a) 10 mW.mm$^{-2}$, and (b) 60 mW.mm$^{-2}$ light power applied during a 5 s pulse duration. Raster plot (top) and histogram (bottom) of neural activity during inhibition and 5 seconds before and after inhibition.

The experimental results show that stimulation with Jaws can effectively inhibit cells with different power intensities, as shows Figure 5.20. No significant difference between 10 mW.mm$^{-2}$ and 60 mW.mm$^{-2}$ was found. This result was expected as the light power employed in both cases largely exceeded the light power limit reported in literature (1 mW.mm$^{-2}$) [24].
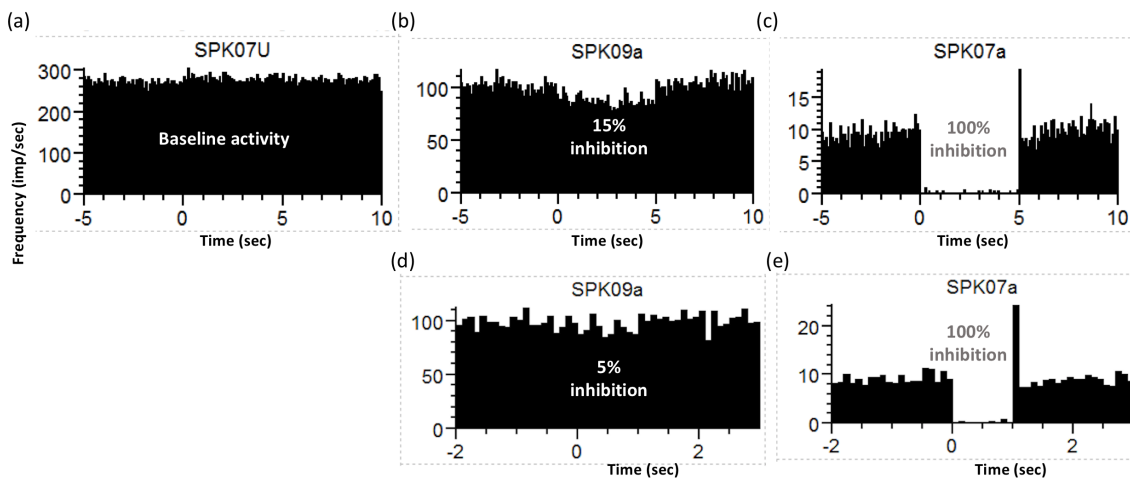


**Figure 5.21:** Histogram of neural activity, resulting on (a) no inhibition, (b) 15% inhibition, and (c) 100% inhibited cells, using a stimulation protocol with 60 mW.mm$^{-2}$ light power and 5 s pulse duration. For the same cell with 1 s light pulses results in (d) 5% and (c) 100% inhibition.

As an example, Figure 5.21 shows the inhibition quantification, for the same cells, using different pulse durations. The unit in Figure 5.21a is not affected by light (0% inhibition), while unit SPK07a was completely silenced when light was being delivered (100% inhibition), using 1 s and
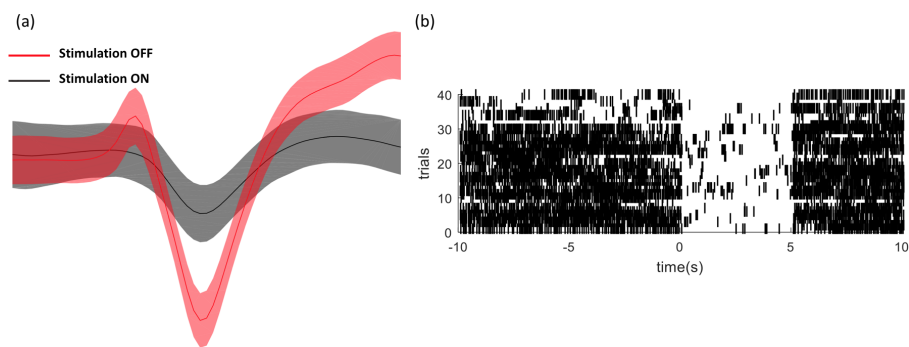
**Figure 5.22:** (a) Jaws inhibition (decreasing in signal amplitude) in a single neuron using a stimulation protocol with 60 mW.mm$^{-2}$ light power and 5 s pulse duration. (b) Raster plot showing firing rate of the single cell during and after stimulation period for an entire session (40 trials).

5 s pulse duration (Figure 5.21c and e, respectively). On the other hand, unit SPK09a expressed slightly different inhibition percentage when exposed with red light for 1 s (5% inhibition) or 5 s (15% inhibition) – Figure 5.21b and d, respectively. This suggests that optogenetic inhibition efficiency varies with exposing light time. This means that Jaws has a time lag that must be considered when using it in in vivo experiments. Moreover, differences in inhibition percentage between cells may result from their distance to light source, which may influence the light power delivered to the cell.

Figure 5.22a shows the amplitude reduction in the action potential of a Jaws-expressing neuron, while exposed to red high light power (60 mW.mm$^{-2}$). For the entire session (40 trials) and 5 s light pulses, it is clear the consistent decrease in the neuron firing rate. This proves the excellent ability of Jaws to inhibit cell populations.

As expected, common-noise signal, specially from animal's movements, had an important effect on the signals acquired. This effect was minimized by offline data sorting. Electrical field effect was minimized by putting animal cage inside a Faraday cage during the experiment sessions. Another important aspect is the virtual reference choice, which user-dependent. This selection may result in quite different conclusions from the same experiment, depending on the reference used [25]. An alternative solution to choose a reference consists of averaging the recording from all functional electrodes and subtracts it from the other electrodes [22, 23]. The averaging will represent the signal from a virtual reference positioned at the center of all recording channels [22].

As a conclusion, Jaws exhibited robust inhibition of neural activity, and it results in strong light responses when used in ACC area of rodent models. Also, it demonstrates Jaws potential as

a neural inhibitor tool. The noninvasive optogenetic inhibition opened up by Jaws [18] enables a variety of important neuroscience experiments and offers a powerful general-use chloride pump for basic and applied neuroscience.

# References

[1] C. M. Gray, P. E. Maldonado, M. Wilson, and B. McNaughton, "Tetrodes markedly improve the reliability and yield of multiple single-unit isolation from multi-unit recordings in cat striate cortex," J. Neurosci. Methods, **63**(1), doi: 10.1016/0165-0270(95)00085-2, 43-54, 1995.

[2] J. Scholvin, J.P. Kinney, J.G. Bernstein, C. Moore-Kochlacs, N. Kopell, C.G. Fonstad, and E.S. Boyden, "Close-Packed Silicon Microelectrodes for Scalable Spatially Oversampled Neural Recording," IEEE Trans Biomed Eng., **63**(1), doi: 10.1109/TBME.2015.2406113, 120-130, 2016.

[3] S. F. Cogan, "Neural Stimulation and Recording Electrodes," Annu. Rev. Biomed. Eng., **10**, doi: 10.1146/annurev.bioeng.10.061807.160518, 275-309, 2008.

[4] M. R. Abidian, and D. C. Martin, "Experimental and theoretical characterization of implantable neural microelectrodes modified with conducting polymer nanotubes," Biomaterials, **29**(9), doi: 10.1016/j.biomaterials.2007.11.022, 1273-1283, 2008.

[5] E. Seker, Y. Berdichevsky, M. R. Begley, M. L. Reed, K. J. Staley, and M. L. Yarmush, "The fabrication of low-impedance nanoporous gold multiple-electrode arrays for neural electrophysiology studies," Nanotechnology, **21**, doi: 10.1088/0957-4484/21/12/125504, 125504, 2010.

[6] S. F. Cogan, P. R. Troyk, J. Ehrlich, C. M. Gasbarro, and T. D. Plante, "The influence of electrolyte composition on the in vitro charge-injection limits of activated iridium oxide (AIROF) stimulation electrodes," J. Neural Eng., **4**, doi: 10.1088/1741-2560/4/2/008, 79-86, 2007.

[7] K. A. Ludwig, J. D. Uram, J. Yang, D. C. Martin, and D. R. Kipke, "Chronic neural recordings using silicon microelectrode arrays electrochemically deposited with a poly(3,4-ethylenedioxythiophene) (PEDOT) film," J. Neural Eng., **3**, doi: 10.1088/1741-2560/3/1/007, 59-70, 2006.

[8] X. T. Cui, and D. D. Zhou, "Poly (3,4-Ethylenedioxythiophene) for Chronic Neural Stimulation," IEEE Trans. Neural Systems and Rehabilitation Engineering, **15**(4), doi: 10.1109/TNSRE.2007.909811, 502-508, 2007.

[9] M. Asplunda, H. von Holst, and O. Inganäs, "Composite biomolecule/PEDOT materials for neural electrodes," Biointerphases, **3**(8), doi: 10.1116/1.2998407, 83-93, 2008.

[10] C. Boehler, M. Asplund, "A detailed insight into drug delivery from PEDOT based on analytical methods: Effects and side effects," J. Biomedical Materials Research A, **103A**(3), doi: 10.1002/jbm.a.35252, 1200-1207, 2014.

[11] T. D. Y. Kozai, K. Catt, Z. Du, K. Na, O. Srivannavit, R. M. Haque, J. Seymour, K. D. Wise, E. Yoon, and X. T. Cui, "Chronic In Vivo Evaluation of PEDOT/CNT for Stable Neural Recordings," IEEE Trans. Biom. Eng., **63**(1), doi: 10.1109/TBME.2015.2445713, 111-119, 2016.

[12] J. P. Kinney, J. G. Bernstein, A. J. Meyer, J. B. Barber, M. Bolivar, B. Newbold, J. Scholvin, C. Moore-Kochlacs, C. T. Wentz, N. J. Kopell, and E. S. Boyden, "A direct-to-drive neural data acquisition system," Front. Neural Circuits, **9**, doi: 10.3389/fncir.2015.00046, 46, 2015.

[13] The HDF Group, Hierarchical data format version 5 (2000-2010), http://www.hdfgroup.org/HDF5

[14] O. Herreras, "Local Field Potentials: Myths and Misunderstandings," Frontiers in Neural Circuits, **10**, doi: 10.3389/fncir.2016.00101, 101, 2016.

[15] G. Praxinos, and K. B. J. Franklin, "The mouse brain atlas in stereotaxic coordinates," Second Ed. Academic Press, San Diego, USA, 2001.

[16] M. J. Aminoff, "Aminoff's Electrodiagnosis in Clinical Neurology. Chapter 3: Electroencephalography: General Principles and Clinical Applications," Second edition, doi: 10.1016/B978-1-4557-0308-1.00003-0, 37-84, 2012.

[17] S. Dufour, Y. De Koninckc, "Optrodes for combined optogenetics and electrophysiology in live animals," Neurophotonics, **2**(3), doi: 10.1117/1.NPh.2.3.031205, 031205, 2015.

[18] A. S. Chuong, M. L. Miri, V. Busskamp, G. A. C. Matthews, L. C. Acker, A. T. S⊘rensen, A. Young, N. C. Klapoetke, M. A. Henninger, S. B. Kodandaramaiah, M. Ogawa, S. B. Ramanlal, R. C. Bandler, B. D. Allen, C. R. Forest, B. Y. Chow, X. Han, Y. Lin, K. M. Tye, B. Roska, J. A. Cardin, and E. S. Boyden, "Noninvasive optical inhibition with a red-shifted microbial rhodopsin," Nat. Neurosci., **17**(8), doi: 10.1038/nn.3752, 1123-1129, 2014.

[19] C. M. Teixeira, S. R. Pomedli, H. R. Maei, N. Kee, and P. W. Frankland, "Involvement of the Anterior Cingulate Cortex in the Expression of Remote Spatial Memory," Journal of Neuroscience, **29**, doi: 10.1523/JNEUROSCI.1068-06.2006, 7555-7564, 2006.

[20] FlexDrive, `open-ephys.org` [Accessed on October 2018]

[21] J. Voigts, J. H. Siegle, D. L. Pritchett, and C. I. Moore, "The flexDrive: An ultra-light implant for optical control and highly parallel chronic recording of neuronal ensembles in freely moving mice," Front. Syst. Neurosci., **7**(8), doi: 10.3389/fnsys.2013.00008, 2013.

[22] K. J. Paralikar, C. R. Rao, and R. S. Clement, "New approaches to eliminating common-noise artifacts in recordings from intracortical microelectrode arrays: inter-electrode correlation and virtual referencing," J. Neurosci Methods, **181**(1), doi: 10.1016/j.jneumeth.2009.04.014, 27-35, 2009.

[23] Q. Liu, J. H. Balsters, M. Baechinger, O. van der Groen, N. Wenderoth, and D. Mantini, "Estimating a neutral reference for electroencephalographic recordings: the importance of using a high-density montage and a realistic head model," J. Neural Eng., **12**(5), doi: 10.1088/1741-2560/12/5/056012, 056012, 2015.

[24] E .S. Boyden, F. Zhang, E. Bamberg, G. Nagel, and K. Deisseroth, "Millisecond-timescale, genetically targeted optical control of neural activity," Nat. Neurosci., **8**(9), doi: 10.1038/nn1525, 1263–1268, 2005.

[25] Y. Tian, and D. Z. Yao, "Why do we need to use a zero reference? Reference influences on the ERPs of audiovisual effects," Psychophysiology, **50**(12), doi: 10.1111/psyp.12130, 1282-1290, 2013.

# Chapter 6

# Conclusions and Future Work

In this chapter are summarized the conclusions reached on this PhD work, taking into account the main goals presented on Chapter 1. In view of the obtained results and limitations, it is also presented future developments for improving the proposed microdevice.

## 6.1 Conclusions

This PhD work had twofold objectives: (i) Develop a robust implantable microsystem for optogenetic applications, with simultaneous electrical recording and optical stimulation capability of brain circuits; and, (ii) perform in vitro and in vivo characterization techniques for the device validation as a useful tool in neuroscience.

Results show that optrode devices were successfully manufactured using standard microfabrication technologies, such as photolithography, thin-film deposition and low-cost traditional mechanical blade dicing technology. Fabrication results suggest a robust probe design consisting of 8 mm long and 600 $\mu$m wide single-shafts with a sharp tip. An overall comparison to the LED-optrodes presented in literature, the proposed device presents long shafts that enables reaching deep neural structures in the brain of a rodent. This feature was accomplished using blade cutting technology that is a purely mechanical microfabrication process and is characterized by its simplicity and reproducibility, capable of producing high-aspect ratio devices. The 2D dicing methodology applied to Si substrates facilitates the integration with patterning process, frequently used in MEMS and

CMOS industry.

The integration of commercial LED chips presented both advantages and disadvantages. The manual assembly of the LED to substrate represents as a hard task and showed yield challenges. As an advantage, the use of different wavelength LEDs for simultaneous activation and inhibition of engineered tissue is possible with the commercial chip coupling approach. The large dimensions of the LED chip were a limitation factor to reduce probe width. As previously discussed, shaft cross-section must still be optimized for rodents' application, as it might cause a significant damage to neurons. With our fabrication approach, wide probes are necessary to accommodate large LED chip and recording sites. The pitch between recording points was limited by the photolithographic processes in room conditions. Blade dicing cuts hinder the reduction of the shafts thickness, as cuts with thinner substrates resulted in the wafer breakage.

Electrochemical, optical and mechanical testing also demonstrates a robust optrode micro-system. Low impedance values of recording sites and sufficient light power results show great potential for this design to modulate neural activity in both cortical and deeper brain regions. Mechanical validation showed strong shafts capable of withstanding high longitudinal compression forces before breaking, while requiring low forces (magnitude of mN) to implant them into brain tissue.

The in vivo validation using the proposed optrode is currently being performed. Optogenetic experiments done in animals are time-consuming and require a careful protocol preparation. The optrode will be implanted in ACC cortical area, and engineered brain cells expressing ChR-2 opsin will be tested to promote cells excitation when blue light is delivered into focus area, as well as the electrical activity of cells in the vicinity of probe implantation area will be recorded. On the other hand, in vivo acute recordings using close-packed probes successfully recorded LFP and several single cells based on waveform and firing rate analysis. Optogenetic experiments using a commercial tetrode proved to be a successfully study, as electrical activity of Jaws-expressing cells was turned off (silenced) when they were exposed to red light.

## 6.2 Future Work

The proposed microsystem in this work has still a lot of room for improvement to become a mature optogenetic tool. Some of these improvements are suggested in this section as future work directions.

In the perspective of reducing cross-section dimensions of the proposed device, future work could include monolithically manufacturing LEDs onto the probe. In the last two decades, studies demonstrate how to produce micro-scale and high-efficiency LEDs based on GaN technology in a wide range of the visible spectrum [1, 2].

Another future strategy to improve efficiency of the optrode could include the integration of an optical lens over the LEDs surface. The LED-lens combination would enable the convergence and focusing of the light onto the LED active area. Our group reported the fabrication of polymeric lenses using photolithography and thermal reflow processes [3]. The final lenses had dimensions in the range of 30 $\mu$m, 4.9 mm and 5 $\mu$m in width, length and thickness, respectively. The length of the lithographic-based lenses results from the fact that they were manufactured over photodiode arrays. Adjusting lenses and LED dimensions would only require employing compatible lithographic masks for proper photoresist patterning over the LED emission area. As an alternative process to traditional lithographic-based lenses, Thiele et al [4] reported the fabrication process of a 3D 200 $\mu$m lens structure over a 100 $\mu$m LED, using direct laser writing (DLW). With a collimation factor increment of 6.2 and the emission half-angle reduced by 50%, DLW technology proved to be a promising choice to produce collimating lenses. Despite its flexibility to 3D structuring and sub-micrometer resolution, DLW can be time consuming to fabricate arrays of micro-optical devices and complex photonic structures.

As previously discussed, since LED chips are the direct light source interface, a major concern consists of tissue damage due to overheating. Thus, it becomes crucial to assess thermal properties of optical sites under various conditions, avoiding inadequate light-power density or exposure time, which can cause tissue damage. Probes providing in situ heat monitoring can be particularly important on academic scenarios, where photostimulation protocols are frequently customized to each experiment and application. As preliminary work, our group reported the integration of a Pt thermoresistance into an optrode device for thermal sensing in the vicinity of LED-based

stimulation [5]. This combination of hybrid devices might open new avenues for the study of brain networks.

The 3D capability of recording and photostimulation is a key element for more realistic and complete information gathering of neural networks. Strategies for targeting 3D distributed brain structures could simply include manufacturing of planar optrode arrays using stacking methods [6] or alignment plates [7], and thus enabling independent light delivery to dozens of sites distributed in a 3D fashion throughout neural circuits.

Finally, strategies to reduce the acute inflammatory or chronic foreign body response of neural tissue to implanted devices could be employed. This is important because responses of neural tissue can lead to signal loss due to neuronal loss in the vicinity of the implanted device [8]. Thus, in order to improve electrode-neural tissue interface and promote long-term recording stability, biomaterials filled with anti-inflammatory drugs and neurotrophins can be coated onto the shaft of the probe. Hydrogels and fast degrading conductive polymers [9, 10] can be used to reduce the inflammatory tissue response and/or camouflage the implanted device [8].

# References

[1] T. Kim, Y. H. Jung, J. Song, D. Kim, Y. Li, H. Kim, I. Song, J. J. Wierer, H. A. Pao, Y. Huang, and J. A. Rogers, "High-Efficiency, Microscale GaN Light-Emitting Diodes and Their Thermal Properties on Unusual Substrates," Small, **8**(11), doi: 10.1002/smll.201200382, 1643-1649, 2012.

[2] S. Nakamura, M. Senoh, N. Iwasa, S. Nagahama, "High-Brightness InGaN Blue, Green and Yellow Light-Emitting Diodes with Quantum Well Structures," Jap. J. Appl. Phys., **34**(2), doi: 10.1143/JJAP.34.L797, L797-L799, 1995.

[3] R. P. Rocha , M. J. Maciel, J. M. Gomes, J. P. Carmo, and J. H. Correia, "Fabricating microlenses on photodiodes to increase the light-current conversion efficiency," IEEE Sensors J., **14**(5), doi: 10.1109/JSEN.2014.2305623, 1343-1344, 2014.

[4] S. Thiele, T. Gissibl, H. Giessen, and A. M. Herkommer, "Ultra-compact on-chip LED collimation optics by 3D femtosecond direct laser writing," Opt. Lett., **41**(13), doi: 10.1364/OL.41.003029,

3029-3032, 2016.

[5] S. B. Goncalves, J. M. Palha, H. C. Fernandes, M. R. Souto, S. Pimenta, T. Dong, Z. Yang, J. F. Ribeiro, and J. H. Correia, "LED optrode with integrated temperature sensing for optogenetics," Micromachines, **9**(9), doi: 10.3390/mi9090473, 473, 2018.

[6] C. Chang, and J. Chiou, "Development of a Three Dimensional Neural Sensing Device by a Stacking Method," Sensors, **2010**, 10, doi: 10.3390/s100504238, 4238-4252, 2010.

[7] J. Scholvin, A. Zorzos, J. Kinney, J. Bernstein, C. Moore-Kochlacs, N. Kopell, C. Fonstad, and E. S. Boyden, "Scalable, Modular Three-Dimensional Silicon Microelectrode Assembly via Electroless Plating," Micromachines, **9**(9), doi: 10.3390/mi9090436, 436, 2018.

[8] T. D. Y. Kozai, A. S. Jaquins-Gerstl, et al., "Brain Tissue Responses to Neural Implants Impact Signal Sensitivity and Intervention Strategies," ACS Chem. Neurosci., vol. 6, no. 1, pp. 48–67, Jan. 2015.

[9] C. D. Lee, S. A. Hara, et al., "Matrigel coatings for Parylene sheath neural probes," J. Biomed. Mater. Res. Part B Appl. Biomater., vol. 104, no. 2, pp. 357–368, Feb. 2016.

[10] T. H. Qazi, R. Rai, et al., "Tissue engineering of electrically responsive tissues using polyaniline based polymers: A review," Biomaterials, vol. 35, no. 33, pp. 9068–9086, Nov. 2014.

# Appendix A

# Journal Publications

The following is the list of the international journal publications that have resulted from this thesis.

1. S. B. Goncalves, J. M. Palha, H. C. Fernandes, M. R. Souto, S. Pimenta, T. Dong, Z. Yang, J. F. Ribeiro, and J. H. Correia, "LED optrode with integrated temperature sensing for optogenetics", Micromachines, **9**(9), 473, 2018. IF = 2.222 doi: 10.3390/mi9090473

2. S. B. Goncalves, A. M. Loureiro, H. C. Fernandes, S. Pimenta, J. F. Ribeiro and J. H. Correia, "High-aspect ratio Si neural shafts: Fabrication and Brain Implantation", IEEE Journal of Microelectromechanical System, 2018. IF = 2.475 doi: 10.1109/JMEMS.2018.2868229

3. S. B. Goncalves, A. F. Silva, J. F. Ribeiro and J. H. Correia, "Implantable Neural Microsystems in Medical Industry," IEEE Sensors Journal, **18**(5), 2117-2124, 2018. IF = 2.512 doi: 10.1109/JSEN.2018.2791802

4. S. B. Goncalves, J. F. Ribeiro, A. F. Silva, R. M. Costa and J. H. Correia, "Design and Manufacturing Challenges of Optogenetic Neural Interfaces: A Review," Journal of Neural Engineering, **14**, 041001 (18pp), 2017. IF = 3.493 doi: 10.1088/1741-2552/aa7004

5. S. B. Gonçalves, J. F. Ribeiro, A. F. Silva and J. H. Correia, "High Aspect-Ratio Neural Probes using Conventional Blade Dicing," Journal of Physics: Conference Series, **757**(1), 012011, 2016. IF = 0.45 doi: 10.1088/1742-6596/757/1/012011

6. S. B. Goncalves, M. J. Oliveira, A. C. Peixoto, A. F. Silva and J. H. Correia, "Out-of-plane neural microelectrode arrays fabrication using conventional blade dicing," The International Journal of Advanced Manufacturing Technology, **85**(1), 431-442, 2015. IF = 1.458 doi: 10.1007/s00170-015-7948-7

7. S. B. Goncalves, A. C. Peixoto, A. F. Silva and J. H. Correia, "Fabrication and mechanical characterization of long and penetrating length neural microelectrode arrays", Journal of Micromechanics and Microengineering, **25**, 055014, 2015. IF = 1.79 doi: 10.1088/0960-1317/25/5/055014